POLITECNICO DI MILANO

M. Sc. in Mathematical Engineering

Major in Computational Science and Engineering

School of Industrial and Information Engineering

An image-based computational hemodynamics analysis of systolic obstruction in hypertrophic cardiomyopathy

Supervisor: Prof. Christian VERGARA

Assistant supervisor: Dr. Ivan FUMAGALLI

A.Y. 2020-2021

M.Sc. Thesis of

Piermario VITULLO

ID: 919817

Abstract

Hypertrophic Cardiomyopathy (HCM) is a very common pathological condition among the cardiovascular diseases, characterized by an abnormal thickening of the myocardium. It has a relevant impact on the global cardiac function and may lead to fatal outcomes as sudden cardiac death. Moreover, HCM may induce flow obstructions if the pathology affects the medio-basal region of the interventricular septum. In that case we refer to the pathology as Hypertrophic Obstructive Cardiomyopathy, that is a more severe form of HCM. In this work the aim is to assess the effects of this condition on the left ventricle hemodynamics of different patients suffering from HCM, determining if it induces an obstruction during the systolic phase. In order to achieve the goal, an image-based computational pipeline is provided, integrating a Computational Fluid Dynamics (CFD) analysis in moving domain with the reconstruction of the patient-specific ventricular geometry and motion from standard cine-MRI images, routinely acquired in diagnostic procedures. The mathematical model, hinging upon incompressible Navier-Stokes Equations, combines in a unique framework the Arbitrary-Lagrangian-Eulerian (ALE) formulation, accounting for the moving domain, with a resistive method, modeling the immersion of the mitral valve in the computational domain. The model is discretized by a stabilized finite element method. The analysis of outputs of interest, after the elaboration of clinical images of patients coming from L. Sacco Hospital in Milan and the numerical simulation of the problem, provide, for each HCM patient, a better understanding of the patho-physiological behaviour of hemodynamics (due to the abnormal morphological and dynamical conditions of the left ventricle). Moreover, relying on clinical guidelines, the investigation of the numerical results yields a computational-based classification of such patients. Furthermore, preliminary clinical indications that may help diagnosis and design of a possible surgical treatment (*septal myectomy*) are provided.

Keywords: **mitral valve**; **hypertrophic cardiomyopathy**; **septal myec-**

tomy; **cine-MRI**; **image-based computational fluid dynamics**

Sommario

La Cardiomiopatia Ipertrofica è una condizione patologica molto comune tra le malattie cardiovascolari, caratterizzata da un ispessimento anomalo del miocardio. Ha un impatto rilevante sulla funzione cardiaca globale e può risultare fatale, causando morte cardiaca improvvisa. Inoltre, la Cardiomiopatia Ipertrofica può causare ostruzioni al flusso se la patologia colpisce la regione medio-basale del setto interventricolare. In quel caso la patologia è definita Cardiomiopatia Ipertrofica Ostruttiva, che è una forma più severa della malattia. In questo lavoro, l'obiettivo è valutare gli effetti di tale patologia sull'emodinamica del ventricolo sinistro, stabilendo se causi un'ostruzione durante la sistole. Lo scopo è stato raggiunto presentando una pipeline computazionale basata sull'imaging, che integra l'analisi mediante fluidodinamica computazionale in dominio mobile con la ricostruzione della geometria e del movimento del ventricolo paziente-specifico, ottenuta tramite immagini standard cine-RM, regolarmente acquisite nelle procedure diagnostiche. Il modello matematico, basato sulle Equazioni di Navier-Stokes relative a un fluido incomprimibile, unisce in un unico sistema la formulazione ALE, che modella il dominio mobile, con un metodo resistivo, che rappresenta matematicamente l'immersione della valvola mitrale nel dominio computazionale. Tale modello è discretizzato con un metodo agli elementi finiti stabilizzato. L'analisi degli output d'interesse, a seguito dell'elaborazione delle immagini cliniche dei pazienti fornite dall'Ospedale Sacco di Milano e della simulazione numerica del problema, permette, per ogni paziente HCM, una migliore comprensione del comportamento fisiopatologico dell'emodinamica (per via delle condizioni morfologiche e dinamiche del ventricolo sinistro). Inoltre, basandosi sulle indicazioni guida cliniche, lo studio dei risultati numerici porta a una classificazione di tali pazienti fondata sul metodo computazionale. Infine, vengono fornite delle indicazioni cliniche preliminari che potrebbero aiutare nella diagnosi e nella progettazione di un eventuale trattamento chirurgico (*miectomia settale*).

Parole chiave: **valvola mitrale**; **cardiomiopatia ipetrofica**; **miectomia settale**; **cine-RM**; **fluidodinamica computazionale basata sulle immagini**

Contents

List of Figures

List of Tables

Chapter 1

Introduction

Hypertrophic cardiomyopathy (*HCM*) is one of the most common *Cardiovascular Diseases* (*CVD*) that affects heart anatomy and functional efficiency, by means of an anomalous myocardial thickening. CVD are responsible for many fatal outcomes as strokes or heart attacks, possibly causing sudden death in young patients. Since the CVD incidence in recent years had a considerable increase, the interest in a mathematical and numerical modelization of the effects of these pathologies on the circulatory system has risen in the scientific and medical community.
The aim of this work is to apply for the first time to HCM cases a computational pipeline, in order to describe the consequences in the hemodynamics and in the anatomy of patient-specific *left ventricles* (*LV*), providing a relevant support to clinicians for the treatment of the pathology in the decision-making phase.
Indeed, pharmacological therapies or changes in lifestyle are suggested for less severe cases, while in the most critical ones a surgical treatment, as *septal myectomy*, is necessary. The goal is to help clinicians to understand whether to go into surgery and, in that particular case, locate the portion of the interventricular septum to resect.
Before starting a deep discussion over the mathematical and numerical modeling of the physical problem, the focus is on providing a basic insight of the structure and the global functioning of the cardiovascular system and in particular of the left ventricle, in order to understand how HCM has a relevant impact on the blood flow efficiency and the myocardial structure.

1.1 The cardiovascular system

The cardiovascular system is an organ system whose main task is the transport of blood, a red-colored fluid connective tissue mainly formed by *plasma* (made by proteins, ions and, at 92%, by water [25]), which contains oxygen, waste products, nutrients, hormones and all the chemical substances that need to be delivered in specific areas of the body. It is a closed circuit that consists of *elastic vessels*, which bring blood in all the regions of the organism, two *circulatory loops*, with the aim of carrying oxygenated and deoxygenated blood, and an organ which powers all the system, acting as a pump, the *heart*. These three compartments form the circulatory system, thanks to which blood flows and reaches every living tissue, in a one-way direction and developing oxygen and substances.
The first of the two circulatory loops is the systemic circulation, that is made of:

- *arteries*, vessels with the aim of carrying oxygenated blood from the left heart to the living tissues;
- *veins*, vessels which let, instead, the non-oxygenated blood to come back to the right heart;
- *microvasculature*, that allow the exchange of nutrients and regulate the blood flow due to the high resistance which entail the decrease of fluid pressure.

Arteries compose a network in which branches decrease of size the more they reach the peripheral regions of the body. The largest one is the *aorta*, that has an average physiological diameter of 2.5 cm in adults and connects left ventricle to arterial tree. In this vessel a peak of flow rate is registered, with a high Reynolds number that is reached ($\sim$4000), 10 times higher than in other blood vessels, as coronary arteries, where the reference value is $\sim$400 [24]. In terms of elasticity, arteries have highly non-linear elastic properties, due to the presence of distensible structures of elastin at small strain and collagen fibers that increase strength at large strain. The concentration of these two substances is higher in the aorta and in proximal arteries to the heart, to ensure an increased extensibility. Going downstream in the arterial tree, the concentration decreases in order to allow microvasculature to store blood and discharging it, carrying it back to the heart crossing the venous system.
Veins, instead, are characterized by more compliance: arteries need to be more elastic, in order to be extensible as a response of every pulse of heart,

while veins are provided with valves, in order to keep the blood flowing in one direction and against gravity.
A typical assumption for the blood flow is to consider a Newtonian fluid: the main reason is in the difference in dimension between the arteries and veins diameter (10^{-1}cm) and the blood cells one (10^{-3}cm).
In summary, vasculature has some main properties that arise from its description: the *complexity*, due to the complicated vessels network and the biological functioning, and the *variability* in vessels shape, branching, path and demands on the system.
The second loop is the pulmonary circulation, where the action of *pulmonary arteries* allows the transport of non-oxygenated blood from the right heart (where it is ejected) directly to the **lungs**; in this organ, then, blood becomes oxygenated and it is ready to be carried by the *pulmonary veins* back to the left heart. In a heartbeat, the pressure varies in a range of 70-130 mmHg in the systemic circulation, while in the pulmonary one, the range is 20-30 mmHg. [24]
The most important compartment in the circulatory system is the *heart*, that acts as a mechanical pump, ejecting blood into arteries and gathering it from veins.

1.1.1 An overview on the anatomy of the heart

Heart is composed by the *left* and *right* part, separated by the *interatrial* and *interventricular septa* (made of thick muscular tissue and a fibrous termination region near the aortic valve) and each of which consists of two chambers, the **atrium** and the **ventricle**.
The interventricular septum is continuous with respect to the left ventricle wall and it has a curved and convex form from the point of view of a physiological right ventricle: as a consequence, the latter is narrower than the left chamber, which is, instead, cone-shaped. The heart is as a striated involuntary muscle made up of three layers: the myocardium, that is the thick central muscular layer (made of *cardiomyocites*, collagen and capillaries), that contains the thinner inner one, the *endocardium* (made of endothelium), and the outer one, the *epicardium*. All the structure is enclosed in a protective membrane, the *pericardium*, that has the role of isolating the heart from other organs, and located in the middle area of the chest, between the lungs.
Heart compartments are provided also with *atrioventricular valves*, that link atria and ventricles: the *tricuspid valve* acting in the right heart and the

bicuspid **mitral valve** in the left one.
There are also two more semilunar valves that separate the ventricles and circulatory system, the *pulmonary valve* in the right heart and the tricuspid **aortic valve**.
Valves allow blood circulation into the two loops. The systemic one starts from the left ventricle, where oxygenated blood ejected through the Left Ventricle Outflow Tract (LVOT), with the opening of the aortic valve. It reaches aorta crossing the root and ascending part and reaching the living tissues through the arterial branches and microvasculature, where nutrients are exchanged. After this phase, non oxygenated blood is driven back to the right heart thanks to veins, in particular the superior and inferior vena cava.
Here pulmonary circulation starts, in series, with the transport of non-oxygenated blood from the right heart to the lungs with the pulmonary arteries, the latter transfers carbon dioxide (collected from the tissues) to the airways and acquires oxygen and finally it is ready to come back to the left atrium crossing the pulmonary veins. After crossing the mitral valve, blood is transferred back to the left ventricle. (Figure 1.1).

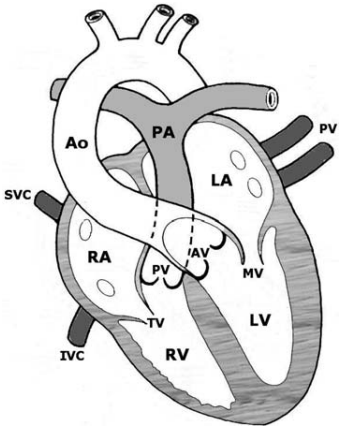

Figure 1.1: Heart cross section; the represented chambers are the left ventricle (LV), left atrium(LA), right ventricle (RV), right atrium (RA); the valves are the mitral valve (MV), aortic valve (AV), tricuspid valve (TV), pulmonary valve (PV); the vessels are the aorta (Ao), pulmonary artery (PA), pulmonary veins (PV), superior and inferior vena cava (SVC and IVC) [25]

The heart contraction is vital, it starts by electrical impulse, it is regulated by chemical agents and represents the mechanism that allow the blood to be pumped into the two circulations (Figure 1.2): besides, it is the cause

of the main characteristic of the blood flow, the **pulsatility**. The latter is fundamental, because it doesn't allow blood to a transition to a full turbulent flow when high Re are reached (for example in the aorta). For this reason the regime is laminar (for example in coronary arteries) or developing to a partial transition to turbulence.
Moreover, heart generates the pressure gradient that allows the fluid to reach a lower pressure areas from a higher pressure ones. As a consequence, it affects the flow rate: flow regulation is a fundamental process held by the cardiovascular system to guarantee the correct metabolic behaviour and constant perfusion pressure for each organ.

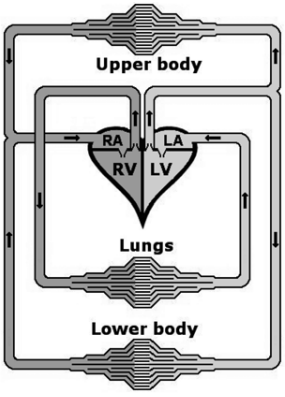

Figure 1.2: A sketch of the circulatory system, with the four chambers of the heart [25]

1.1.2 Electrical propagation

The ventricular contraction allowing blood flow into the systemic circulation is stimulated by heart electrical impulses, coming from a natural pacemaker located in the right atrium, the *sinoatrial node*, that determines the whole myocardium rhytm in terms of heartbeats. It is important to briefly describe the propagation process of the electrical signals, which are triggered by an electrical potential spreading in the myocardium: thanks to the stimulation and activation of specific heart cells, called *cardiomyocytes* (with the generation of an action potential over a suitable threshold), the membrane voltage varies, while the opening and closing of several ion channels that let the current crossing the membrane.
In particular, at the start, an inward sodium current stimulates the membrane at rest and its potential varies from $\sim$ -90 mV to $\sim$ 20 mV, through a *rapid depolarization* process. Then the extracellular calcium ions channel is

activated by the sodium one, with a short phase of repolarization, that leads to a refractory period, where a characteristic *plateau* around 0 mV is observed. In this phase any further stimulus is inhibited Finally, the outward flow of potassium ions determines a *repolarization* that brings the potential back to the rest value.

1.2 Left ventricle structure and global functioning

1.2.1 Anatomy of the left ventricle

One main property of both atrioventricular valves (Figure 1.4) is the connection of the cusps through inelastic components named *chordae tendinae* to specific ventricular appendices protruding internally in the cavity, called *papillary muscles*. Their task is to stabilize the two-cusps mitral valve structure in the inlet area and to avoid the prolapse of the ventricles into the atria during the contraction phase, that would lead to backflows.
These traits are not accounted for the valves in the outlet tract of the ventricles (the aortic and pulmonary one), since their three-leaflets-structure ensures support when valves are closed.
Regarding the structural properties of the left ventricle for a healthy patient, the wall dimension usually varies from 8 mm when it is relaxed to 12 mm when it is contracted (it is larger in the basal interventricular area and it reaches its minimum in the apical part). It is quite thicker than the right ventricle one, varying in a range of 2-7 mm. This is expected, since in the left ventricle the highest values of pressure are reached due to blood ejection into systemic circulation, so the thickness of the myocardium is lower in the right ventricle
The myocardium is characterized by a helical orientation of the myofibre, that varies from the basal to the apical region and, in depth, from the outer epicardial layers to the inner endocardial ones.
As it can be observed from clinical images (for example in Figure 1.3), the left ventricle aspect is not regular as in the graphical representations, but high invagination of the surface is detected, due to the presence of muscular bundles, the *trabeculae carnae*, which decrease smoothness in the apical and medio-basal regions.
In the basal area, the mitral valve (MV) is composed by two leaflets, an anterior one, covering a larger part of the valve annulus, and a posterior one, that has, instead, a larger surface area, even if the former rises higher. This configuration is caused by the fibrous ring surrounding the MV, the *mitral*

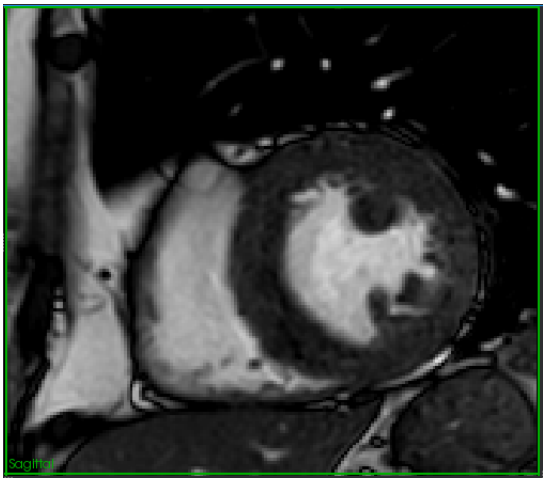

Figure 1.3: Short-axis visualization in a cardiac MRI sequence, where it is highlighted a section of a left ventricle and, in particular, the effect of the trabeculae carneae and the papillary muscles on the aspect of the LV (clinical images provided by L. Sacco Hospital in Milan)

annulus, that is saddle-shaped, in order to confer a mechanical advantage to both cusps by adding curvature.
Furthermore, the semilunar aortic valve (AV) acts in between the left ventricle and the aortic root and it is formed by three scoop-shaped leaflets (tricuspid valve), each of which attached to the fibrous annulus.
An interesting aspect regarding the position of the mitral and aortic valvular rings is their connection through a triangular fibrous structure that ensures continuity: the *fibrous trigone*. Usually, the inclination between the two planes enclosing it reaches 30 degrees. But, as it will be discussed in the next chapters, this value can vary; in one of the patient-specific cases, an increased inclination will be detected.

1.2.2 The cardiac cycle

The pressure driven fluid flow is regulated by the heart, that pumps and ejects blood from the ventricles to the aorta and the pulmonary artery. In order to perform this process, a threshold blood pressure value needs to be exceeded in the arteries (70 mmHg for the aorta, 10 mmHg in the pulmonary artery), since vessel walls have elastic properties and react to deformation induced by blood and the pumping action of heart that allows blood to reach every living tissues.

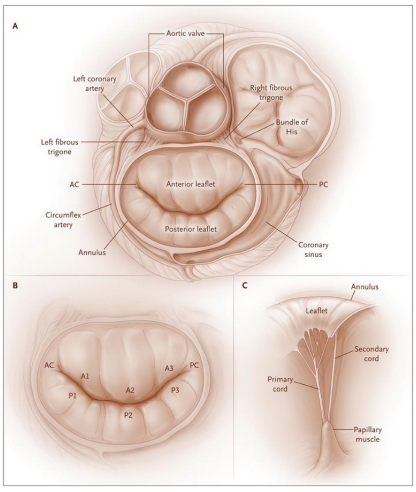

Figure 1.4: Cross section of the left heart, with the representation of the aortic and mitral valves and the visualization of the complex MV structure (https://www.bjaed.org/article/S2058-5349(17)30007-0/pdf)

In summary, for each heartbeat, the exerted work is:

$$W = QP + \frac{1}{2}mv^2 \tag{1.1}$$

where Q is the blood flow rate, P is the arterial blood pressure, m is the ejected mass and v is the blood velocity in the artery.
From the ratio between the energy W and the total energy consumption, an efficiency marker of the heart can be computed: a physiological reference value is about 25%.
For what concerns the cardiac cycle (Figure 1.5), two specific phases are distinguished: the *systole*, where heart undergoes contraction, and *diastole*, a relaxation period. Usually an heartbeat lasts almost 0.85 s (70 heartbeats per minute), where 1/3 of the cycle is characterized by the systole, while in the rest of it the diastole takes place [24]. In particular, for the left heart, different phases (Figure 1.6) are observed in the cardiac cycle, considering as initial condition a state where left atrium has been fully filled, the left ventricle has reached the minimum value of volume and the mitral valve is not open yet:

- **Ventricular filling**: in the moment that ventricular pressure is exceeded by the atrial pressure, due to inflation of blood, mitral valve

opens and blood starts flowing passively in the left ventricle, which relaxes and its volume increases. The ventricular pressure slowly increases.
After the 80% of this phase is completed, the process of ventricular filling becomes active (*atrial systole*), with the active contraction of the left atrium that slowly pushes in the ventricle the remaining blood. At the end of the atrial kick, the mitral valve closes since ventricular pressure is higher than the atrial one and the left ventricle has reached maximum volume.

- **Isovolumic contraction**: during this phase the active contraction of the ventricle takes place. As a consequence, the ventricular pressure increases and the mitral valve is closed, but also the aortic valve is closed, since the aortic pressure is higher. For this reason the blood volume keeps constant due to blood incompressibility.
  Elastic energy is accumulated.

- **Ventricular ejection**: in this phase the ventricular pressure reaches the aortic one (70 mmHg), so that the aortic valve opens and the blood starts flowing through the LVOT into the aortic root and into the systemic circulation. The ventricle keeps contracting, so its pressure still increases. Also aortic pressure increases, due to elastic adaptation to vessel wall. In summary, a pressure gradient between the two areas drives blood flow and it reduces for the active contraction, until ventricular and aortic pressure become equal (in that instant the *systolic peak* is reached with the maximum blood velocity. Then, there is the inversion of the sign for the pressure gradient and the blood deceleration, until the velocity is negative and the aortic valve consequently closes.
  The elastic energy is released, with the ejection of the blood due to a passive mechanical contraction for inertial effects (without an increase of the volume)

- **Isovolumic relaxation**: the elastic recoil after the closure of the aortic valve leads to a slight pressure increase in the aorta. Also, the elastic energy of the ventricle is still released, with both valves closed. So the volume does not change.

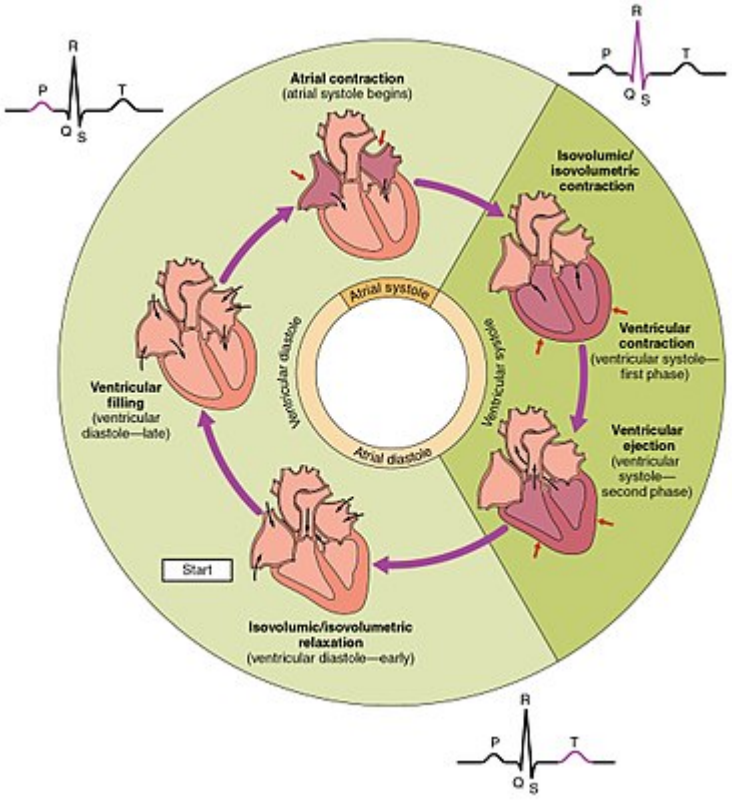

Figure 1.5: Graphical illustration of the cardiac cycle phases (https://en.wikipedia.org/wiki/Cardiac$_cycle$)

1.2.3 Global cardiac performance indicators

In cardiovascular physiology, in order to analyze the cardiac performance during the cycle and to gain a good amount of information about the efficiency of the global processes, some functioning indicators are computed and inspected.
The first one that is going to be presented is the *Wiggers diagram* (Figure 1.7) where, with respect to the X-axis, used to plot time, *blood pressure* in the aorta and in the left heart chambers, the *ventricular volume*, the *electrocardiogram* and the phonocardiogram are simultaneously plotted. The aim is to show and schematically describe the relation among the variation in time of these parameters, illustrating the coordination in every phase of the cardiac cycle. It is a relevant graph, since it is useful as reference for investigating the behaviour of the clinical markers in patient-specific cases. Indeed, it shows the instant when the pressure gradient between the aortic

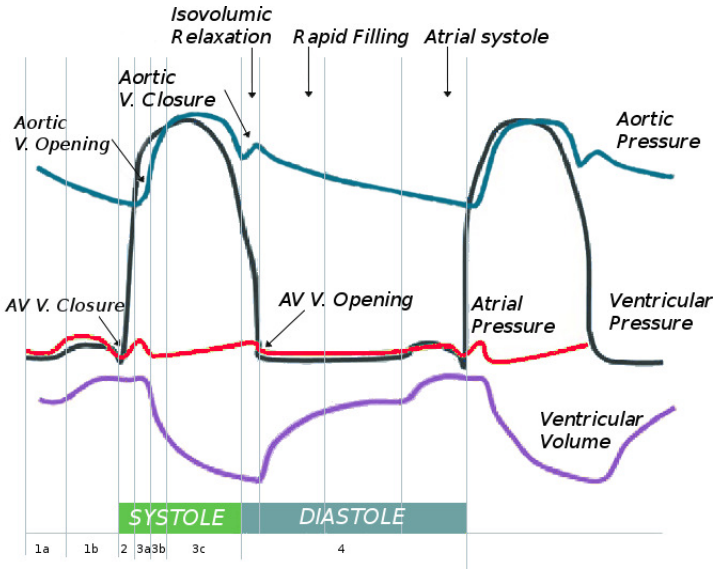

Figure 1.6: Aortic and ventricular pressure and aortic and ventricular volume behaviour during all the phases of the cardiac cycle [24]

root and the left ventricle is inverted, with the former that becomes higher than the latter. Moreover, it highlights the moments of opening or closing of the mitral and aortic valves.

The next indicators concern the cardiac efficiency in terms of pumping activity. They are obtained registering the blood volume in the left ventricle in the most significant instants, at the end of the systole and of the diastole:

- The *End Diastolic Volume* (EDV) and the *End Sistolic Volume* (ESV), highlighting the ventricular volume in those two instants (as shown in Figure 1.7 at the end of Isovolumic contraction and isovolumic relaxation, respectively). Physiological values of EDV and ESV are approximately 120 mL and 50 mL. Starting from the presented parameters, an additional one is evaluated:

- The *Stroke Volume (SV)*: the blood volume pumped in the ventricular ejection phase. It is computed as the difference between the EDV and the ESV:

$$SV = EDV - ESV$$

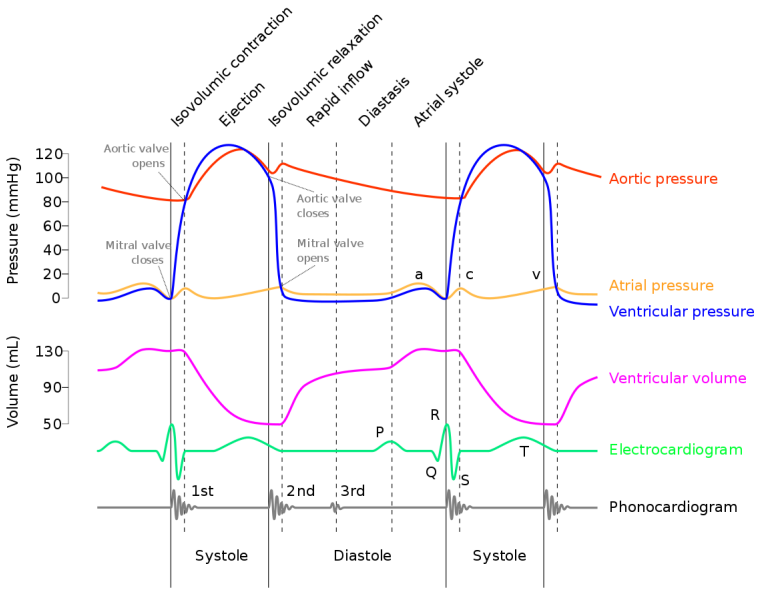

Figure 1.7: Wiggers diagram, showing the relation between the variation of blood pressure in every chamber and ventricular volume (https://upload.wikimedia.org/wikipedia/commons/9/91/Wiggers_Diagram_2.svg)

and its value, for a healthy patient, by the previous claims, approximately 70 mV per beat, but it usually varies in normal conditions in a range of 60-100 mL beat^{-1}.

- The *Cardiac Output (CO)*: the amount of blood ejected in the systemic circulation per minute, obtained as the product between the SV and the heart rate HR, the number of contractions per minute:

$$CO = SV \times HR$$

  It varies between 4 and 8 L min^{-1}.

- The *Ejection Fraction (EF)*: the volumetric fraction of EDV pumped into the circulation during the ventricular ejection phase in the systole. It is expressed in percentage as:

$$EF = \frac{SV}{EDV} \times 100$$

  It is a useful indicator to inspect the systolic function efficiency. A representative threshold value is 55%, that healthy patients exceed.

These parameters can be slightly affected by normal conditions (as age, usual habits or gender for example), while, in pathological cases, they can severely change as a consequence of possible modifications in cardiac tissues by means of alterations in contractility, cavities dimensions and myocardial stiffening.
An interesting physical principle, that consider the parameters illustrated above, is the *Frank-Starling law* of the heart, that is described in the Figure 1.8. It shows how the stroke volume and the telediastolic volume (EDV) are related: whenever the EDV increases, the more the myocites are stretched by the blood, causing a higher contraction force during systole, and an increase of stroke volume in response. The Frank-Starling law is an important clinical since it helps to gain a more global view about the cardiac functioning also due to the focus on the arterial blood supply and the venous return. In fact it describes a physiological mechanism between the left and right ventricles that clinicians take into account. Indeed, this law exploits a relation between the contractility power and heart and cells deformations, as in the description of aortic and mitral valve insufficiency (where the diastolic cells stretching overcomes the threshold of validity of the Frank-Starling law and the contractility, but, also, heart dilation due to retrograde flow leads to contractility power increase, applying the same law).

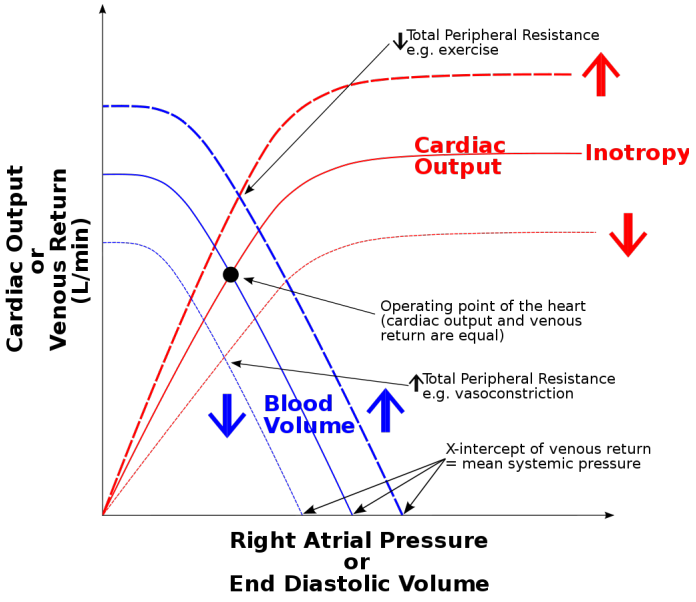

Figure 1.8: The diagram representing the Frank-Starling Law (https://it.wikipedia.org/wiki/Legge_di_Frank-Starling)

A final marker that is going to be presented is specifically related to the left ventricle and the cardiac cycle, the *pressure-volume loop* (PV loop) analysis, as a consequence of the pressure action in the blood flow and in heart contraction. The left ventricle pressure is plotted against the respective volume (right graph in Figure 1.9) and the loop is explained analyzing the sequence of processes occurring the cardiac cycle.

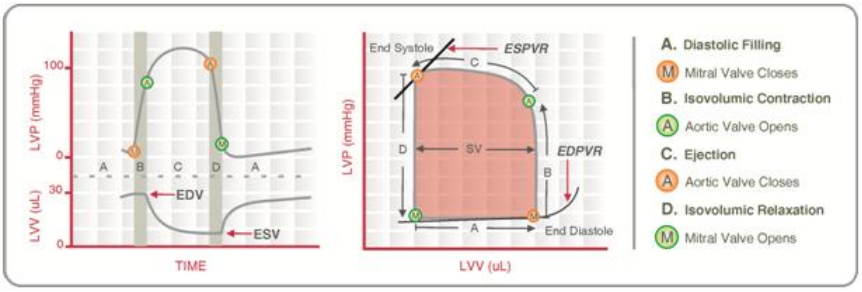

Figure 1.9: Pressure-Volume diagram modeled with respect to the cardiac cycle phases (https://en.wikipedia.org/wiki/Pressure%E2%80%93volume_loop_analysis_in_cardiology)

We can immediately notice the representation of the isovolumic phases of contraction and relaxation with vertical lines and the graphical description of the opening and closure of the valves as the corners of the diagram.
Moreover, the clinical relevance of this graph is in the analysis of the loop variations in pathological conditions (as with the cavity enlargement, the increased walls stiffening or the altered myocardial compliance), as in Figure 1.10, where it is inspected the effect of the increase of *preload* (the stretching of a single cardiomyocyte before contraction) and *afterload* (the main tension that the ventricle needs to apply in order to contract), respectively at the end of diastole and systole.

1.2.4 Left ventricle strains in the contraction phase

A fundamental tool that clinicians take into account in order to assess global heart functioning during the contraction phase is the evaluation of the left ventricle strains in three different spatial directions (Figure 1.11), that form a complex displacements pattern that dominates the ejection fraction and preserve physiological values (so, they are affected in pathological conditions):

- **Circumferential deformation**: the strain characterized by a change in length of the myocardium along the circumferential axis, due to the

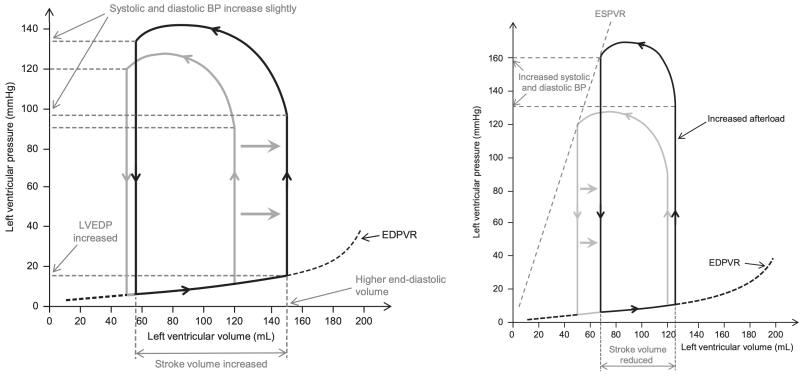

Figure 1.10: Left: Increased preload effect on the PV loop at the end of diastole (EDPVR: end-diastolic pressure volume relationship); Right: Increased afterload effect on the PV loop at the end of systole (ESPVR: end-sistolic pressure volume relationship) [48]

myocardial fibers shortening in systole. This effect is induced by the *twist mechanics* of the left ventricle, thanks to the counterclockwise and clockwise helical motions of, respectively, the apical and basal regions.

- Longitudinal deformation: it represents the shortening of the ventricle in the longitudinal direction, with negative strain. The plane containing the mitral ring moves from its initial end-diastolic position and the displacement is between 15-20%. This motion is crucial for the analysis of the LV systolic function, since it allows to keep a physiological value of EF. Otherwise, indeed, the ESV is higher than it should be in normal conditions and, consequentially, the EF decays (it could reach values less than 30%).

- Radial deformation: it is the consequence of the wall thickening of the myocardium and it is evaluated as the difference between the cavity radius in the actual configuration from the correspondent radius in the reference configuration, the end-diastolic position. The pattern is not regular, since lower displacements are detected in the area of the interventricular septum, while the greatest ones area measured in the lateral free wall.

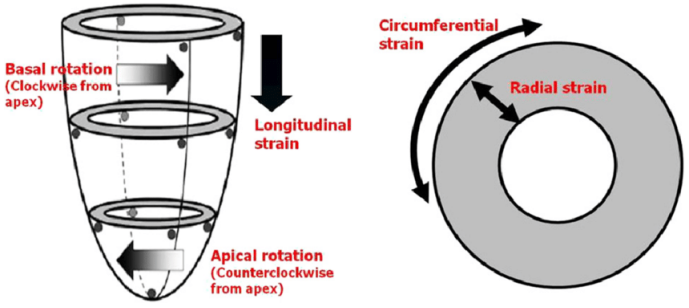

Figure 1.11: Representation of the LV deformations in the three spatial directions during heart contraction [49]

Chapter 2

Hypertrophic Cardiomyopathy: the clinical problem

In this section an overview of the Hypertrophic Cardiomyopathy is going to be provided, presenting also, a detailed description of the imaging techniques, in order to show pros and cons of the diagnostic tests and the difficulty of assessing the severity of the pathology. Furthermore an overview of computational methods in the framework of the cardiovascular system will be illustrated, in particular focusing also on relevant works in this area of research. Finally, the objectives of the present work will be explained.

2.1 The main aspects of Hypertrophic Cardiomyopathy

Heart muscle can be severely affected by pathologies that hit the structure and the functioning, the *cardiomyopathies*, due to enlargement, stiffening or weakening of the ventricle (*hypertrophic*, *dilated*, *restrictive*). LV generally could suffer more of one of these conditions than RV. In the worse cases, cardiomyopathies could lead to heart failure, plaques formation and sudden death. They could be asymptomatic in the early phases, while, generally, are characterized by the presence of sympthoms as shortness of breath, fatigue, irregular heartbeat and swelling of the legs, all signs of possible incoming heart failure.
When cardiomyopathies determine a lower blood pumping, with respect to

the amount needed by the body (fundamental in terms of nutrients and oxygen supply), the heart needs to keep normal values of cardiac output, so it increases his frequency (*tachycardia*), and, also, it increases the diastolic filling in order to compensate the lower amount of ejected blood and to increase the stroke volume. But tachycardia has negative energetic effects for the heart, leading to abnormal cells stretching and invalidation of Frank-Starling law.
In conclusion, the mechanism will be no longer correctly functioning and the cardiac output decreases in a drastic way. As result, the heart failure shows up.
The treatment of a cardiac pathology depends on the severity of the condition, the age of the patient, his lifestyle and his health status. Indeed, non invasive therapies, with the simple changes in the lifestyle or pharmacological treatments could be proposed for the less severe cases, while surgical procedures could be necessary for the worse ones.

Before starting the description of Hypertrophic Cardiomyopathy, it is useful to understand the main aspects regarding another type of it, the **Dilated Cardiomyopathy**: it is characterized by the thinning of the ventricular wall (since the cardiomyocites are partially replaced with fibrosis and small scars), leading to an excessive enlargement and weakening of the ventricular walls. The outcome is pathological heart contraction and an insufficient blood ejection. **Hypertrophic Cardiomyopathy** (HCM) is a condition affecting the interventricular septum and the left ventricle, with the abnormal wall thickening in the heart muscle. As result, the ability of pumping blood is hit and the ejection fraction strongly decreases. Moreover, a phase shift between the mechanical and the electrical activity is recognized in the detection of the end-systolic and end-diastolic instants.
The causes of the HCM are different and comprehend genetical inheritances from patient's parents, mutations in specific genes in the production of heart proteins, hypertension or cardiac remodeling. HCM is the most common type of cardiomyopathy, since it affects about one in 500 people [26].
The severity of the pathology depends on many factors, but the risk of suffering cardiac death increases when the wall thickening (with peaks of $30 - 35mm$) is even more excessive.
The pattern is different from patient to patient, since it could involve the whole myocardium or local portions of it. Usually, the interventricular septum is the most affected position, where the highest values of thickening are detected. Since, for the most, patients with HCM suffer of this condition is restricted areas of the myocardium, this pathology is also described as

asymmetric.
An effect of HCM is the increase blood pressure due to wall thickening, that leads to the insufficient filling of the ventricle. Furthermore, it hits also the myocardial fibers, since their orientation is not physiological and coordinated (*electrical disarray*).
In Figure 2.1 the differences in the anatomy between a normal heart and a cardiomyopathic one can be noticed.

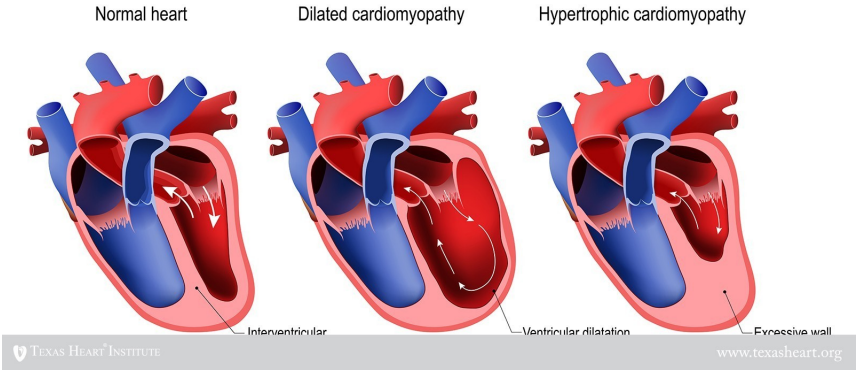

Figure 2.1: The comparison between a normal heart with the two main types of cardiomyopathies (https://www.texasheart.org/heart-health/heart-information-center/topics/hypertrophic-cardiomyopathy/)

2.2 Treatment of Hypertrophic Obstructive Cardiomyopathy: a surgical approach

In some cases, the distortion of the heart anatomy can lead to a worse condition, where the *Left Ventricle Outflow Tract* (LVOT) is obstructed: as result, the combined effect of the asymmetric septal hypertrophy and the subaortic stenosis, leads to blood pressure drop in the aortic root (causing high pressure gradients), increased jet velocity and excessive values of *Wall Shear Stresses* (WSS). For this reason, HCM can be classified in two variants, the obstructive one (*hypertrophic obstructive cardiomyopathy*, HOCM) and the non-obstructive one.
HOCM could be associated in some cases to a *Systolic Anterior Motion* (SAM), which is the displacement of the distal portion of the anterior leaflet

of the mitral valve towards the LVOT. This pathologic motion leads to a possible severe narrowing in the outflow tract in the ejection phase, when the aortic valve is open, affecting the hemodynamics in the LVOT.
HOCM is usually caused by an autosomal dominant genetic disorder in about 60% of detected cases, while the other ones are most of all the consequence of unconstrained mutations. With the respect to the non obstructive HCM, the thickening of the myocardial muscles cells is more abnormal, determining a worse alignment of the myocites and a worse *myocardial disarray*. In conclusion, the risk of heart failure is higher, most of all due to *diastolic disfunction*, *mitral regurgitation*, *arrhythmia* or "*burnt out HOCM*" (systolic disfunction during end-stage HOCM) [27].
In the most severe cases of HOCM a surgical procedure is applied to the patient by the clinicians, choosing treatments as *septal myectomy* (surgical removal of the enlarged interventricular septum portion, causing the obstruction in the LVOT), that represents the gold standard for the treatment of HOCM sympthoms. The aim is to improve the systolic function, increasing the stroke volume and the ejection fraction, and to preserve the efficiency of the mitral valve from the risk of possible damages.
By indication of ESC guidelines, septal resection is a tricky procedure that it must be performed only by highly experienced multidisciplinary teams, in order to ensure an acceptable surgical risk.
There are three different approaches for septal myectomy, with the general idea of resecting a portion of the septal myocardium, removing at least 1 cm depth of muscle [30]:

- *Transaortic extended septal myectomy* (TAESM): the most common method, associated to low mortality rate, characterized by a relevant extension of the septum cut

- *Transmitral septal myectomy* (TMSM): a technique that ensures a wide view of the septum, preserves the aortic leaflets and, possibly, detects abnormalities in the mitral valve

- *Complete septal myectomy*: the most applied method in case of simultaneous SAM and mitral insufficiency

The postoperative results for each one of the three surgical treatments are relevant, since the LVOT is opened and the pressure gradient is significantly reduced.

2.3 Diagnostics: the Magnetic Resonance Imaging

The detection and diagnosis of the hypertrophic cardiomyopathy in its early stages is crucial for the treatment of the pathology. The primary tests that are executed for suspected cases of HCM are *Transthoracic Echocardiography* (*TTE*) and the cardiac *Magnetic Resonance Imaging* (*MRI*), both non-invasive techniques for the assessment of the overall state of the heart.
TTE is a test characterised by the use of a probe, placed in the chest or abdomen of the patient, that, due to ultrasounds, allows the capture of images of the heart in different views. The main property of this technique is the surface modality of the examination: ultrasound waves need to cross the skin and the soft tissues in order to reach the heart and allow image-capturing. This leads to important limitations and inaccuracies for the final output of the test, since the deepest structures with respect to the skin have an inferior visualization quality than the ones which are closer to the skin.
MRI is an imaging technique that captures the structure and the physiological function of the heart through scanners that uses strong magnetic fields and magnetic field gradients (which localize the magnetic resonance signal) and radio waves in order to recover different visualizations of the anatomy of the heart, based on the direction variation of the magnetic field. From this test different frames (*slices*) of the same area of the heart are recovered in several instants of a heartbeat. As a consequence, the evolution in time of the cardiac structures can be recovered (**cine-MRI**).
The starting point of the present work is based on the MRI technique, since it is the one that provides the initial data for the geometrical reconstruction of a 3D model of a patient-specific left ventricle for a whole heartbeat, thanks to which it will be possible the mathematical and numerical description of the problem.
The patient is place in a MRI scanner, where he undergoes a strong magnetic field. The hydrogen nucleus, that behaves like a bar magnet (spinning on its axis), reacts due to the body's natural magnetic properties and all the protons realign, with the respective axes all lined up uniformly. As a consequence, a magnetic vector oriented is generated, with the same orientation of the MRI scanner axis. Then, a radio wave is added to the magnetic field and a deflection of the magnetic vector occurs, with the strain against the pull of the field of the protons. When the radio-frequency source is switched off, the vector returns to its resting state (*relaxation*), thanks to the MRI sensor that recognize the energy released by the protons in the previous step. In this phase a signal is emitted, cross-sectional images are reconstructed and the signal is plotted on a grey-scale, based on its intensity [28].

The main parameter that determine the intensity of grey of each pixel is the realignment time of the protons: the lower the latter is (and so the realignment of the magnetic vector and of the axial spin is faster), the brighter the images are.
Since a cardiac MRI test is executed through a series of pulse sequences and most of the tissues have different realignment times, it is possible to distinguish and separate them for different substances: for example, hydrogen nucleus is characterized by an high concentration of fat and water, so, in order to not consider the signal from the adipose tissue (or to detect adipose tissue), a specific technique as *fat suppression* can be applied. The property of distinguishing different tissues is one of the pros that allow MRI to be used also to detect different pathologies, regarding the aortic valve, the coronary artery or the pericardium.
The final 2D MRI output image series are provided with the following visualizations, as long as the acquisition plane varies:

- **Short-axis view**: the biventricular short-axis in the heart is the plane perpendicular to the long axis of the heart, that coincides with the axis aligning the basal and the apical regions. It provides, for each instant of time, a three-dimensional representation through parallel slices (upper-left image in Figure 2.2), while the following views consist in a single 2D slice.

- **2 chambers view**: the first of the three long-axis views, that is achieved by rotating the images perpendicularly to the mitral valve and parallel to the cardiac septum, obtaining an overview of the LA and LV and the mitral valve (upper-right image in Figure 2.2).

- **3 chambers view**: second long-axis visualization that is reconstructed in the instants when border between the mitral and aortic valves is localized on the axial slices and the images are rotated from this point. The output is an overview of the LV, the LA, the proximal ascending aorta and the two valves (bottom-left image in Figure 2.2).

- **4 chambers view**: the final long-axis view, achieved by rotating upwards from the apex of the heart on the axial slices. In this axis, the right ventricle is projected next to the right atrium, and the left ventricle next to the left atrium (bottom-left image in Figure 2.2).

Due to the high spatial resolution, the possibility of detecting different tissues and the three dimensional information produced by the short-axis images, cardiac MRI is the most recommended technique for assessing the

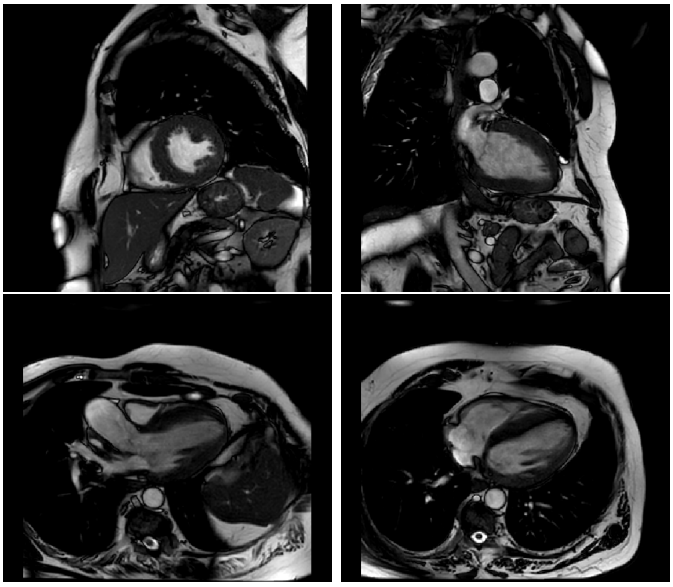

Figure 2.2: Four types of MRI visualizations. Upper-left: short-axis view; Upper-right: 2 chambers view; Bottom-left: 3 chambers view; Bottom-right: 4 chambers view (clinical images provided by L. Sacco Hospital in Milan)

severity of hypertrophy in the heart walls, since the reconstruction of the wall thickness and the corresponding measurement is crucially accurate. Instead, TTE has an important liability in diagnosing the lateral and apical hypertrophies.

On the other hand, MRI is a technique with some non-negligible disadvantages: the patient needs to be fully cooperative, since it undergoes a long process (up to 1 hour), where it is fundamental to stand still and breath-holding several times in the acquisition phase of each slice, in order to get output images without spurious artifacts and blurs, corrupting the results. For this reason, most of all with claustrophobic or old patients the risk of providing unusable images is very high.

Also, another important disadvantage is due to the very high low resolution between slices in the volumetric series of MRI, since the slice thickness is in between 6 and 8 mm, depending on MRI scanners, with 2–4 mm of interslice spacing gaps, leading to a final value of 10 mm [29].

2.4 Overview on the computational methods for heart function modeling

The mathematical and numerical models for the cardiovascular system are divided into two macro-categories: the one concerning the arterial circulation and the one regarding the heart function modeling.
In the first case, the most important model known from the literature consists in the connection of the fluid-dynamics problem for the hemodynamics in the lumen and the mechanics problem for the vessel wall: the final coupled model is a *Fluid-Structure Interaction* (FSI) problem. The fluid-dynamics equations are represented by Navier-Stokes for incompressible Newtonian fluids [31][32][33] or non-Newtonian ones [34][35] in an Eulerian framework, where the fluid domain Ω_f is a three-dimensional time-varying domain and the solutions are the fluid velocity $\boldsymbol{u}$ and the fluid pressure p. Providing suitable boundary and initial conditions, the described system allows to perform a CFD study for the blood flow.
Instead, in order to model the structure behaviour, a mechanic wall problem is introduced. It consists of an elastodynamics equation (usually with a non-linear finite elastic law) that models the deformation of the lumen wall with a Lagrangian approach. The corresponding equations are written in the reference configuration (Lagrangian configuration). The solution is the structure displacement $\boldsymbol{d}$.
The final FSI problem is obtained coupling the aforementioned equations with the relative boundary conditions via the modeling of the interaction at an interface Σ that represents the lumen boundary through matching conditions that must be enforced: the kinematic condition (continuity of velocities), the dynamic condition (continuity of the normal stresses) and the geometric condition (geometry adherence between the domains). The coupled FSI problem reads:
Find $\boldsymbol{u}$, p, $\boldsymbol{d}_f$ *and* $\boldsymbol{d}$ $\forall t > 0$, *such that, given the proper boundary and initial conditions* :

$$
\begin{cases}
\rho_f \partial_t \boldsymbol{u} + \rho_f (\boldsymbol{u} - \boldsymbol{u}_f) \cdot \nabla \boldsymbol{u} - \nabla \cdot \boldsymbol{T}_f(\boldsymbol{u}, p) = \boldsymbol{0} & x \in \Omega_f, \\
\nabla \cdot \boldsymbol{u} = \boldsymbol{0} & x \in \Omega_f, \\
\boldsymbol{u} = \partial_t \boldsymbol{d} & x \in \Sigma, \\
\boldsymbol{T}_f(\boldsymbol{u}, p)\boldsymbol{n}_f = -\boldsymbol{T}_s \boldsymbol{n}_s & x \in \Sigma, \\
\rho_s \partial_{tt} \hat{\boldsymbol{d}} - \nabla \cdot \hat{\boldsymbol{T}}_s = \boldsymbol{0} & x \in \hat{\Omega}_s, \\
\hat{\boldsymbol{d}}_f = \hat{\boldsymbol{d}} & x \in \hat{\Sigma}, \\
-\Delta \hat{\boldsymbol{d}}_f = \boldsymbol{0} & x \in \Omega_f.
\end{cases} \tag{2.1}
$$

where $\mathbf{T}_f$ is the fluid Cauchy stress tensor and $\hat{\mathbf{T}}_s$ is the Piola-Kirchhoff tensor.
The FSI problem is a model that is applied also in the heart function modeling, considering the interaction between the hemodynamics in a heart chamber and the elastic law for the myocardial wall.

2.5 Objectives of the work and State of The Art

In the present work the aim is to carry out a *Computational Fluid Dynamics* study of cardiac hemodynamics for patients affected by HCM. Recently, many research groups have focused efforts into the challenging tasks of developing a simulation of the blood flow in the heart, but the idea of using computational hemodynamics approaches to analyze the consequences of HCM is not common in the literature. Indeed, to the best of my knowledge, this topic has been discussed only by Kudriavtsev [17], Nardi et al. [20], that proposed a numerical study for the treatment of HCM by means of template geometries, and in two works that focused on hypertrophic obstructive cardiomyopathy (HOCM) associated with *Systolic Anterior Motion* (SAM). In the first one, performed by Meschini, Mittal and Verzicco [45], an FSI approach is applied, while the second one, by Deng et al. [46] is a CFD study. Other than that, it is necessary to point out that this work is linked to the paper of Fumagalli et al. [2], where cardiac hemodynamics is inspected numerically by means of CFD in a moving domain, with prescribed left ventricle displacements reconstructed from cine-MRI data, in order to assess the severity of hypertrophic obstructive cardiomyopathy (HOCM) associated with *Systolic Anterior Motion* (SAM) of the mitral valve. Moreover, the reconstruction pipeline for patient-specific geometries is a reworked and improved version of the pre-existent one proposed in [2].
For what concerns the modeling of the hemodynamics in the left ventricle,

the physical problem requires to define a computational domain and prescribe suitable boundary conditions. For the segmentation, an image-based segmentation procedure is taken into account, starting from *Magnetic Resonance Imaging* (*MRI*) data and constructing a 3D-representation. For the boundary displacement, a sequence of 3D level-set images provided with temporal evolution are elaborated from the initial data and considered into the problem.
The idea of prescribing the motion in a suitable way for the computational description of blood fluid-dynamics follows from the results obtained by Donea, Giuliani, and Halleux [9], Dedé, Menghini and Quarteroni [10], Tagliabue, Dedé, and Quarteroni [11] and Masci et al. [12]. On the other hand it is important to cite the works by This [13] [14], that was relevantly influential for the segmentation and reconstruction of the moving domain.
In general, for the blood flow analysis for the hemodynamics of the left ventricle, two main computational approaches are currently the most adopted:

- The *Fluid-Structure Interaction* (FSI) approach: remarkable works proposing FSI models are for example Gao et al. [1], Feng et al. [4], Kunzelman, Einstein, and Cochran [3], Ma et al. [5], Su et al. [6], Lassila et al. [7], Kaiser, McQueen, and Peskin [8] and [45]. The main characteristic of this framework is the modeling in pathological conditions of the complex mechanics of the the myocardium and, possibly, the mitral valve structure (with its subvalvular apparatus and calibrating its complex rheological properties). This implies high computational costs.

- The CFD approach: a different study that allows to deal with reduced complexity and higher computational costs due to image processing. Important works to be cited are [2], [13], [46], [20], Canè et al. [15] that focused more in the assessment of the left ventricle torsion as clinical biomarker or Su et al. [18] and Su et al. [19] that shifted the center of the attention more on the vortexes formation due to the presence of the valve.

The CFD analysis that is going to be proposed in this work relies on proposing a mathematical model based on Navier-Stokes equations for a moving domain with an *Arbitrary Lagrangian Eulerian* (ALE) approach, where the mitral valve is accounted for as an immersed surface and modeled by applying a resistive method, the *Resistive Immersed Implicit Surfaces* (RIIS) method (Fedele et al. [21]), consisting in the use of an additional term, that penalizes the kinematic condition (i.e. the blood needs to be adherent to

the valve surface). Resistive methods have been introduced in this framework by Astorino et al. [22] and Fernández, Gerbeau and Martin [23]. The main advantage of this method is the possibility to apply a 0D-model of the mitral valve, reducing the computational costs, without the need of considering its complex structure and dynamics by means of a 3D-model based on a surface-conforming mesh.
Moreover it is useful to stress that in this work, with respect to the other CFD studies mentioned above, the geometry reconstruction phase does not rely only on short-axis acquisitions, but it consists in the merging of the short-axis and long-axis visualizations, improving the final representation of the endocardium and its accuracy. The main aspects that are going to be discussed in this thesis are:

- The description of a novel reconstruction pipeline for patient-specific computational domains, that has been realized owing to MOX laboratory, consisting in the elaboration of standard diagnostic cine-MRI data to obtain the geometries and the relative motions, and finally applying the procedure for two patients that suffer from HCM
- The mathematical and numerical modeling of the blood flow in the moving domain (that will consist of the left ventricle and the ascending aorta), with the prescribed left ventricle displacements and the mitral valve modeled as an immersed surface with a resistive method; then the spatial and time discretization (respectively with a three-dimensional Finite Element Method (FEM) and a semi-implicit Euler method) of the problem will be performed
- The post-processing analysis, providing clinical indicators in order to assess the condition of the two patients and the severity of HCM, with the aim of supporting clinicians in the decision-making phase for the treatment of the pathology; in particular velocity, pressure gradients and Wall Shear Stress (WSS) will be evaluated to detect the effects of HCM in the two cases and these output results will be compared to the corresponding parameters of a patient suffering from SAM

Chapter 3

A novel reconstruction pipeline for the geometry and the input data

In the first section of the procedure that is going to be presented, the goal is to take into account the standard cine-MRI acquisitions and elaborate it in order to determine the three-dimensional moving domain along with the displacement fields associated to several instants of a heartbeat for each point of the geometry. Since the aim is to support clinical decision-making, it is crucial to calibrate the CFD study for common practice medical imaging, avoiding the use of more complex and advanced clinical MRI data, with specific acquisition protocols.
The pipeline will consist initially into processing the short-axis volumetric acquisitions, improving the resolution from the point of view of the slices thickness by applying a *Short-Long Axis Merging* (SLAM) algorithm. Then, through a semi-manual segmentation procedure the 3D myocardium is reconstructed and the deformation of the left ventricle is captured from the variation of the wall thickness for the whole cardiac cycle. In the next step the reconstructed computational geometry is connected to the initial tract of a template ascending aorta tract. Since in this work We have simulated only the systolic phase, for the purposes of the present work the mitral valve will be taken from a template and modeled as closed. Furthermore the mesh generation phase and its main computational aspects are going to be presented, with the description of steps leading to the exportation of the volumetric hexahedral mesh, that will represent the domain in the reference configuration in the simulation of the left ventricle hemodynamics. Finally, the imaging results of the aforementioned reconstruction pipeline will be

shown for two patients suffering from HCM.

3.1 The Short-Long Axis Merging algorithm

In order to deal with a CFD study of ventricular hemodynamics of patient-specific cases, firstly it is necessary to define the computational domain and compute the relative displacements for its temporal evolution. As initial step the clinical cine-MRI images, provided by L. Sacco Hospital of Milano, are considered. The image set consists in short-axis and long-axis series, each one of those is relevant in terms of diagnostics of the pathology. In particular, the former yields the only volumetric information about the left ventricle anatomy and dynamics through parallel slices of high resolution and representation accuracy (in the case of a cooperative patient).
The reconstruction pipeline applied by Fumagalli et al. [2] consisted in the segmentation of the 3D domain directly from the short-axis images. One of the main disadvantages of using these visualizations is the low resolution between each parallel slice, as explained in the section 2.3, since each one of the provided acquisitions has a thickness of $8mm$.
As a consequence, it is difficult to catch some important effects of the heart contraction, as the longitudinal shortening of the base of the ventricle, which could undergo a lower displacement per instant of time than the thickness of a slice. For this reason the ring that delimits the basal region could move in a portion of space included between two slices and the deformation is not captured.
In the present work we consider the *Short-Long Axis Merging* (SLAM) Algorithm, proposed in the work of Pase [57], which exploits the high resolution of of the base-to-apex section of the long-axis MRI series, merging those information into the short-axis visualization, obtaining as final result a *merged image*. Indeed, the long-axis acquisitions carry important information about the contour of the endocardium and the epicardium in a single slice. The two-dimensional nature of this type of series, instead, is the disadvantage that needs to be overcome with the short-axis volumetric information.
The procedure provides two important advantages with respect to other image processing strategies that have been introduced in other CFD studies, presented in the Section 2.5. Firstly, the possibility to catch the shortening of the base of the ventricle during the systole. Secondly, a more accurate segmentation phase regarding the identification of the surfaces of the epicardium and the myocardium.
Each acquisition of the MRI series is in the DICOM format (as in computed

tomography and in radiography). Every file contains information about name, scanner settings, the series, etc., each one of those defining an attribute of the DICOM image. The SLAM algorithm consists initially into the partition of the information in each DICOM file into two parts through a specific tool, the Matlab Image Processing Toolbox:

- The first one stores into a matrix the grey scale integer values of every pixel of an image
- The second one stores a structured array with the remaining fields and the respective values

The partition allows to preserve the image pixel data, allocated in a matrix that is independent of the remaining metadata structured array. As a consequence, it is possible to perform operations with the MRI sequences without losing information about the single grey scale integer values.
The SLAM algorithm assigns a new value for the thickness field of each slice of the short-axis series, 1 *mm*. As specified before, this operation does not impact on the image pixel matrix. Afterwards the procedure defines new slices, with the same value of thickness, to be located between the original short-axis slices. The aim is to obtain a final visualization where the spacing in the basal-apical direction is similar to the resolution of the slices.
In order to get one merged image per time instant, it is fundamental to bring together the short-axis and long-axis sequences, which have a different number of frames (20 for the short-axis series, 30 for the long-axis one), by detecting the time instants that both have in common and fixing one of them.
Then it is possible to generate the new slices (setting their thickness to 1 *mm*), by firstly copying the metadata structured array from an original slice and defining a null matrix with size given by the image dimensions, and then by modifying two position fields from the metadata structured array:

- *Image Position Patient* (IPP): the field containing the coordinates of the origin of the patient reference system, represented by the center of the first entry of the matrix storing the intensity of each pixel (Figure 3.1).
- *Image Orientation Patient* (IOP): the field containing the 6 components of the two unit vectors (identifying the column and row directions in the slice plane) that allow to locate the new slices in the patient reference system in the 3D space (Figure 3.1).

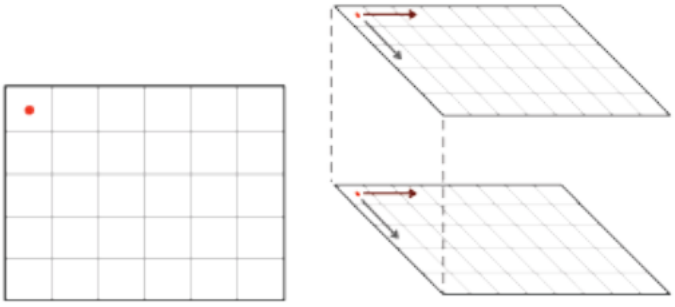

Figure 3.1: Left: the field Image Position Patient containing the coordinates of the origin of patient reference system [57]; Right: the field that carries the information of the component of the two vectors for the correct positioning of the new slices in the 3D space [57]

Subsequently 7 new slices are inserted between the original short-axis ones (since for the latter the thickness is 8 mm for all the patients that are going to be considered), as represented in Figure 3.2. In this phase the field *Number of slices* from the metadata is modified too.

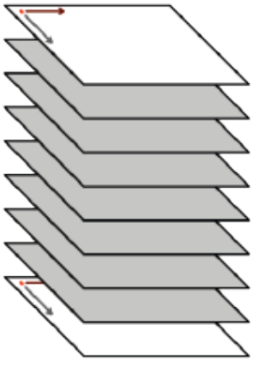

Figure 3.2: The merged image is generated by positioning correctly 7 new slices between the original short-axis ones

In the final phase the SLAM algorithm computes, in the patient reference system, for each pixel p of the new slices with its 3D coordinates the grey scale integer values in the intensity matrix (Figure 3.3. The idea is considering a sphere $\boldsymbol{S}$ centered in p with radius $R = T - \epsilon$ ($\epsilon > 0$, with T identifying the thickness of the short-axis), ensuring that the sphere contains the projections p_i ($i = 1, 2, ..., n$) onto the previous and next short-axis slice. Each projection p_i is associated to the corresponding value of grey scale intensity

v_i. At this point the algorithm fills each pixel with a given value of grey intensity v_{new}, obtained as the following weighted average (that in the worst case is obtained with the projections onto the two original shot-axis slices):

$$v_{new} = \frac{\sum_{i=1}^{n} v_i \omega_i}{\sum_{i=1}^{n} \omega_i} \tag{3.1}$$

where each weight is computed as $\omega_i = R - |p - p_i|$ As a result, starting

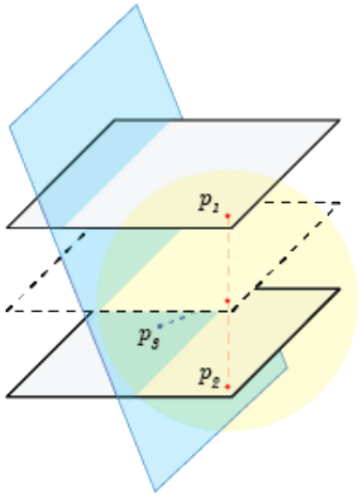

Figure 3.3: A grey intensity value is assigned by the algorithm from the weighted average with the grey values of the projections onto the nearby slices with respect to the considered short-axis slice (lying into a sphere of radius T - ϵ

from the MRI short-axis series (represented at the left in Figure 3.4), adding the information of the long-axis acquisition, a merged image with a higher accuracy in the contours and a better resolution in the basal-apical direction is obtained (right image in Figure 3.4). This approach leads to a more precise identification of the basal region of the left ventricle (that represented the main weakness in the pipeline proposed in [2] for the image-processing phase) and to an improved segmentation of the geometry.

3.2 Left ventricle geometry and motion reconstruction from cine-MRI data

After the first step of the computational pipeline, consisting into merging the MRI short-axis and long-axis acquisitions, in the next phase the main task is the segmentation of the endocardium and the epicardium from the

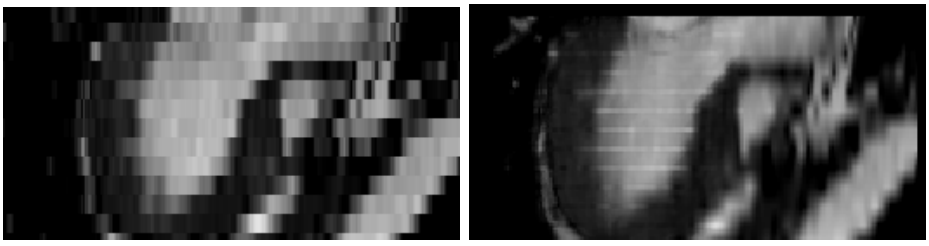

Figure 3.4: $Left$: An MRI short-axis series slice; $Right$: merged image resulting from the SLAM Algorithm (clinical images provided by L. Sacco Hospital in Milan)

artificial merged images, which are an enriched visualization of the 3D original short-axis representation. In the work [2], in order to fully catch the shortening or stretching of the left ventricle during the heartbeat and the motion of the aorto-mitral annulus, it was not possible to perform only a segmentation of the endocardium from the 3D short-axis image, due to the low resolution of the latter. For this reason, subsequently, it was necessary to model as a function in time the distance between the base and the apex of the left ventricle from the 2D long-axis image. The function was obtained by manual measurements and, coherently with it, the segmented endocardium was cut at the base. Afterwards the geometry could be ready for the modeling of a high resolution level-set image and for the following registration algorithm.
On the contrary, extending the pipeline of [2] and applying the procedure described in the section 3.1, the segmentation of the merged images allows already to capture the motion of the base and the shortening/elongation of the LV, which are relevant factors in the contraction and relaxation phases. In the following subsections, the steps of the reconstruction pipeline of left ventricle geometry with its local displacements are going to be presented, including the output results obtained for one of the HCM cases analyzed in this work.

Segmentation of the 3D endocardial and epicardial surface from the merged images

For this second step the endocardial surface (extended until the aortic region) and the epicardial one are reconstructed for each enriched artificial clinical image (one per time instant) and the two resulting geometries are intersected, in order to obtain the final endocardium together with the ventricular base. The tool that has been employed for the segmentation is the

Medical Image Toolkit (MITK) [www.mitk.org][50][51].
Thanks to the improvement brought by the SLAM algorithm, the segmentation method does not affect the pipeline, as long as the reconstruction of the aorto-mitral annulus is accurate. In this work the applied procedure consists in the partition of the ventricle from the merged image into multiple 2D subsets which are orthogonal to the base-to-apex direction and are made by a set of pixels. The identification of the 2D areas is a manual procedure, that relies on the accuracy and the level of detail of the contours of the ventricle (that Section 3.1 ensures). The endocardium and part of the aortic tract cross sections are selected tracing the edges of the bright portions within the left ventricle, including the dark parts representing the papillary muscles. This choice derives from the approximation of the left ventricle as an ellipsoid in clinical estimates and the idea to keep an acceptable level of smoothness in the reconstruction of the geometry, in order to avoid a heavy impact in terms of computational costs during the simulation phase.
The epicardium sections, instead, are obtained by selecting the border of the darker area surrounding the endocardium.
The final 3D surfaces, in the end, are created by the MITK applying a 3D radial basis interpolation algorithm relying on the intensity of the visualization and the two dimensional contours [50][51] (in Figure 3.5 the two surfaces are highlighted in MITK, while in Figure 3.6 a cross section of them is represented using ParaView [www.paraview.org]). The two output files are in the *.vtp* format.

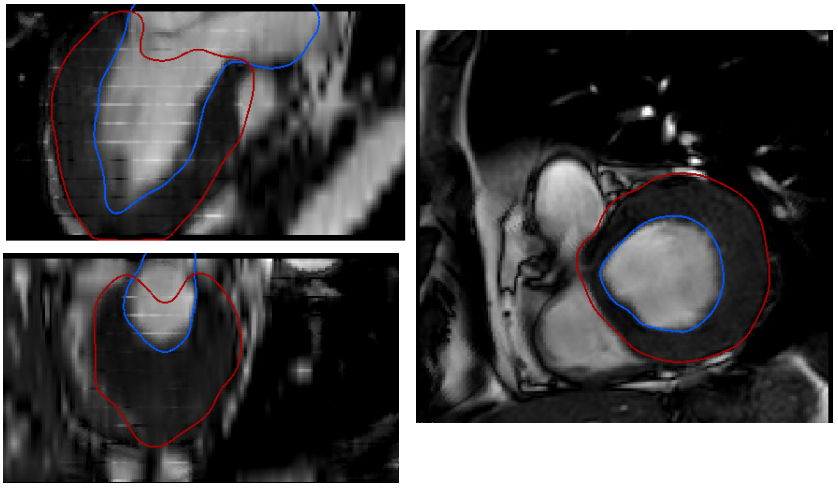

Figure 3.5: 3D epicardial and endocardial surfaces segmentation (MITK visual outputs) (clinical images provided by L. Sacco Hospital in Milan and segmented with MITK) [www.mitk.org]

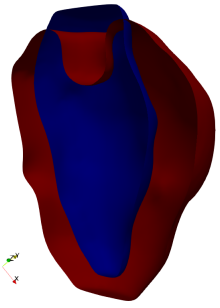

Figure 3.6: Cross section of the endocardial (blue) and epicardial (red) segmented surfaces (obtained using ParaView) [www.paraview.org]

Generation of the 3D myocardial surface

In the next step of the reconstruction of the left ventricle geometry, the outputs of the segmentation of the merged images, the endocardial and epicardial surfaces, are processed and intersected with semi-automatic tools hinging upon the Vascular Modeling Toolkit (VMTK) [52] and the Visualization Toolkit (VTK). The result is the creation of a myocardial surface, for each time instant, partitioned in three parts: the epicardial and endocardial parts and the valvular ring (Figure 3.7). Applying a pipeline based on VMTK, the two inputs surfaces are connected and for each of the three portions a tag is assigned. The identification of a valvular ring and its deformation in time allow to reconstruct the motion of the ventricular base and to capture the systolic shortening and the diastolic elongation of the left ventricle. This possibility derives from the insertion of new slices between two original MRI short-axis slices, improving the resolution of the short-axis image and ensuring a more accurate representation, for each time instant, of the basal region and, consequently, of the valvular ring. For this reason the manual measurement of the base-to-apex distance in time can be avoided, as the cuts of the endocardial surfaces, reported in [2].

Generation of the 3D level-set images of the myocardium

Afterwards, relying on the same pipeline hinging upon VMTK, the 3D surfaces, representing the myocardial configurations at every different time instant corresponding to each frame of the merged image series, are processed and modelled in order to convert each of them in a volumetric level-set im-

age. The image contains the signed distance transform from the surface points and it is obtained by assigning to the VMTK command that performs the surface modelling, among all the parameters, the one regarding the spacing, that is 1 mm for every direction in the 3D space.

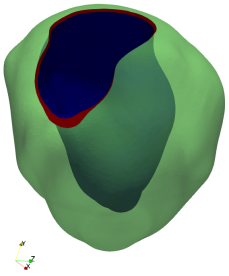

Figure 3.7: Reconstruction of the myocardium, highlighting the endocardial (blue) and epicardial (green) portions and the valvular ring (red) (visualization obtained using ParaView) [www.paraview.org]

The level-set images are composed by two types of file: the $.zraw$ format, where all the image data are compressed, and the $.mhd$ one, that is a header file, called *segmentation mask*. As highlighted in Figure 3.8, the brighter portion emphasizes the epicardial slices, while the internal darker side coincides with the endocardial portions. The idea of generating level-set images, together with their binary nature, derives from the goal of performing an image registration procedure without taking into account standard acquisitions.

Application of a registration algorithm among the level-set images

Indeed, after reconstructing the myocardial images at different time instants, the aim now is to register them. The following process consists into assigning a reference frame and recovering the geometrical transformations of each image the into the reference one, so introducing a common coordinate system. The idea is to represent each pixel of the image as the correspondent biological point and assigning to the homologous point its local displacement from the moving configuration to the reference one. The goal of the registration then is to find the function T that maps each pixel of the moving image to correspondent one of the reference frame. In Figure 3.9 the registration process is highlighted and schematically reproduced.
The procedure that is applied hinges upon SimpleITK [simpleitk.org], that relies on the SimpleElastix software package. The procedure of mapping

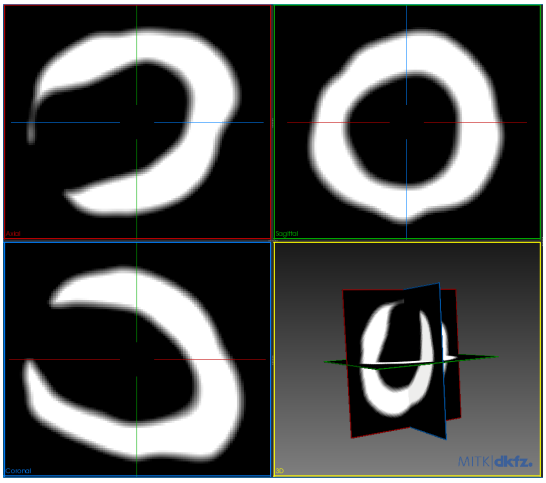

Figure 3.8: Volumetric representation of the level-set image of the reconstructed myocardium (visualized with MITK) [www.mitk.org]

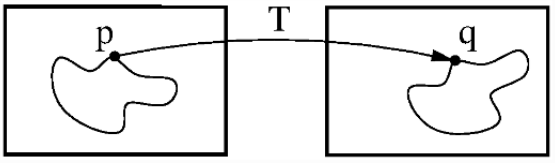

Figure 3.9: Considering a point p of the moving image, the function T maps p into the point q of the fixed frame (image taken from https://simpleelastix.readthedocs.io/_images/ImageRegistrationConcept.png)

the moving frame to the fixed image relies on the application of a similarity metric, a quantitative criterion that measures the level of match between the two input frames. The algorithm solves an optimization problem over the search spaces of parameters of the transform. The aim is the minimization of a cost function C with respect to the deformation map T, where the cost function is the difference between the images: indeed, considering the positions in the moving image $IM(\boldsymbol{x})$ and in the reference one $IF(\boldsymbol{x})$, a coordinate transformation $T(\boldsymbol{x})$ is determined, in order to spatially align $IM(T(\boldsymbol{x}))$ with $IF(\boldsymbol{x})$ and consequently mapping $IM(\boldsymbol{x})$ to $IF(\boldsymbol{x})$.
Metric is crucial for an accurate image registration: by means of a similarity value that is computed between the input images (in this case from the pixel intensities), a pipeline is repeated until a convergence criteria is met. The idea is to derive the similarity value at each step, identifying the direction of alignment and going to the next step until the best match is detected and

the minimization problem is solved. In this work a reference configuration that is chosen is the end-systolic one, where the minimum ventricular volume is reached, in order to avoid the formation of non-conforming elements in the registration process. The corresponding displacement arrays are computed for the the homologous end-systolic endocardium, extracted from the myocardium.
In order to apply the metric, some pixels in the input images have to be selected. The component that is responsible for this mansion in SimpleElastix is the sampler. The sampler generates a grid on the reference frame and it chooses a random number of volumetric pixels with the relative greyscale intensity values. For what concerns the off-grid grey level values to be computed, an interpolation method is applied: in this work a non-rigid registration algorithm is considered, the B-splines registration algorithm, relying on an interpolator that is based on b-splines approximations of order N for the interpolation of the intensity values (where $N = 3$).
Considering K as the number of cine-MRI acquisitions, from the level-set images the algorithm provides as output the 3D displacements vector field $\boldsymbol{d}_{MRI}(t_k)$ (t_k=k*τ_{MRI}, with τ_{MRI} that represents the cine-MRI time resolution and k=$0, ..., K-1$) that is applied to the endocardium for each instant of time. In this way to ventricular motion is reconstructed and the transform from the fixed end-systolic configuration to the other ones is determined.
In Figure 3.10 there is an illustration of the endocardium that is deformed with each systolic displacement that has been determined with the image registration.

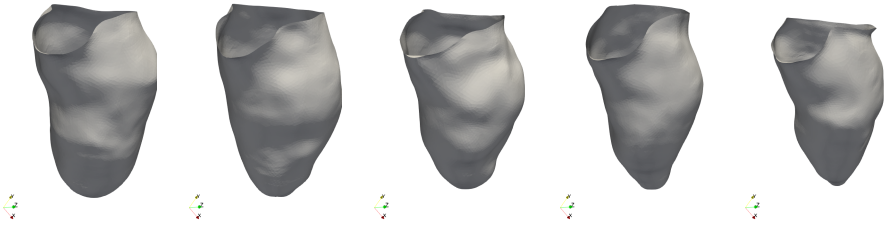

Figure 3.10: Reconstructed endocardium deformed with the systolic registered displacements (visualized with ParaView) [www.paraview.org]

3.3 Domain extension including the aorta tract and valve dynamics modeling

As described in the previous section, a patient-specific endocardium is modelled from the enriched artificial clinical images and the ventricular motion is reconstructed for each acquisition time of the cine-MRI. In order to build the computational domain and to solve a CFD problem, the aim is now to include the aortic tract and a mitral valve to the endocardial surface. In this way it is possible to model the hemodynamics and obtain a physiological characterization of the blood flow.
Whilst the myocardium and its motion could be captured accurately from the merged clinical images, exploiting the advantages of the volumetric short-axis acquisitions and the long-axis ones, for both the aorta and the mitral valve the cine-MRI series do not contain enough information for a segmentation and a reconstruction. The reasons differ for the two cases.
For what concerns the aortic tract, the standard image data routinely acquired in current clinical practice focus more on catching the heart functioning than the behaviour of the aorta. The only relevant aspect is brought by the 3 chambers view in the long-axis series, since it contains an overview of the initial aortic tract. Instead, from the short-axis view, the little information about the structure of the initial aortic tract is exploited for comparing the positioning and the dimensions of the aorta added to the computational domain with the ones relative to the clinical visualizations.
Regarding the mitral valve, the MRI acquisitions do not allow a direct segmentation of the leaflets due to their very thin structure and their very rapid motion during the contraction and relaxation phase (except when we deal with stenosis or thickening of the mitral valve). Even if the SLAM algorithm increased the resolution of the short-axis views and decreased the thickness of each slice, the resolution is still low and the movement of the leaflets is too fast with respect to the cine-MRI time step τ_{MRI}.
Since the aorta and the valve cannot be segmented, the computational domain is completed by deploying the template geometry *Zygote Solid 3D Heart Model* [53], a geometry that models a complete healthy heart that has been reconstructed from CT-scans (Figure 3.11). The connection of the two components to the left ventricle relies on adapting them to the endocardium aorto-mitral annulus.

Since the final goal is to perform a CFD simulation of a systole for each HCM patient that is taken into account, the aortic leaflets are neither geometrically nor mathematically modeled. Indeed the assumption is to consider the

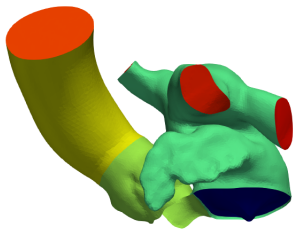

Figure 3.11: Zygote template geometry, modeling a healthy heart, from which the mitral valve, the left atrium and the aorta have been extracted [53]

aortic orifice always open during the test. Moreover, because of the aim of inspecting the consequences of HCM on ventricular walls and the systolic function, assessing the intraventricular obstruction, the aortic valve is negligible.
In order to perform the merge of the two components described above, the main strategy consists into using a command pipeline based on VMTK, hinging upon tools employed in [54].
In this work a new approach is proposed for the attachment of the template geometry to the end-diastolic LV endocardium (LV_{pz}, corresponding to the configuration at t=0), with respect to the procedure that has been applied in [2]. The reconstruction of the computational domain in [2] relies on the connection of the left ventricle with the whole Zygote template geometry, including the left atrium surface, and then removing the latter after having extended the displacement field $\boldsymbol{d}_{MRI}$ to the entire domain.
Instead, an improvement of the accuracy of the aortic representation can be achieved by excluding from the template geometry the left atrium and connecting directly the Zygote aorta (LH_{zyg}) to the endocardium. Further results are reported in Section 3.5.
In the following, the complete connection pipeline is described completely:

- **Pre-scaling all the Zygote inputs**: in the early stage of the process, the template aorta, its boundary ring and the mitral valve are geometrically rescaled (left image in Figure 3.12), for each dimension in the 3D space), in order to match the dimensions of the respective components manually measured from the cine-MRI visualizations or written in the clinical reports. The pre-scaling value, in this work, is computed as the ratio between the diameters of the aortic section corresponding to the Valsalva sinuses region of the patient-specific aorta

and the template one.

- **Registration of the aortic rings**: afterwards a rigid registration of the template aortic ring to the LV aortic annulus is applied through the *Iterative Closest Point* (ICP) algorithm (reported in [55]). The VMTK command is **vmtkicpregistration** and computes the distance between the rings.

- **Translation of the template aorta and valve**: in the next stage the Zygote aortic tract and the mitral valve undergo a geometrical transform and they are translated applying the command **vmtksurfacetransform**. The input matrix that contains the information needed to transform the surfaces is provided by the distance computed in the previous phase.

- **Harmonic connection**: the aorta is merged into the endocardium, representing the reference surface, by harmonically deforming the input aortic surface to the LV. A vectorial distance between the template and the reconstructed aortic annuli is computed (for this reason it is crucial having two open input surfaces). This distance represents the Dirichlet BC of a Laplace-Beltrami problem [56], whose solution is the deformation to apply to the stripe of LH_{zyg} near the LV boundary ring. After that the merge of the two surfaces becomes conform and the connection through harmonic deformation of the Zygote geometry is performed. The analogous process is repeated for the template mitral valve Γ_{zyg} that undergoes a harmonic deformation to be conform with the mitral annulus of the left ventricle at the end-diastolic phase, obtaining Γ (middle image in Figure 3.12).

- **Harmonic extension**: for what concerns the mitral valve surface a zero-displacement field is assigned through ParaView [www.paraview.org], in order to identify the physiological absence of motion in the valve with respect to the ventricular reference system. Whilst, the aorta undergoes a harmonic extension of the displacement field $\boldsymbol{d}_{MRI}$ through the command **vmtkharmonicextension**, that takes effect on a subset of the input surface, selecting the regions beyond the ventricular surface using the entity tags (avoiding the mitral valve entity ID, since a zero-displacement field must be assigned for this portion). The values of the displacement array is applied as Dirichlet BC for the harmonic extension at the boundary rings of the excluded domain. The solution is the displacement field $\boldsymbol{d}_{MRI}$ extended to the aortic tract (right image in Figure 3.12).

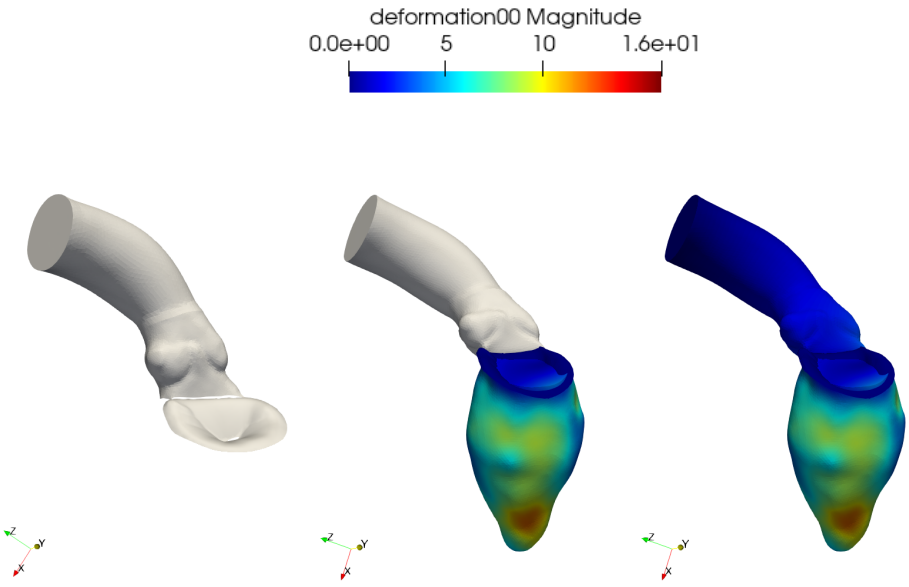

Figure 3.12: Schematic illustration of the domain extension with the Zygote template geometries [53]. Left: rescaled Zygote template geometries of the aortic tract and the mitral valve; Middle: the mitral valve deformed in a conform way with respect to the LV mitral annulus and the reconstructed endocardium colored with the displacement dALE00 (at t=0) harmonically connected with the deformed aorta; Right: harmonic extension of the displacement d_{MRI} (in the illustrated case dALE00) to the aortic tract, while for the mitral valve a zero-displacement field is assigned.
Generated thanks to the VMTK library [www.vmtk.org], using additional tools proposed by Fedele [54] and visualized with ParaView [www.paraview.org].

3.4 Volumetric mesh generation

In the last phase of the reconstruction pipeline the focus is on the generation of a computational volumetric mesh from the surface obtained in the previous step. Moreover, a specific geometry is created in order to store the displacement fields evaluated over the surface for each time instant and obtaining boundary conditions for the CFD simulation in the moving domain. Instead, the mitral valve is modeled as an immersed surface in the computational domain that stands still during the heartbeat. Thereby it does not contribute in the process of mesh generation and boundary conditions definition.
The aim is to obtain a hexahedral non-uniform mesh, with low characteristic length in the region of interest, where the jet is more intense, the LVOT,

whilst in the apical ventricular portion and in the ascending aorta a higher characteristic length can be considered, to reduce the total computational costs for the CFD simulations. The starting point is the output of the Section 3.3, the reconstructed geometry surface, characterized by a uniform triangulation with *triangles* as surface mesh elements (Figure 3.13, *left*).
As for the antecedent procedure, in order to achieve the purposes of this section, the Vascular Model Toolkit Library [www.vmtk.org] is adopted, along with the tools reported by Fedele in [54].
The meshing strategy consists in the following main steps:

- *Non-uniform remeshing*: a VMTK command, (**vmtksurfaceimplicitdistance**), consisting in generating an array that stores the computed distance from an input reference surface (a small sphere located in the middle of the *fibrous trigone*[1], as in Figure 3.13, *right*), is applied in order to define the two portions of the domain with different average characteristic length h. The command **vmtksurfacetagger** is deployed imposing a distance threshold and the two regions are generated. Afterwards **vmtksurfaceedgelengtharray** assigns an array containing the threshold value of $h = 2mm$ for the mesh elements of the LVOT portion, $h = 3.6mm$ for the elements outside, while, in the neighbourhood of the intersecting edges of the two macro-regions defined before, the characteristic length varies smoothly from 2 to 3.6. The choice of the mesh spacing is based on the work of Fumagalli et al. [2].
  Finally the command **vmtksurfaceremeshing** operates the remesh of the surface with the average characteristic length contained in the array generated in the previous phase 3.14.
  For each one of these steps the output file extension is the *.vtp*.

- Subsequently a suitable volumetric mesh for CFD is generated through **vmtkmeshgenerator**, where each volume mesh element is a *tethraedron*. In this case the output file is in the *.vtu* format, suitable for a volumetric geometry with unstructured grid.

- From the tetrahedral volumetric mesh, **vmtkmeshtethex** provides a hexahedral one, by splitting each tetrahedron (volume mesh element) in four hexahedra and each triangle (surface mesh element) in three quads (Figure 3.14). The latter have approximately half of the characteristic length with respect to the correspondent starting triangles.

[1] The structure that ensures fibrous continuity between the aortic and the mitral orifices, that has been introduced in Section 1.2.1

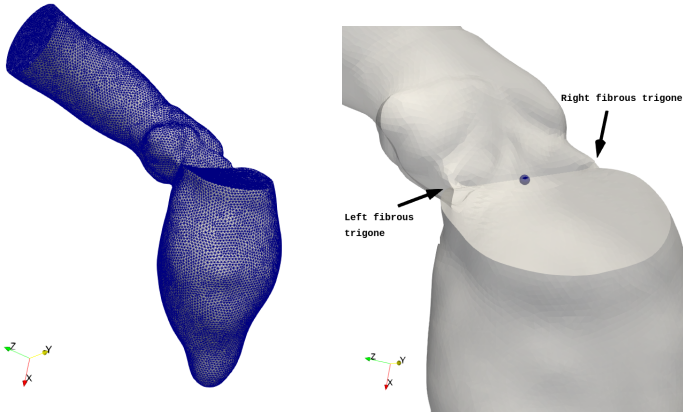

Figure 3.13: Left: Uniform triangulation of the surface of the computational domain before the mesh generation step; Right: example of reference sphere located in the middle of the fibrous trigone, in order to compute the distance from it, which defines the two portion of different mesh characteristic length by means of a threshold distance. Generated thanks to the VMTK library [www.vmtk.org], using additional tools proposed by Fedele [54] and visualized with ParaView [www.paraview.org]. [www.paraview.org]

As a consequence, in the LVOT region $h \simeq 1mm$, while elsewhere $h \simeq 1.8mm$. The output file extension is still *.vtu*.

- The last step consists into exportating the mesh file and writing it into the disk in the format *.msh*, having as input the generated hexahedral volumetric mesh. The deployed command is **vmtkmeshwriter**.

3.5 Results from the application of the complete pipeline

In this section the outputs of the application of the reconstruction pipeline described in the previous sections are shown for two patients, whose cine-MRI acquisitions and clinical reports were provided by L. Sacco Hospital of Milan. Both patients suffered from non-obstructive HCM, without SAM of the mitral valve.
The most significant global cardiac performance indicators, explained in Section 1.2.3, are inspected for the analyzed patients. Moreover, due to the potential clinical relevance, the results obtained evaluating those parameters are compared with the corresponding ones, already computed, of a third patient, provided by L. Sacco Hospital, suffering from SAM of the mitral valve associated to Hypertrophic Obstructive Cardioyopathy (HOCM).

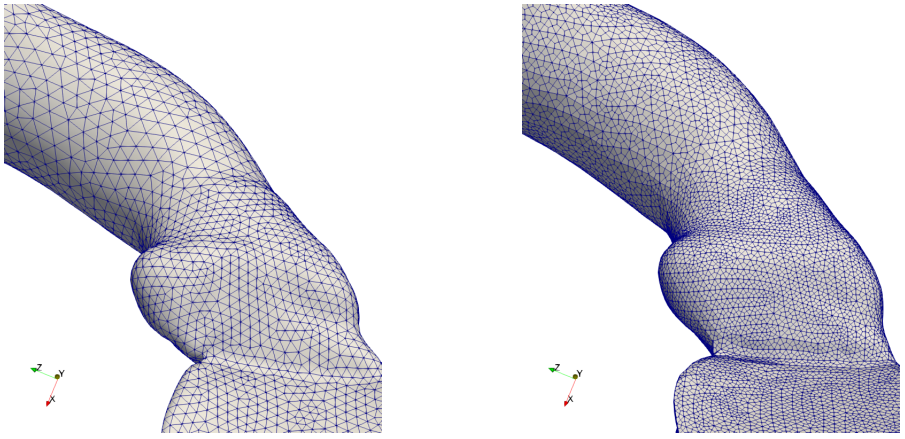

Figure 3.14: Left: Non-uniform triangulation of the surface mesh, with low characteristic length in the LVOT region and a higher value outside Right: hexahedral volumetric mesh with each surface triangle splitted into three quads and each tetrahedron into four hexahedra.
Generated thanks to the VMTK library [www.vmtk.org], using additional tools proposed by Fedele [54] and visualized with ParaView [www.paraview.org].

This idea derives from a relevant consequence of the presence of SAM The clinical conditions of the two HCM patients and the SAM-HOCM one are delineated thanks to the reports provided by L. Sacco Hospital, with the approval of the Ethics Committee and in accordance to the ethics guideline of the institutions involved, including the signed consent of the patient:

- **Patient 1**: 57 years-old woman, with pronounced symmetric HCM, without SAM, and reduced cavity dimensions ($EDV = 128\,mL$). The wall mass, thickness and systolic thickening are relevantly increased (in particular an end-diastolic wall mass of $240\,g$ is reported). The global systolic function is reduced, with a computed ejection fraction $EF = 37\,\%$. Also, a septal hypokinesis in the medium-basal region is observed, so a slow or reduced motion of the interventricular septum, causing anormal contractions during the heartbeat. Moreover an infiltrative pathology of type *amyloidosis* is reported, that consists in the abnormal accumulation of the *amiloid* protein in the myocardium.
- **Patient 2**: 66 years old man, with non-obstructive hypertrophic cardiomyopathy without SAM. Increased wall and septal thickening ($EDV = 153\,mL$) and high wall mass (measured end-diastolic wall mass of $216\,g$). Remarkable decrease of the global systolic function ($EF =$

32 %). Also, distributed septal hypokinesis in the septal and medium-basal areas is observed. No mitral regurgitation has been detected.
For what concerns the aortic tract, a very mild aortic insufficiency is observed and a slightly inflated value of the aortic root diameter ($36\,mm$) has been measured (with the ascending tract with the same diameter value).

- **Patient 3** (not examined in this work, taken into account for comparison results): 83 years-old woman with symmetric HCM, with preserved global systolic function (63 %), LV dimensions within the limits of physiological values ($EDV = 101\,mL$) and increased wall mass (end-diastolic wall mass equal to $59.9\,g$), thickness and thickening.
Most of all, from the cine-MRI series, it has been observed the prolapse of the anterior leaflet of the mitral valve towards the septum, causing a stenosis and an obstruction in the LVOT.

3.5.1 Outputs of the reconstruction pipeline

The strategy discussed above in the chapter is applied to Patient 1 and Patient 2, in order to define the computational domains for each CFD simulation, determining the corresponding geometry and the local displacements that deform the domain from the reference end-systolic configuration to the other time instants of the heartbeat. The implemented pipeline is summarized in the following algorithm:

- application of the SLAM Algorithm to the cine-MRI short-axis and long-axis series (Figure 3.19);
- segmentation of the endocardial and the epicardial surface from the enriched images and generation of a merged myocardial surface from a VMTK-based pipeline (first row of Figure 3.15) that intersects the two input surfaces;
- generation of the 3D level-set images of the reconstructed myocardium (second row of Figure 3.15);
- registration of the local displacement field $\boldsymbol{d}_{MRI}$ from the level-set images exploiting the SimpleITK tool [www.simpleitk.org] (Figure 3.16). Comparing the two patients endocardia for each time instant, it is possible to detect the different shape of the left ventricles: Patient 1 has a more elongated endocardium, while Patient 2 cavity has larger dimensions that can be caught straightaway from the picture;

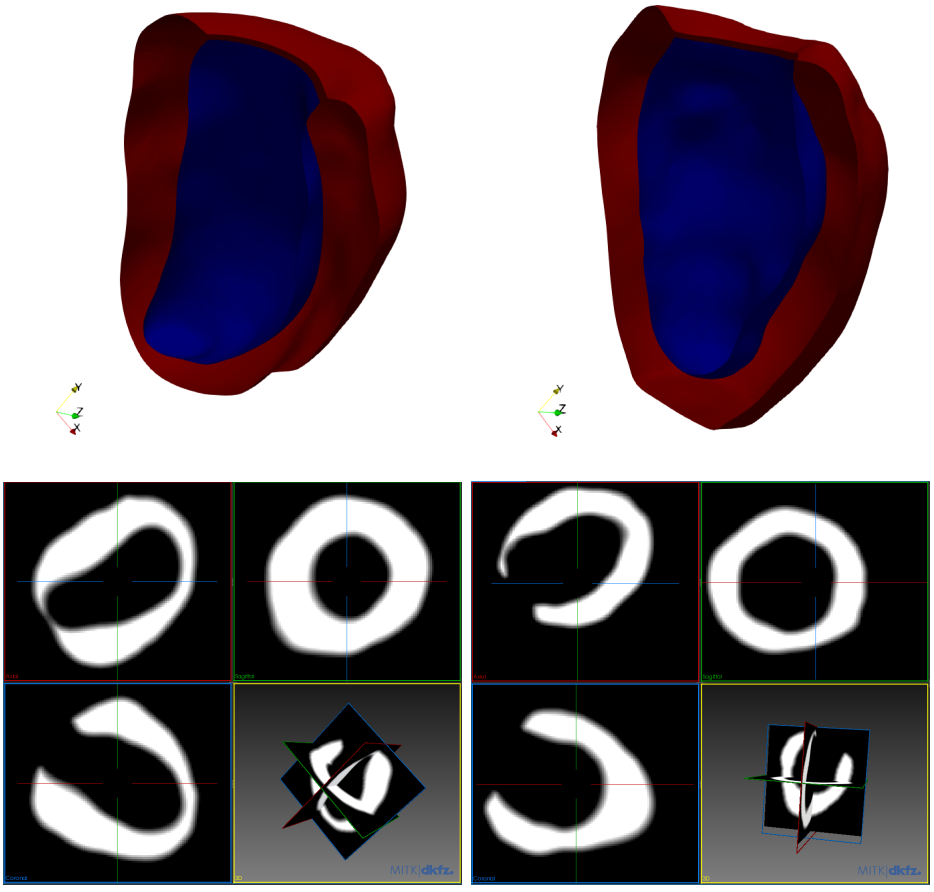

PATIENT 1 PATIENT 2

Figure 3.15: Patient 1 and Patient 2's cross sections of the reconstructed 3D myocardial surfaces (highlighting in red the epicardium and in blue the endocardium) and level-set images at t=0.2 s.
3D surfaces visualized with ParaView [www.paraview.org], level-set images analyzed with MITK [www.mitk.org]

- harmonic connection of the Zygote aortic tract and mitral valve to the left ventricle and harmonic extension of the displacement fields to the whole computational domain (Figure 3.18). From both the representations of the corresponding geometry, it is possible to observe the reconstruction of the physiological mitral valve modeled as an immersed surface in domain and located confirmly with respect to the ventricular base. Moreover in Figure 3.18 the zero-displacement field is highlighted on the surface of the mitral valve, ensuring its stillness

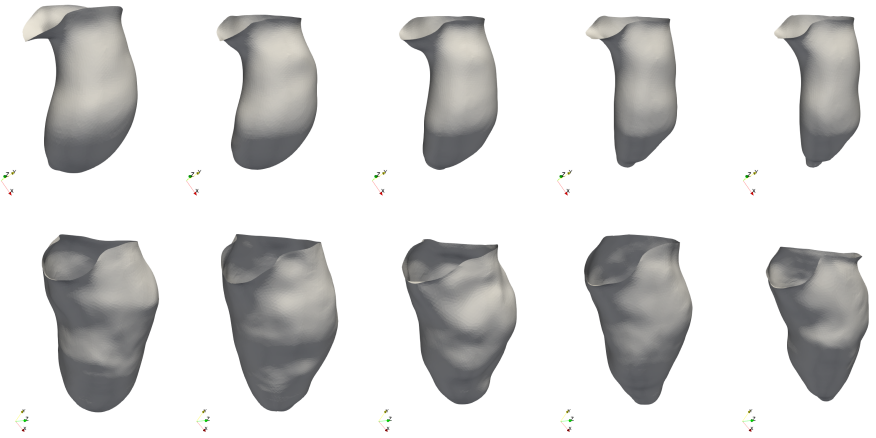

Figure 3.16: Reconstructed endocardia deformed with the systolic registered displacements, from t=0 s to t=0.4 s with time step 0.1 s. Upper side: Patient 1; Lower side: Patient 2 (visualized with ParaView) [www.paraview.org]

during the heartbeat. For what concerns the dimension of the LV cavity and aortic root, a remarkable enlargement can be noticed for Patient 2, in addition to the distributed hypokinesis that can be detected in the lateral wall of the medium-basal region, near the septum, for the time instant t=0 s.

- 3D hexahedral mesh generation and displacement fields storing, applying a VMTK pipeline, obtaining a computational volumetric mesh from the 3D domain surfaces. The spatial discretization in the domain is the same for the two patients, applying an average characteristic length of h=1.8 mm, with a local refinement to h=1 mm in the region of the mitral valve, including the LVOT.

3.5.2 Short-Long Axis Merging algorithm

The process of merging the cine-MRI volumetric short-axis acquisitions with the long-axis images through the SLAM algorithm has brought crucial improvements in the image processing phase. As it can be noticed from Figure 3.19, the contours of both the endocardia in the computed frame are more accurate and well defined with respect to the correspondent original short-axis visualization. The resolution in the merged images increases for each instant of time and for each frame of the cine-MRI short-axis series. As a consequence, the segmentation phase is more user-friendly and leads to a

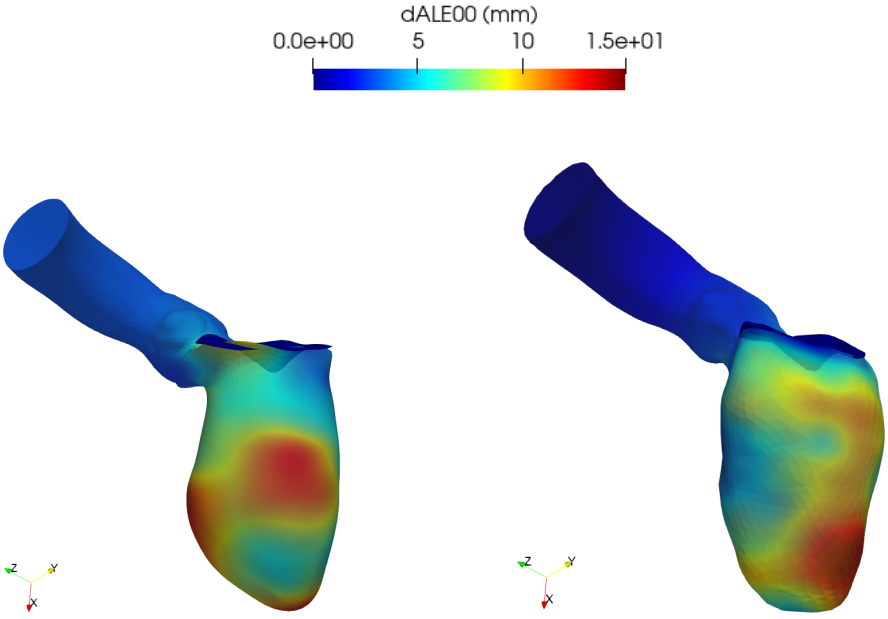

Figure 3.17: The 3D domain surfaces at t=0 s with the local displacement field dALE00 projected Left: Patient 1; Right: Patient 2
Generated thanks to the VMTK library [www.vmtk.org], using additional tools proposed by Fedele [54] and visualized with ParaView [www.paraview.org].

more precise reconstruction, since the 3D interpolation method hinges upon the pixel grey-scale intensity.
A particular that can be observed in both the artificial frames is the brighter lines, representing the original slices in the short-axis acquisition: the reason behind that is the approach of computing a weighted average of the grey intensity values of the projections onto the nearby slices with respect to the one that is considered. So, since the contrast between short-axis and long-axis views can be different, this leads to obtaining darker slices, that are inserted between two brighter original ones.
Another relevant advantage that is exploited using the SLAM algorithm, as already claimed, is the possibility to capture the motion of the ventricular base due to the endocardium shortening throughout the systole, that keeps the ejection fraction stable within physiological values.
The original short-axis acquisitions and their high spacing value between the slices do not allow to catch the base, since it could move between two slices. The SLAM algorithm, instead, allows a segmentation of the basal region

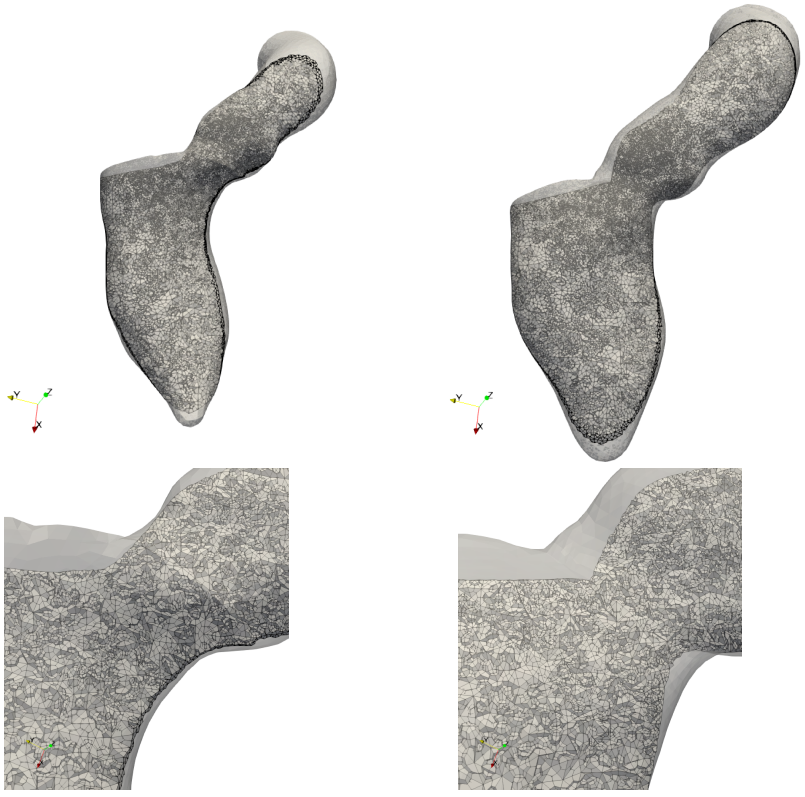

PATIENT 1 PATIENT 2

Figure 3.18: The 3D hexahedral meshes at t=0.3 s of Patient 1 and Patient 2, emphasizing the mesh refinement in the region of the mitral valve in the lower pictures Left: Patient 1; Right: Patient 2
Generated thanks to the VMTK library [www.vmtk.org], using additional tools proposed by Fedele [54] and visualized with ParaView [www.paraview.org].

from the resulting enriched images, adding the information deriving from the long-axis acquisitions. Figure 3.20 shows that the merging algorithm let the segmentation procedure represent for the respective patient the LV base and its movement within the systolic shortening (that stops in the instant where the minimal volume is reached).

3.5.3 Inclusion of the aorta

The next aspect to be discussed in this work is the improvement in the inclusion of the Zygote template geometry of the aorta. The original approach consisted in the harmonic connection between the reconstructed en-

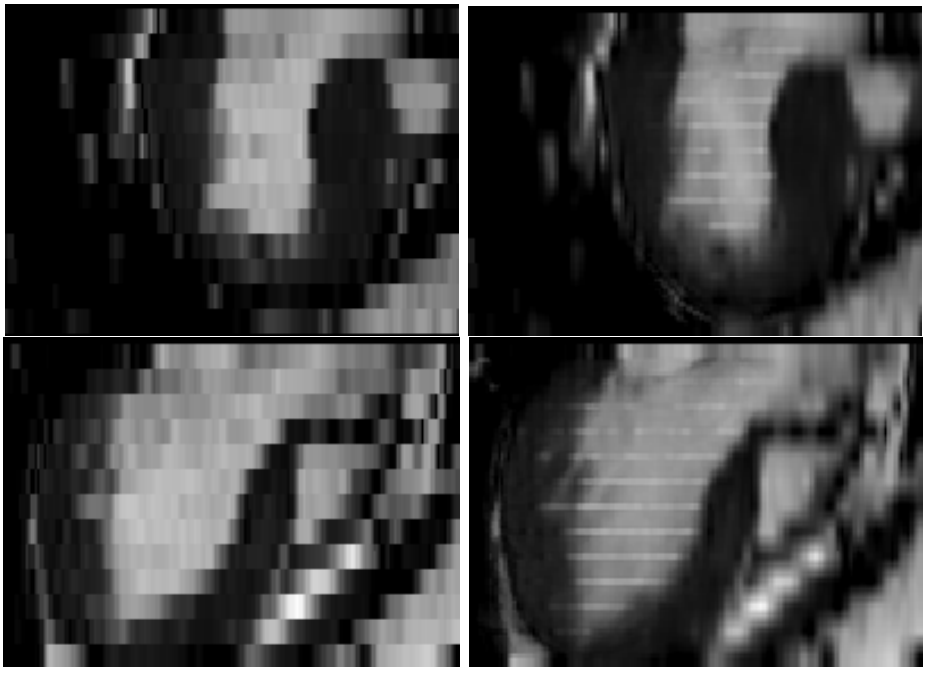

Figure 3.19: Comparison for each patient between the original short-axis view and the merged image resulted from the application of the SLAM algorithm, at the time t=0.2 s. Upper-Left: original image, patient 1; upper-right: computed image, patient 1; lower-Left: original image, patient 2; lower-right: computed image, patient 2 (clinical images provided by L. Sacco Hospital in Milan and visualized with MITK) [www.mitk.org]

docardium and the whole *rescaled* template geometry (reported in 3.11), including the left atrium surface, proceeding then with the harmonic extension of the displacement field $\boldsymbol{d}_{MRI}$ and finally removing the left atrium tract in ParaView [www.paraview.org], since for the purposes of the CFD simulations the atrium is not involved and is not included in the computational domain.

An important issue arises when a patient-specific aortic tract section has a diameter which differs relevantly from the respective value of the template geometry. For instance, as in the case of Patient 2, the aortic root diameter value, measured in the clinical reports, is $36\,mm$, slightly higher than corresponding measure in the reconstructed endocardium (29.5)). This matter leads to computing a higher value of *pre-scaling* in the VMTK pipeline for the connection of the two components. As a consequence, having included the left atrium in the merging phase, also the latter is rescaled. The result is a possible degeneration of the template geometry aortic annulus, that is deformed to let it be conform to the LVOT border. This means that the

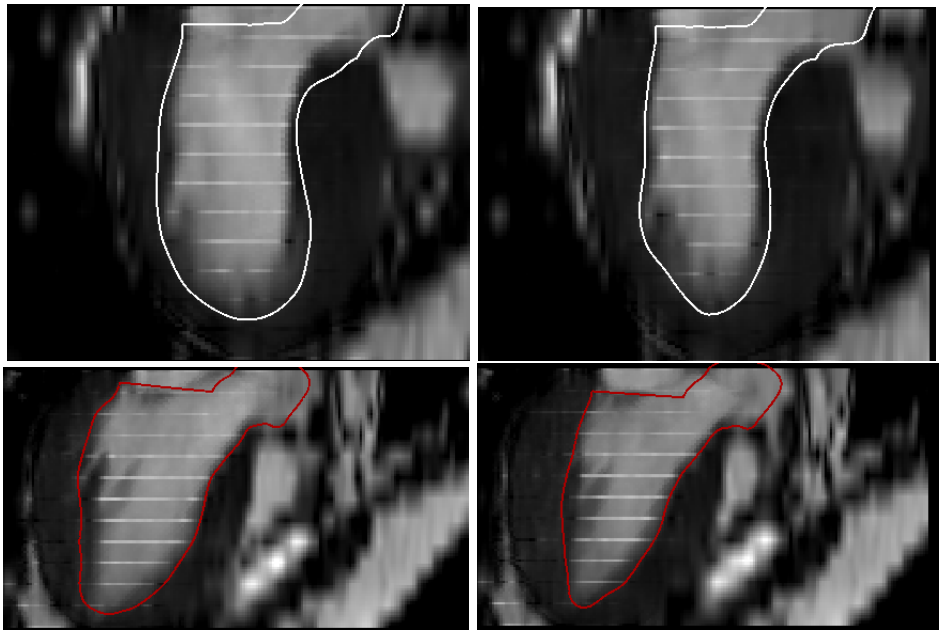

Figure 3.20: Thanks to the SLAM algorithm, the ventricular base is captured from the segmentation of the enriched image of Patient 1 (first row) and Patient 2 (second row). Left: mid-systolic endocardium, at t=0.2 s; Right: end-systolic endocardium, at t=0.4 s (clinical images provided by L. Sacco Hospital in Milan and visualized with MITK) [www.mitk.org]

fibrous trigone is not accurately represented and the basal region is not well captured.

The other main issue of connecting to the left ventricle the whole Zygote geometry is related to the angle delimited by the aortic and atrial edges with respect to the base-to-apex plane, in correspondence of the mitral and aortic valves area. Indeed, this parameter varies from case to case and it can change due to different factors, as for example the position and the breath of the patient during the magnetic resonance. Whilst, the Zygote geometry is obtained for a physiological case, without pathologies.

As already claimed, standard image data routinely acquired does not focus into fully catching the aortic tract and its structure. Instead, from the 3-chambers view in the MRI long-axis series significant information can be extracted and exploited. Indeed, projecting the Zygote geometry into a frame of this type of acquisition, it is possible to compare the angles formed by the left atrium and the aorta for the original patient-specific clinical image and the template component to be included. Applying this validation process, it is possible to verify whether the described parameter is far from

the reference Zygote value for the considered patient, leading to inaccuracy problems in the inclusion of the aortic tract due to different slopes between the captured aorta from the clinical images and the computational domain one.
These issues have been experienced, in particular, with the analysis of Patient 2. Figure 3.21 illustrate the mismatching angles values manually measured with a tool of MITK: the Zygote structure carries the constraint of a fixed inclination between the left atrium and the aortic tract, modeling the physiological representation of the two aforementioned regions. This represents a limitation in the reconstruction pipeline, since, the evaluated angle directly from the 3-chambers long-axis view is almost the double. Whilst, a pre-scaling value higher than 1 entails an enlargement of the left atrium portion.

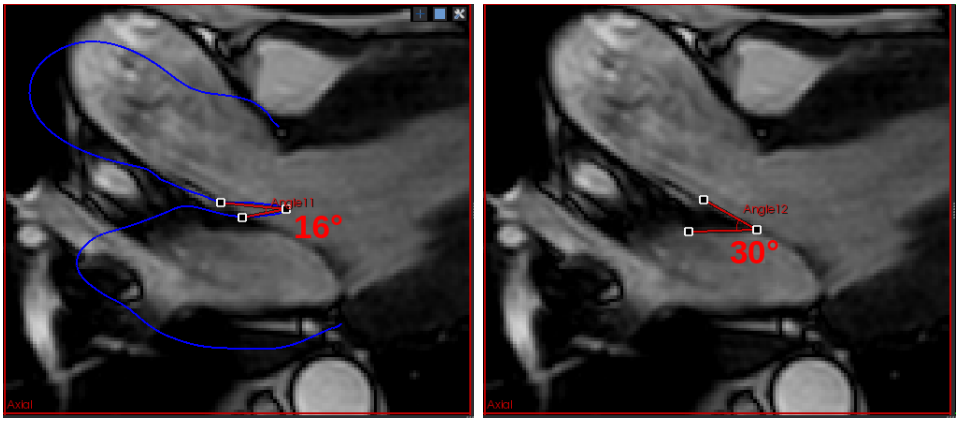

Figure 3.21: The different left atrium-aorta angles (with respect to the base-to-apex direction) between the Zygote geometry (Left, $16°$*) and Patient 2 clinical images (Right,* $30°$*).*
3-chambers long-axis image, provided by L. Sacco Hospital in Milan and visualized with MITK [www.mitk.org]

The two problems combine and cause high imprecision for the definition of the computational domain after connecting the template aorta to the left ventricle, as the red tracts in Figure 3.22 show for a fixed time instant and frame. A consequence of the inaccuracy of the aortic representation is a different behaviour of the blood flow, with the jet impacting differently on the aortic walls and the spatial location of the obstruction that is shifted.
An improvement that has been found in this work consists into modifying the original domain extension pipeline, obtaining the one described in Section 3.3. The first step is to remove straightaway the left atrium region from

the Zygote 3D model, instead of neglecting it after the harmonic connection and extension. Then, in the rigid registration phase, rather than applying a geometric translation of the template geometry based on the distance between the reconstructed and template valvular ring (including both the aortic and mitral annuli), the ICP method is exploited with the only aortic annulus. For what concerns the Zygote model, the aortic ring is trivial to select from ParaView, whilst for the reconstructed endocardium it is necessary firstly to capture the fibrous trigone with the auxilium of the clinical images. Afterwards, the pipeline proceeds in the same way for both the original and the new approach for the domain extension. The final result of a direct connection of the aortic tract with the left ventricle is highlighted in blue in Figure 3.22: a comparison between the computational domain obtained with the original and the new approach is carried on, showing a big improvement in terms of precision of the representation and aortic tract capturing.
Thereby, the image processing pipeline that has been applied relies on the new domain extension approach.

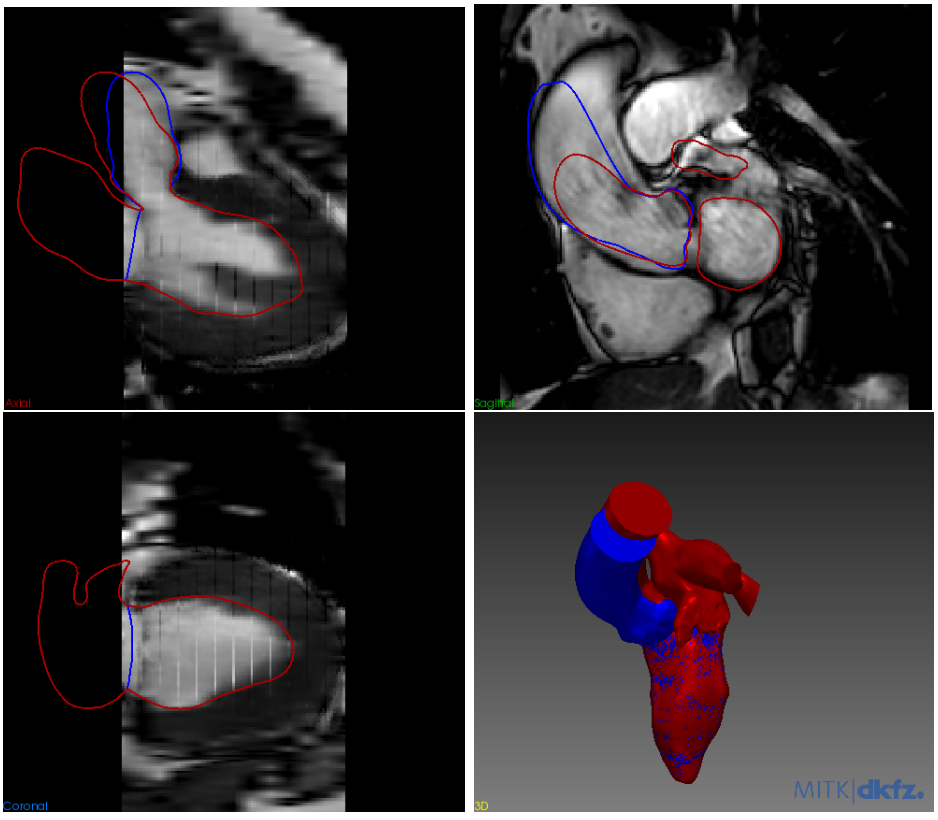

Figure 3.22: The comparison at t=0.3 s between the computational domains obtained from the original reconstruction pipeline (with the inclusion of the whole Zygote geometry to the domain straightaway) and the new one (removing the left atrium and connecting the aorta directly to the left ventricle). The 3D surfaces are plotted on the short-axis enriched images and the respective aortic tracts are paired in terms of shape and inclination with the aorta captured in the clinical acquisitions.
Upper-Left: MITK view in the base-to-apex direction; Upper-Right and Lower-Left: MITK visualizations orthogonal to the base-to-apex direction; Lower-Right: MITK 3D representation of the computational surfaces.
MRI Short-axis series provided by L. Sacco Hospital in Milan and visualized with MITK [www.mitk.org]

3.5.4 Outputs of interest from the imaging results

After discussing the improvements and the advantages of the SLAM algorithm and the new domain extension approach, the focus now is on presenting relevant outcomes regarding the global cardiac functioning of each patient. In this section also Patient 3 relative results are going to be shown and compared with to the other patients corresponding outputs.

Firstly the focus is on the geometric indicators of the reconstruction pipeline. The displacement field $\boldsymbol{d}_{MRI}$ is depicted in Figure 3.23 for the three patients. It is possible to observe strightaway the different distribution and intensity of the deformation fields, highlighting the anomalies in the contraction phase caused by HCM, that have been assessed in clinical reports. For instance, if can be claimed that each patient is characterized by a reduced motion in the septal region, it is also true that the hypokinesis is present in other endocardial portions, depending on the case: Patient 1 movement is decreased near of the ventricular base, while Patient 2 distributed hypokinesis is evident, with a substantial motion reduction in the posterolateral wall of the medium-basal region. Patient 3, then, reaches the peak of deformation in the lateral wall of the endocardial base, causing the shortening of the basal area that contributes to keep the ejection fraction within the physiological limits. The non-homogeneous distribution of the displacements affects the

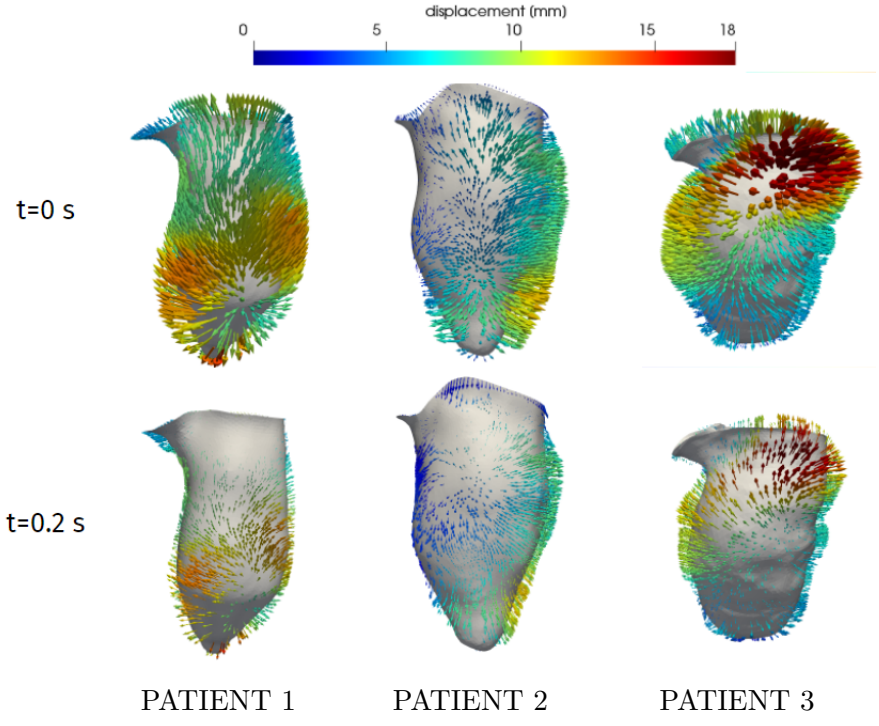

Figure 3.23: Reconstructed displacement fields for the three patients at the end of diastole (t=0 s) and in late systole (t=0.2 s). The spatial configuration is the same for each case, with the endocardium aligned vertically and the interventricular wall septum located on the left.
Visualized with ParaView [www.paraview.org]

evolution of the LV cavity volume. As outlined in Figure 3.24, the behaviour is coherent with respect to the physiological pattern reported in the Wiggers diagram, validating the reconstruction procedure in terms of modeling of the ventricular geometry and motion during the heartbeat. As expected, after the end of the systole at t=0.4 s, the expansion rate of the LV differs from case to case. Patient 2, for example, undergoes a slowed diastolic expansion with respect to the physiological evolution of the volume reported in the Wiggers diagram in Figure 3.24. This aspect is coherent with the value of EF, the lowest among the ones reported from the clinical estimates with respect to the three patients and mentioned in Table 3.1. In particular this denotes that Patient 2 expels an insufficient amount of blood by comparison with the high estimate of the End-Diastolic Volume. The stroke volume is too scarce to ensure an efficient blood flow. A low value of ejection fraction is also in accordance with the distributed hypokinesis of Patient 2 in the basal region, since the reduced motion interfers with the shortening movement of the base, that is crucial in the contraction phase to support the blood flow from the LV cavity.

Analyzing the same Table 3.1, a comparison is performed between the volume measurements estimated after the reconstruction pipeline with those obtained from clinical data acquisition. Clinical volume estimates hinge upon a significant measure criterion: the approximation of the left ventricle as an ellipsoid [93]. For what concerns the EDV evaluation, the two approaches show good agreement, as for each patient the difference between the reconstructed value and the one obtained from clinical measures differs by less than the 8%. The End-Systolic Volume, instead, brings important differences between the two methods. An explanation can be related to the HCM effects on the LV contraction, that may entail spatial inhomogeneity for the endocardium, causing possible inaccuracies in the approximation of the ventricle as an ellipsoid. As a consequence, there are discrepancies in the ejection fractions measures. Regarding Patient 3, although SAM associated to HOCM affects the relative blood flow, physiological values of EF are obtained with both the approaches, confirming that the global systolic function is preserved. This is in accordance with the illustration of the displacement field at the end of diastole in Figure 3.23, since the intensity of the deformation is high in the basal region, allowing the indispensable shortening of the ventricular base, that keeps EF within the physiological limits.

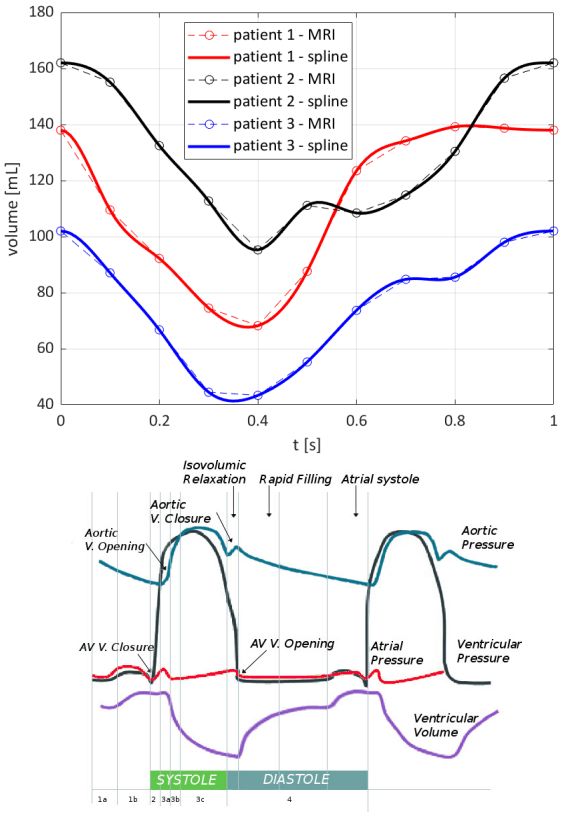

Figure 3.24: Time evolution of the volume of the reconstructed LV cavity, compared with the reference physiological behaviour reported in Wiggers diagram [24]

Patient	EDV[mL]	ESV[mL]	EF[%]
1	138	68	51
2	162	94	42
3	102	43	57
1	128	81	37
2	152	103	32
3	101	37	63

Table 3.1: Comparison between the evaluations of the End-Diastolic Volume(EDV), End-Systolic Volume and Ejection Fraction from the reconstruction pipeline (above) and the clinical estimates (below)

Chapter 4

Mathematical modeling of the physical problem and numerical analysis

After segmenting the patient-specific left ventricle from the enriched artificial cine-MRI acquisitions, recovering the local endocardial displacement, extending the domain with the Zygote template aortic tract and mitral valve and generating the volumetric mesh, the aim of this work now is to discuss the mathematical framework of the physical problem, presenting the fluid-dynamics equations that rule the hemodynamics in the moving computational domain in the systolic phase of the heartbeat. Moreover, a numerical analysis is going to be performed, presenting the relative challenges and the applied methods to derive the solution of the final linearized system.

4.1 Introducing the CFD model in a moving domain with valve dynamics modeling

4.1.1 Initial assumptions on the physical problem

The computational domain Ω^t=$\Omega(t)$ is displayed in Figure 4.1 ($Left$). Its surface is subdivided into three portions:

- Σ^t_{wall}=$\Sigma_{wall}(t)$, representing the ventricular endocardium wall and the aortic tract surface;
- Σ^t_{out}=$\Sigma_{out}(t)$, identifying the distal section of the ascending aorta, where an outflow condition will be assigned;

- Σ_m^t=$\Sigma_m(t)$, showing the upper edge of the left ventricle, the region where the closed mitral valve will be immersed.

.

Since the heartbeat period of interest is the systole and Σ_m^t follows the motion of Σ_{wall}^t, prescribed through the reconstructed cine-MRI displacement data, we introduce the surface $\Sigma^t = \Sigma_{wall}^t \cup \Sigma_m^t$, where a unique boundary condition will be assigned in the strong formulation of the mathematical model.

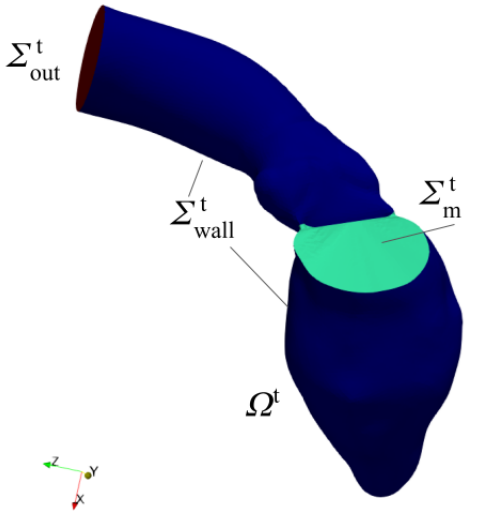

Figure 4.1: Computational domain Ω^t, with the subdivision of its boundary into the surface representing the ventricular and aortic wall Σ_{wall}^t, the distal section of the ascending aorta Σ_{out}^t and the upper edge of the left ventricle Σ_m^t (visualized with ParaView) [www.paraview.org]

For what concerns the blood flow, the first common convention is to consider it as a **homogeneous incompressible** fluid, with constant density $\rho = 1.06 \cdot 10^3\, kg/m^3$ and dynamic viscosity $\mu = 3.5 \cdot 10^{-3}\, Pa/s$ [24]. Secondly, it is crucial to specify the assumptions made to model the rheological characteristics of the blood, deriving the constitutive relations under which the mathematical model can be presented. In particular, blood can be considered either as a **Newtonian** fluid or as a non-Newtonian one, namely if the Newton's law of viscosity holds or not, depending on the setting of the problem and the process to be modeled. Newton's law of viscosity claims the

linearity of the viscous stress with respect to the strain rate, which means that, in mathematical terms, in case of an isotropic material, that the following equation holds:

$$\tau = \mu \frac{du}{dy} \tag{4.1}$$

where τ identifies the shear stress, $\frac{du}{dy}$ is the derivative of the velocity with respect to the direction of shear and μ is the dynamic viscosity. In terms of the Cauchy stress tensor σ, since in this case the fluid is also incompressible, the following relation that introduces also the pressure term is true:

$$\sigma(\mathbf{u}, p) = -p\mathbf{I} + \mu(\nabla \mathbf{u} + \nabla \mathbf{u}^T) \tag{4.2}$$

Since blood is a fluid connective tissue, composed by particles suspended in a solution called *plasma*, which are transported in specific regions of the body. For the latter, it is reasonable to consider it as a **Newtonian fluid**, but, due to the action of the particles, that can form non-negligible aggregates, the blood can be modeled as a non-Newtonian fluid, as in many models regarding the hemodynamics in a vessel lumen of small size. For this reason, in this work, because of the the computational domain larger scale, with respect to a vessel lumen, we consider the blood as a Newtonian fluid.

4.1.2 Mathematical challenges for the physical problem modeling

Before presenting the continuous Navier-Stokes equations and discussing both the corresponding strong and weak formulations, it is firstly necessary to discuss two modeling issues:

- The inclusion of the mitral valve in the problem as an immersed surface in the computational domain
- The prescription of the reconstructed ventricular displacements, extended to Σ^t, in a moving boundary problem

In the literature many methods and approaches have been proposed to model an immersed surface in the fluid domain, in order to assess the cardiac hemodynamics with the presence of valves.
For what concerns the mitral valve, many approaches have been exploited to model it as an immersed surface in the fluid domain. For instance cutFEM/XFEM [62-65] methods (discretizing the model on a fixed background mesh) have been introduced, as also Arbitrary Lagrangian Eulerian (ALE)

based ones [58-61] or chimera overset grid methods (hinging upon the decomposition of the complex geometry into simple overlapping grids) [66-67]. The main characteristic of these approaches is the mandatory requirement of updating the fluid computational mesh.
Instead, other methods as the immersed-boundary and fictitious-domain ones [8][68-80] allow to deal with a computational mesh independent of the immersed surface.
For what concerns instead the issue of defining a boundary problem to prescribe the local displacements reconstructed from the artificial cine-MRI images, the chosen strategy relies on the application of the ALE formulation to the Navier-Stokes Equations (NSE): the latter are reformulated on a frame of reference that moves with the fluid mesh [24]. This approach is not Lagrangian-based (there should be a frame moving with the fluid particles) nor Eulerian-based (since it is not a priori fixed in space). Furthermore this strategy allows to reconstruct the fluid domain only once, since with the ALE approach the mesh nodes move at each time step.
A remarkable advantage of this method is that it can be applied in a CFD problem and it can exploit the imaging results of the reconstruction pipeline, obtained from the standard image data routinely acquired by clinical tools. So it represents a valid alternative to the resolution of FSI problem, that requires to model the complex mechanics of left ventricle and mitral valve, decreasing in a significant way the computational efforts.
Regarding the inclusion of the mitral valve surface Γ_{mv} in the fluid mesh in the mathematical model and its effects to the blood flow, this work relies on a procedure falling withing the category of the immersed boundary and fictitious domain methods: the Resistive Immersed Implicit Surface (RIIS) method, exploited for the first time in the work of Fedele et al. [21], relying on the results presented by Fernández, Gerbeau and Martin [23] and Astorino et al.[22]. Moreover, having the goal of assessing the effects of SAM of the mitral valve, it has been applied also by Fumagalli et al.[2]. Due to RIIS method, only the immersed portion Γ of the mitral valve Γ_{mv} is involved in the mathematical model, with the external part, outside the computational domain, that is totally neglected (Figure 4.2).
The method consists into adding a penalization term depending on suitable positive constants R and ε in the momentum equation of the Navier-Stokes Equations. The first constant identifies a resistance coefficient, while the second is a sufficiently small value representing half-thickness of the narrow region around the mitral valve surface Γ, affected by the penalization term.

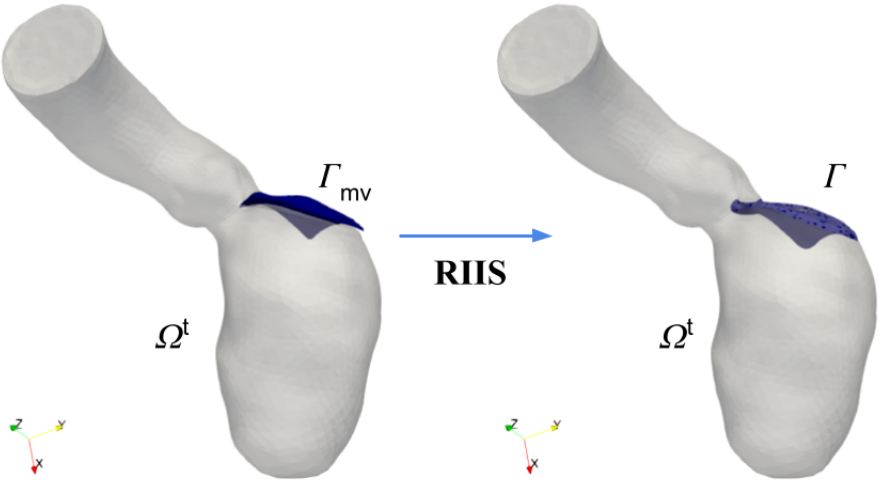

Figure 4.2: RIIS method involves only the immersed part Γ *of the closed mitral valve surface* Γ_{mv} *(visualized with ParaView) [www.paraview.org]*

4.2 Strong formulation

In this section, starting from the common Navier-Stokes strong formulation, with the adding of the RIIS term, the strong formulation of the NSE in a moving domain with the ALE approach is going to be derived by computing the *ALE derivative operator*, hinging upon the solution of the harmonic extension problem of the displacement datum at the ventricular wall $\boldsymbol{d}_{wall}$. The resulting CFD problem is obtained from the merge into a single framework of two different methods, that account for two distinguished modeling issues: the RIIS method for the fluid/structure interaction between blood and mitral valve surface; the ALE approach for the fluid/structure interaction between blood and ventricular myocardium.
For what concerns the fluid domain motion, relying on the displacement field $\hat{\mathbf{d}}_{MRI}$ referred on the end-diastolic configuration and reconstructed in Chapter 3, the ALE approach is employed. Indeed, it is a formulation very suited for ventricular and blood vessel models, since it does not need to handle large displacements, that would otherwise surely lead to high degeneration of the fluid mesh, due to the presence of severely stretched mesh elements. For this reason only frequent grid remeshing would solve the issue, increasing relevantly the computational effort. In terms of outputs of a numerical simulation, the consequence of the distortion of the mesh would

be an anomalous behaviour of the velocity and the pressure profiles, with non-physiological peaks, affecting the accuracy of the solution and the representation of the patient-specific cardiac hemodynamics.
In this work, the only significant issue to untangle about exploiting the ALE formulation is the fact that the displacement fields $\mathbf{d}_{MRI}$ need to be interpolated in a finer grid, since they are defined only in the time instants t_k, for $k = 0, ..., K$, so that they can be available for each time instant in the systolic phase $(0,T_S]$. A deeper discussion of the interpolation of the displacement datum is presented in Section 4.5.
Consequently, it is possible to exploit the ALE technique, introducing a fluid domain displacement in order to reformulate the Navier-Stokes Equations on the end-diastolic frame of reference, moving with the fluid mesh accordingly to the displacement datum.
The fluid domain displacement is the solution of a harmonic extension problem of the displacement datum at the domain wall, defined for each $t \in (0, T_S]$, where the laplacian problem is solved always on the input mesh:

$$\begin{cases} -\Delta\hat{\mathbf{d}}(\mathbf{x}, t) = \mathbf{0} & x \in \Omega^0, \\ \hat{\mathbf{d}}(\mathbf{x}, t) = \hat{\mathbf{d}}_{MRI}(\mathbf{x}, t) & x \in \Sigma^0, \\ \partial_n\hat{\mathbf{d}}(\mathbf{x}, t) = 0 & x \in \Sigma^0_{out}. \end{cases} \tag{4.3}$$

The fluid domain displacement allows to compute the domain velocity $\mathbf{u}_{ALE}$, that is the time derivative of ($\mathbf{x}$,t), i.e.:

$$\mathbf{u}_{ALE} = \left(\frac{\partial}{\partial t}\hat{\mathbf{d}}\right) \circ \hat{\mathbf{d}}^{-1}.$$

Subsequently it is possibile to evaluate the *ALE time derivative* of the velocity $\mathbf{u}$, that relies on the *Reynolds Transport Formula*:

$$\partial_t^{ALE}\mathbf{u} = \partial_t\mathbf{u} + \mathbf{u}_{ALE} \cdot \nabla\mathbf{u}. \tag{4.4}$$

As a final step, in order to recover the strong formulation of the incompressible NSEs based on the RIIS method in the ALE framework, we exploit the definition of $\partial_t\mathbf{u}$ in (4.4), obtaining the following problem:

Find $\boldsymbol{u}$ *and* p *such that*:

$$\begin{cases} \rho(\partial_t^{ALE}\mathbf{u} + (\mathbf{u} - \mathbf{u}_{ALE}) \cdot \nabla\mathbf{u}) - \nabla \cdot \sigma(\mathbf{u}, p) + \frac{R}{\varepsilon}\delta_{\Gamma,\varepsilon}(\mathbf{u} - \mathbf{u}_\Gamma) = \mathbf{0} & x \in \Omega^t, \\ \nabla \cdot \mathbf{u} = \mathbf{0} & x \in \Omega^t, \\ \mathbf{u} = \mathbf{u}_{MRI} & x \in \Sigma^t, \\ \sigma(\mathbf{u}, p)\mathbf{n} = p_0\mathbf{n}_s & x \in \Sigma^t_{out}, \\ \mathbf{u}(\mathbf{x}, 0) = \mathbf{0} & x \in \Omega^0, \end{cases} \tag{4.5}$$

where the introduced term $\mathbf{u}_{MRI}$ can be identified as the wall velocity (indeed $\mathbf{u}_{MRI}$=$\dot{\mathbf{d}}_{MRI}$ is the time derivative of the displacement field projected on the computational domain wall), R and ε are the positive constants described above, $\mathbf{u}_\Gamma$ is the valve velocity prescribed as an input (often recovered by imaging), σ is the Cauchy tensor stress defined as in Eq.(4.2) and $p_0(t)$ is the aortic pressure, prescribed as an outflow condition at the distal section. The most relevant aspect to be discussed regarding this model is the resistive term, added into the Navier-Stokes Equations in the ALE approach. It consists of a multiplicative factor, defined as the ratio between the resistance coefficient R and the half-thickness of the leaflet ε, introduced by Fedele et al.[21], and consistent with the condition $\mathbf{u} = \mathbf{u}_\Gamma$ as $\varepsilon \to 0$. Indeed, in that case $\frac{R}{\varepsilon} \to \infty$, which forces $\mathbf{u}$ to be equal to the valve velocity. Moreover, the RIIS term is modeled through a smoothed Dirac function $\delta_{\Gamma,\varepsilon}$ that has centre in Γ and has support in the narrow layer around Γ with thickness ε. The distribution depends on a signed distance function ψ that assumes the value 0 for any $\mathbf{x} \in \Gamma$. Indeed the immersed mitral valve surface could be redefined in terms of the signed distance, depending on the spatial coordinates $\mathbf{x}$, as $\Gamma = \{\mathbf{x} \in \Gamma : \psi(\mathbf{x}) = 0\}$. Therefore, the smoothed Dirac function reads:

$$\delta_{\Gamma,\varepsilon}(\psi) = \begin{cases} \frac{1+cos(2\pi\psi/\varepsilon)}{2\varepsilon} & \text{if } |\psi| \leq \varepsilon, \\ 0 & \text{if } |\psi| > \varepsilon. \end{cases} \tag{4.6}$$

An important remark to make regarding the RIIS method is that the resistive term in (4.5) accounts for the mitral valve motion, integrating the underlying condition $\mathbf{u} = \mathbf{u}_\Gamma$ on the immersed surface, that, otherwise, would be difficult to model from a mathematical point of view and to implement. A consequence is that, as soon as a quasi-static approach for the mitral valve velocity $\mathbf{u}_\Gamma$ is chosen, so that $\mathbf{u}_\Gamma = \mathbf{0}$, the resistive term imposes and extends the wall motion, that will be reconstructed through the ALE approach, to the immersed surface.
An advantage of applying the RIIS method for the modeling the presence of

an immersed surface in the fluid domain relies on the lowered computational costs, with respect to other techniques hinging upon the necessary update of the fluid mesh in a neighbourhood of the valve surface through time (as ALE-based, cutFEM/XFEM or chimera overset grid methods). Precisely, RIIS method shares some aspects with the immersed boundary techniques (characterized by the independency between the computational domain and the valve surface) and the RIS method, applied in [22] and [23].

4.3 Variational formulation of the problem

Starting from the strong formulation of the CFD problem (4.5) in a moving domain with valve dynamics modeling, the aim now is to determine the correspondent weak formulation.
The idea is to set suitable functional spaces for the velocity $\mathbf{u}$ and pressure p and test functions, in order to multiply the momentum and continuum equations in (4.5) by the respective test function, integrating over the computational domain Ω^t and considering the Neumann boundary condition from the strong formulation.
Hinging upon this pipeline, we set the following functional spaces:

$$\begin{aligned} V &= \{\mathbf{v} \in [H^1(\Omega^t)]^3 : \mathbf{v}|_{\Sigma^t} = \mathbf{u}_{MRI}{}^1\}, \\ V_0 &= \{\mathbf{v} \in [H^1(\Omega^t)]^3 : \mathbf{v}|_{\Sigma^t} = \mathbf{0}\}, \\ Q &= L^2(\Omega^t). \end{aligned}$$

Taking into account the momentum equation, then, it is possible to multiply it by the test function $\mathbf{v} \in V_0$ and integrating over Ω^t:

$$\begin{aligned} &\int_{\Omega^t} \rho \partial_t^{ALE} \mathbf{u} \cdot \mathbf{v}\, d\Omega + \int_{\Omega^t} \rho(((\mathbf{u} - \mathbf{u}_{ALE}) \cdot \nabla)\mathbf{u}) \cdot \mathbf{v}\, d\Omega + \\ &- \int_{\Omega^t} \nabla \cdot \sigma(\mathbf{u}, p) \cdot \mathbf{v}\, d\Omega + \int_{\Omega^t} \tfrac{R}{\varepsilon} \delta_{\Gamma,\varepsilon}(\mathbf{u} - \mathbf{u}_\Gamma) \cdot \mathbf{v}\, d\Omega = \mathbf{0} \quad \forall \mathbf{v} \in V_0. \end{aligned}$$

Let us consider the Cauchy stress tensor divergence integral, exploiting the definition in Eq.(4.2) firstly and then integrating by parts:

$$\begin{aligned} &\int_{\Omega^t} \nabla \cdot \sigma(\mathbf{u}, p) \cdot \mathbf{v}\, d\Omega = \int_{\Omega^t} \mu \nabla \cdot (\nabla \mathbf{u} + \nabla \mathbf{u}^T) \cdot \mathbf{v}\, d\Omega - \int_{\Omega^t} \nabla p \cdot \mathbf{v}\, d\Omega = \\ &= -\mu \int_{\Omega^t} (\nabla \mathbf{u} + \nabla \mathbf{u}^T) : \nabla \mathbf{v}\, d\Omega + \int_{\partial\Omega^t} \mu \frac{\partial \mathbf{u}}{\partial \mathbf{n}} \cdot \mathbf{v}\, d\gamma - \int_{\Omega^t} p \nabla \cdot \mathbf{v}\, d\Omega + \end{aligned}$$

[1] The equality holds in the sense of the traces

$$+\int_{\partial\Omega^t} p\mathbf{v}\cdot\mathbf{n}\,d\gamma \quad \forall\mathbf{v}\in V_0. \tag{4.7}$$

Relying on the Neumann boundary conditions from the strong formulation in (4.5) and substituting the Cauchy stress tensor divergence integral with the integral sum in (4.7), the weak formulation of the momentum equation is recovered.
Repeating the procedure for the continuum equation, multiplying for the test function $q \in Q$, the following identity is obtained:

$$\int_{\Omega^t} q\nabla\cdot\mathbf{u}\,d\Omega = 0 \quad \forall q\in Q. \tag{4.8}$$

The final task to address to recover the variational formulation of the problem is to introduce the following functionals:

- the bilinear form $a: V\times V_0\to\mathbb{R}$, such that

$$a(\mathbf{u},\mathbf{v}) = \mu\int_{\Omega^t}(\nabla\mathbf{u}+\nabla\mathbf{u}^T):\nabla\mathbf{v}\,d\Omega + \int_{\Omega^t}\frac{R}{\varepsilon}\delta_{\Gamma,\varepsilon}\mathbf{u}\cdot\mathbf{v}\,d\Omega;$$

- the trilinear form $c: V\times V\times V_0\to\mathbb{R}$, such that

$$c(\mathbf{w},\mathbf{u},\mathbf{v}) = \int_{\Omega^t}((\mathbf{w}\cdot\nabla)\cdot\mathbf{u})\cdot\mathbf{v}\,d\Omega;$$

- the bilinear form $b: V\times Q\to\mathbb{R}$, such that

$$b(\mathbf{u},q) = -\int_{\Omega^t} q\nabla\cdot\mathbf{u}\,d\Omega;$$

- the linear functional $F: V_0\to\mathbb{R}$, such that

$$F(\mathbf{v}) = \int_{\Sigma^t_{out}} p_0\mathbf{n}\cdot\mathbf{v}\,d\gamma + \int_{\Omega^t}\frac{R}{\varepsilon}\delta_{\Gamma,\varepsilon}\mathbf{u}_\Gamma\cdot\mathbf{v}\,d\Omega.$$

Combing the weak formulations of the momentum and continuum equations, shown with respect to the introduced functionals, the final variational formulation of the incompressible Navier-Stokes Equations with the RIIS term in ALE framework reads:

Find $\boldsymbol{u} \in V$ *and* $p \in Q$ *for a.e.* $t \in (0, T_S]$ *such that* $\forall \mathbf{v} \in V_0$ *and* $\forall q \in Q$:

$$\begin{cases} \rho(\partial_t^{ALE}\mathbf{u}, \mathbf{v})_{\Omega^t} + \rho c(\mathbf{u} - \mathbf{u}_{ALE}, \mathbf{u}, \mathbf{v}) + a(\mathbf{u}, \mathbf{v}) + b(\mathbf{v}, p) = F(\mathbf{v}), \\ b(\mathbf{u}, q) = 0. \end{cases} \tag{4.9}$$

Where the duality in the first term of the momentum equation identifies an integral over Ω^t with the following notation:

$$(\mathbf{u}, \mathbf{v})_{\Omega^t} = \int_{\Omega^t} \mathbf{u} \cdot \mathbf{v} \, d\Omega.$$

4.4 Spatial Finite-Element discretization

4.4.1 Galerkin problem

The aim of this section is to provide a discretization in space with a finite-element approximation, derived from the weak formulation of the problem, before discretizing in time the problem and applying the stabilization techniques to the NSE.
Fixing the time instant t, the idea is to consider the Galerkin approximation of the problem (4.9), by firstly introducing a triangulation of the domain Ω^t through a finite hexahedral computational grid $\mathcal{T}_h$, where each element of the triangulation is denoted as K and its associated characteristic length with h_K.
A measure of the refinement level of the triangulation is given by the parameter h, computed as follows:

$$h = \max_{K \in \mathcal{T}_h} h_K.$$

Afterwards, let us introduce the finite dimensional subspaces $V_h \subset V$ and $Q_h \subset Q$, setting also $V_{h,0} = V_h \cap V_0 = \{\mathbf{v}_h \in V_h : \mathbf{v}_h|_{\Sigma^t} = \mathbf{0}\}$.
To build the finite dimensional subspaces V_h and Q_h, the idea is to consider the general finite element spaces X_h^r of continuous piecewise polynomials of degree r, defined as:

$$X_h^r = \{\mathbf{v}_h \in C^0(\Omega^t) : \mathbf{v}_h \in \mathbb{P}_r \text{ on } K, \ \forall K \in \mathcal{T}_h\}^2 \qquad r \in \mathbb{N}_0,$$

constructing the finite element spaces as:

$$\begin{aligned} V_h = X_h^1 \subset V, \quad \dim(V_h) = N_h < \infty \ \forall h > 0, \\ Q_h = X_h^1 \subset Q, \quad \dim(Q_h) = M_h < \infty \ \forall h > 0, \end{aligned}$$

[2] $\mathbb{P}_r$ is the functional space of polynomials with degree less or equal than r

employing so piecewise linear element spaces to define V_h and Q_h, since the aim is to achieve **linear** convergence in space. In this way, the Galerkin approximation of problem (4.9) reads:
Find $(\boldsymbol{u}_h, p_h) \in V_h \times Q_h$ *for a.e.* $t \in (0, T_S]$ *such that* $\forall \mathbf{v} \in V_{h,0}$ *and* $\forall q_h \in Q_h$:

$$\begin{cases} \rho(\partial_t^{ALE} \mathbf{u}_h, \mathbf{v}_h)_{\Omega^t} + \rho c(\mathbf{u}_h - \mathbf{u}_{ALE,h}, \mathbf{u}_h, \mathbf{v}_h) + a(\mathbf{u}_h, \mathbf{v}_h) + b(\mathbf{v}_h, p_h) = F(\mathbf{v}_h), \\ b(\mathbf{u}_h, q_h) = 0, \end{cases} \tag{4.10}$$

defining the spatial discretization of the domain velocity $\mathbf{u}_{ALE}$, $\mathbf{u}_{ALE,h}$, coming from the space discretization of 4.3.
For what concerns well-posedness of the problem, the trilinear form $c(\cdot,\cdot,\cdot)$ is continuous and coercive, while the bilinear form $b(\cdot,\cdot)$ is continuous.
In order to recover the continuity and coercivity on $V_{h,0}$ of the bilinear form $a(\cdot,\cdot)$, it is necessary to prove it, taking into account the added resistive term:

- *continuity*:

$$\begin{aligned} a(\mathbf{u}_h, \mathbf{v}_h) &= \mu \int_{\Omega^t} (\nabla \mathbf{u}_h + \nabla \mathbf{u}_h^T) : \nabla \mathbf{v}_h \, d\Omega \int_{\Omega^t} \frac{R}{\varepsilon} \delta_{\Gamma,\varepsilon} \mathbf{u}_h \cdot \mathbf{v}_h \, d\Omega \leq \\ &\leq (\mu + \frac{R}{\varepsilon^2}) \, \|\mathbf{u}_h\|_{H^1} \, \|\mathbf{v}_h\|_{H^1} \qquad \forall \mathbf{u}_h, \mathbf{v}_h \in V_{h,0}, \end{aligned}$$

- *coercivity*:

$$\begin{aligned} a(\mathbf{v}_h, \mathbf{v}_h) &= \mu \int_{\Omega^t} (\nabla \mathbf{v}_h + \nabla \mathbf{v}_h^T) : \nabla \mathbf{v}_h \, d\Omega \int_{\Omega^t} \frac{R}{\varepsilon} \delta_{\Gamma,\varepsilon} \mathbf{v}_h \cdot \mathbf{v}_h \, d\Omega \geq \\ &\geq \mu \, \|\mathbf{v}_h\|_{H^1}^2 \qquad \forall \mathbf{v}_h \in V_{h,0}, \end{aligned}$$

where we have exploited the following results for the resistive term:

$$\underset{\psi \in \mathbb{R}^+}{inf} \, \delta_{\Gamma,\varepsilon}(\psi) = 0, \qquad \underset{\psi \in \mathbb{R}^+}{sup} \, \delta_{\Gamma,\varepsilon}(\psi) = \frac{1}{\varepsilon}.$$

infimum (0) and the supremum ($\frac{1}{\varepsilon}$) of the smooth Dirac function.
Regarding the bilinear form $b(\cdot,\cdot)$, due to its "rectangular" form, to account for coercivity, a specific inequality, the *inf-sup condition*, needs to satisfied:

$$\exists \beta_h > 0 : \inf_{\substack{q_h \in Q_h \\ q_h \neq 0}} \left(\sup_{\substack{\mathbf{v}_h \in V_h \\ \mathbf{v}_h \neq 0}} \frac{b(\mathbf{v}_h, q_h)}{\|\mathbf{v}_h\|_{H^1} \, \|q_h\|_{L^2}} \right) \geq \beta_h > 0 \quad \forall h > 0, \tag{4.11}$$

with β_h positive constant that is typically independent of h. For instance if $\beta_h \to 0$ as $h \to 0$, the convergence properties of the method may be affected. The inf-sup condition (4.11) is necessary for the well-posedness of the problem. Indeed, if it is violated, i.e.:

$$\inf_{\substack{q_h \in Q_h \\ q_h \neq 0}} \left(\sup_{\substack{\mathbf{v}_h \in V_h \\ \mathbf{v}_h \neq 0}} \frac{b(\mathbf{v}_h, q^*)}{\|\mathbf{v}_h\|_{H^1} \|q_h\|_{L^2}} \right) = 0,$$

then $\exists q^* \in Q_h$ such that:

$$\sup_{\substack{\mathbf{v}_h \in V_h \\ \mathbf{v}_h \neq 0}} \frac{b(q_h, \mathbf{v}_h)}{\|\mathbf{v}_h\|_{H^1} \|q_h\|_{L^2}} = 0,$$

that implies:

$$b(\mathbf{v}_h, q_h) = 0, \quad \forall \mathbf{v}_h \in V_h.$$

Therefore, if ($\mathbf{u}_h$,p_h) is a solution of (4.10), also the pair ($\mathbf{u}_h$,p_h+q*) is a solution, entailing that the solution of the problem is not unique anymore. Elements as q^* are called *spurious pressure modes*, leading to numerical instabilites as the inf-sup condition is violated. In conclusion, the condition needs to be verified for any choice of the discrete spaces.
In this work, since linear piecewise polynomials are employed to build both V_h and Q_h, the inf-sup condition does not hold, indeed $\mathbb{P}_1$-$\mathbb{P}_1$ is not a Taylor-Hood pair, as any equal order pair of piecewise polynomials with degree $k \in \mathbb{N}$. For this reason a stabilization technique has to be employed to reach optimal convergence and solve the numerical instabilities.

4.4.2 Algebraic form of the problem

The algebraic formulation is derived by introducing the scalar basis function $\{\psi_j(\mathrm{t},\mathbf{x})\}_{j=1}^{M_h}$ for the discrete space Q_h and the vectorial basis function $\{\boldsymbol{\phi}_i(\mathrm{t},\mathbf{x})\}_{i=1}^{N_h}$ for V_h.
Regarding the vectorial ones, they are defined as follows $\forall i = 1, ..., N_h$, introducing the number of degree of freedoms (DOF) K_h for each component of the velocity (with $3K_h = N_h$):
bm

$$\boldsymbol{\phi}_i(t, \mathbf{x}) = \begin{cases} (\phi_i(t, \mathbf{x}), 0, 0) & \text{for } i = 1, ..., K_h, \\ (0, \phi_i(t, \mathbf{x}), 0) & \text{for } i = K_h + 1, ..., 2K_h, \\ (0, 0, \phi_i(t, \mathbf{x})) & \text{for } i = 2k_h + 1, ..., 3K_h, \end{cases}$$

where ϕ_i are the Lagrangian basis functions, defined for the space $H^1_{\Sigma^t}(\Omega^t) \cap V_h$. Hence the total number of DOFs is:

$$N_{DOF} = N_h + M_h = 3K_h + M_h.$$

Now, the idea is to write $\mathbf{u}_h$ and p_h as linear combinations of the basis functions lying in the respective discrete spaces. Therefore:

$$\begin{cases} \mathbf{u}_h(t) = \sum_{j=1}^{N_h} U_j(t)\boldsymbol{\phi_j}(t,\mathbf{x}), \\ p_h(t) = \sum_{k=1}^{M_h} P_k(t)\psi_k(t,\mathbf{x}), \end{cases} \tag{4.12}$$

where the coefficients $\{U_j\}_{j=1}^{3K_h}$ and $\{P_k\}_{k=1}^{M_h}$ are introduced.
Thus, since the Galerkin problem (4.10) holds true for each $\mathbf{u}_h \in V_h$ and $p_h \in Q_h$, we exploit the linear combinations in (4.12) in the discrete formulation, choosing the basis functions as test functions, i.e. $\mathbf{v}_h$=$\boldsymbol{\phi}_i(t,\mathbf{x})$ and $\mathbf{q}_h$=$\boldsymbol{\psi}_l(t,\mathbf{x})$, $\forall i = 1, ..., N_h$ and $\forall l = 1, ..., M_h$.
Therefore, the following system is obtained:

$$\begin{cases} \rho \sum_{j=1}^{N_h} \partial_t^{ALE}\left(U_j(t)\boldsymbol{\phi_j}(t,\mathbf{x}), \boldsymbol{\phi_i}(t,\mathbf{x}) \right) + \\ \quad \rho c\left(\sum_{s=1}^{N_h} U_s(t)\boldsymbol{\phi_s}(t,\mathbf{x}) - \mathbf{u}_h^{ALE}(t), \sum_{j=1}^{N_h} U_j(t)\boldsymbol{\phi_j}(t,\mathbf{x}), \boldsymbol{\phi_i}(t,\mathbf{x}) \right) + \\ \quad + \sum_{j=1}^{N_h} U_j(t) a(\boldsymbol{\phi_j}(t,\mathbf{x}), \boldsymbol{\phi_i}(t,\mathbf{x})) + \sum_{k=1}^{M_h} P_k(t) b(\boldsymbol{\phi_i}(t,\mathbf{x}), \psi_k(t,\mathbf{x})) = \\ \quad = F(\boldsymbol{\phi_i}(t,\mathbf{x})), \\ \sum_{j=1}^{N_h} U_j(t) b(\boldsymbol{\phi_j}(t,\mathbf{x}), \psi_l) = 0. \end{cases} \tag{4.13}$$

The definition of ALE derivative can be exploited to reformulate the first term in the left hand side of the momentum equation, thanks to the fact that basis functions time variation is null with respect to the reference frame:

$$\sum_{j=1}^{N_h} \partial_t^{ALE}\left(U_j(t)\boldsymbol{\phi_j}(t,\mathbf{x}), \boldsymbol{\phi_i}(t,\mathbf{x}) \right) = \sum_{j=1}^{N_h} \frac{dU_j(t)}{dt}\boldsymbol{\phi_j}(t,\mathbf{x}).$$

Let us introduce the vectors $\mathbf{U}$=$(U_1(t),...,U_{N_h}(t))^T$, $\mathbf{P}$=$(P_1(t),...,P_{M_h}(t))^T$ and $\mathbf{F}$=$(F(\boldsymbol{\phi_1}(\mathrm{t},\mathbf{x})),...,F(\boldsymbol{\phi_{N_h}}(\mathrm{t},\mathbf{x})))^T$. Subsequently, the following matrices are built:

- the *mass matrix* $M \in \mathbb{R}^{N_h \times N_h}$, such that:

$$M_{ij} = \int_{\Omega^t} \boldsymbol{\phi_j} \cdot \boldsymbol{\phi_i} d\Omega, \tag{4.14}$$

- the *convective matrix* $N \in \mathbb{R}^{N_h \times N_h}$, such that:

$$[N(\mathbf{U}(t) - \mathbf{U}_{ALE}(t)]_{ij} = c(\mathbf{u}_h(t) - \mathbf{u}_{ALE,h}(t), \boldsymbol{\phi_j}, \boldsymbol{\phi_i}), \tag{4.15}$$

- the *stiffness matrix* $A \in \mathbb{R}^{N_h \times N_h}$, such that:

$$A_{ij} = a(\boldsymbol{\phi_j}, \boldsymbol{\phi_i}), \tag{4.16}$$

- the matrix $B \in \mathbb{R}^{M_h \times N_h}$, such that:

$$B_{lj} = b(\boldsymbol{\phi_j}, \psi_l). \tag{4.17}$$

Relying on the bilinearity of $a(\cdot,\cdot)$ and $b(\cdot,\cdot)$ and on the trilinearity of $c(\cdot,\cdot,\cdot)$, from the system (4.13) the following algebraic formulation defined by a non-linear system with Ordinary Differential Equations (ODE) is obtained, with $\mathbf{U}(t)$ and $\mathbf{P}(t)$ unknowns and initial condition $\mathbf{U}(0)$=$\mathbf{0}$ ($\in \mathbb{R}^{N_h}$):

$$\begin{cases} \rho M\dot{\mathbf{U}}(t) + \rho N(\mathbf{U}(t) - \mathbf{U}_{ALE}(t))\mathbf{U}(t) + A\mathbf{U}(t) + B^T\mathbf{P}(t) = \mathbf{F}(t), \\ B\mathbf{U}(t) = 0. \end{cases} \tag{4.18}$$

4.5 Time discretization

After defining the system of ODEs (4.18), the task to be addressed in this section is to fully-discretize the problem, providing a time-discretization of (4.18), coupled with a discretization of (4.3). This procedure relies on the following pipeline, hinging upon key points:

- **Refined partition of the time interval**: given a uniform time step Δt, the idea is to partition the interval $(0, T_S]$ and denote with $(\mathbf{u}^n, p^n)$ the approximation of the exact solution $(\mathbf{u}(t^n), p(t^n))$, at time $t^n = n\Delta t$, $\forall n = 0, ..., N$, with $N = \frac{T_S}{\Delta t}$.

- **Time interpolation of the displacement datum**: since a refined partition of time interval is derived, the cine-MRI displacement data $\hat{\mathbf{d}}_{MRI}$ should be now interpolated on a finer grid, introducing $\hat{\mathbf{d}}^n_{MRI}$ $\forall n = 0, ..., N$.

- **Time discretization scheme**: Several schemes are employed for Navier-Stokes Equations, subdivided in explicit, semi-implicit and implicit methods.
  The explicit techniques have an important limitation related to the bound of parabolic type on the time step Δt, such that $\Delta t \lesssim h^2$. It is a restrictive condition, since in most fluid-dynamics applications a refined grid is considered, with a small value of h. Instead, implicit discretizations provide *unconditionally absolute stability*, but the resulting algebraic system to be solved is non-linear, so it is necessary to linearize it through a Fixed-Point or Newton method. Semi-implicit techniques avoid linearizations and restrictive time step bounds, with a milder CFL-like stability condition: $\Delta t \lesssim h$, satisfied in hemodynamics by the Δt needed for accuracy purposes.
  For this reason, in this work a semi-implicit first-order Euler scheme is applied to the algebraic system.

- **ALE mapping from the solution of the lifting problem**: regarding the computational domain motion in the ALE framework, a family of mappings $\mathcal{A}^t$ is introduced, where, for each $t \in (0, T_S]$, a function associated to each point of the reference configuration domain Ω^0 a point on the current configuration domain Ω^t. The main advantage is that the motion is reconstructed in a refined grid (with respect to time), the mesh is updated without that a new one is generated and the ALE approach for the transient hemodynamics affects the finite-element discretization by moving the basis functions in a conform way ([9][82]).
  Find $\hat{\mathbf{d}}_h^{n+1} \in V_h^0$ *with* $\hat{\mathbf{d}}_h^{n+1} = \hat{\mathbf{d}}_{MRI}^{n+1}$ *on the boundary such that* :

$$(\nabla \hat{\mathbf{d}}_h^{n+1}, \nabla \mathbf{v}_h) = 0, \quad \forall \mathbf{v}_h \in V_h^0, \tag{4.19}$$

  We then define each mapping as:

$$\mathcal{A}^{n+1} : \Omega^0 \to \mathbb{R}^3, \quad \mathcal{A}^{n+1}(\hat{x}) = \hat{x} + \hat{\mathbf{d}}_h^{n+1}, \tag{4.20}$$

- **Update of domain, finite element spaces and valve location**: subsequently, the domain and the triangulation are updated (and so the finite element spaces V_h and Q_h to V_{h+1} and Q_{h+1}) for the next time step:

$$\Omega^{n+1} = \mathcal{A}^{n+1}(\Omega^0), \quad \mathcal{T}_h^{n+1} = \mathcal{A}^{n+1}(\mathcal{T}_h^0). \tag{4.21}$$

An important remark to be made concerns the mitral valve Γ. For each time instant, the valve presence is accounted for by the RIIS method and the immersed surface is included in the boundary portion Σ^t. Since a zero-displacement field is assigned for Γ, the valve follows the wall motion, modeled through the interpolated-in-time displacement field $\hat{\mathbf{d}}_{MRI}$. In the ALE framework this means that, fixed the time instant t^n from the refined grid, the discretized velocity $\mathbf{u}_h^n$ in the ventricular, aortic and immersed valve surface boundary is evaluated as $\mathbf{u}_h^n = \mathbf{u}_{ALE,h}^{n-1}$. In particular, the mitral valve position Γ^n is updated, exploiting the aforementioned interpolated displacement datum.

- **Discretization of the integrals and the domain velocity**: afterwards, also the terms in the integrals over the current configuration domain Ω^{n+1} are discretized, along with the domain velocity $\mathbf{u}_{ALE,h}$:

$$\mathbf{u}_{ALE,h}^{n+1} = \frac{\hat{\mathbf{d}}_h^{n+1} - \hat{\mathbf{d}}_h^n}{\Delta t}. \tag{4.22}$$

- **Deriving the final algebraic formulation**: from Eq.(4.22), the approximated first order derivative can be computed as follows:

$$\partial_t^{ALE}\mathbf{u}_h(t^{n+1}) = \frac{\mathbf{u}_h(t^{n+1}) - \mathbf{u}_h(t^n)}{\Delta t} + \mathcal{O}(\Delta t), \tag{4.23}$$

leading to the final fully-discrete formulation of problem (4.5), identified through the following system of ODEs, $\forall n = 0, ..., N-1$, having $\mathbf{U}^0 = \mathbf{0}$:

$$\begin{cases} \rho M\mathbf{U}^{n+1} + \rho N(\mathbf{U}^n - \mathbf{U}_{ALE}^{n+1})\mathbf{U}^{n+1} + A\mathbf{U}^{n+1} + B^T\mathbf{P}^{n+1} = \widetilde{\mathbf{F}}, \\ B\mathbf{U}^{n+1} = 0. \end{cases} \tag{4.24}$$

In particular, the discretized right hand-side of the algebraic momentum equation is computed as follows:

$$\widetilde{\mathbf{F}} = \rho\frac{M}{\Delta t}\mathbf{U}^n + \int_{\Omega_h^{n+1}} \frac{R}{\varepsilon}\delta_{\Gamma,\varepsilon}\mathbf{u}_\Gamma \cdot \mathbf{v}_h \, d\Omega. + \int_{\Sigma_{out}^{n+1}} p_0(t^{n+1})\mathbf{n} \cdot \mathbf{v}_h \, d\gamma.$$

- **Linear system**: a compact form of the system of ODEs (4.24) can be obtained as follows, setting $\mathbf{U}^* = \mathbf{U}^n - \mathbf{U}_{ALE}^{n+1}$:

$$\begin{bmatrix} \rho\frac{M}{\Delta t} + A + N(\mathbf{U}^*) & B^T \\ B & 0 \end{bmatrix} \begin{bmatrix} \mathbf{U}^{n+1} \\ \mathbf{P}^{n+1} \end{bmatrix} = \begin{bmatrix} \widetilde{\mathbf{F}} \\ 0 \end{bmatrix}. \tag{4.25}$$

The choice of a semi-implicit method leads to a mild bound on the time step Δt, with the following CFL-like stability condition:

$$\Delta t \leq C \frac{h}{\|\mathbf{u}_h\|_{L^\infty}} \qquad with\ C \in \mathbb{R}^+,$$

4.6 Stabilization of the fully-discretized problem

As already mentioned, the well-posedness of the discrete problem is related to the choice of a Taylor-Hood pair for the finite-element discretization. Since the discrete spaces V_h and Q_h are obtained from the pair $\mathbb{P}_1 - \mathbb{P}_1$, the inf-sup condition is violated and spurious pressure modes are generated, affecting the optimal convergence of the method.
For what concerns the velocity field, a relevant source of numerical instabilities is associated to the fact that a Galerkin approach is employed to solve the Navier-Stokes equations in a regime that is advection-dominated in hemodynamics. The consequence is that stabilization techniques are required in case of large Reynolds number due to the semi-implicit treatment of the convective term.
For this reason, in order to deal with the two aforementioned sources of instabilities, we employ a Streamline Upwind Petrov-Galerkin along with a Pressure-Stabilizing Petrov-Galerkin (SUPG-PSPG) approach [83].
We introduce the following stabilization term to be added to the Galerkin formulation 4.10:

$$s(\mathbf{u}_h^{n+1}, p_h^{n+1}; \mathbf{v}_h, q_h) = \gamma \sum_{K \in \mathcal{T}^{n+1}} \tau \int_K [\mathcal{L}(\mathbf{u}_h^{n+1}, p_h^{n+1}) - \mathcal{F}]^T \mathcal{L}_{ss}(\mathbf{v}_h, q_h)\, d\Omega,$$

where we have introduced the positive constant γ, the stabilization parameter τ, the residual of the Navier-Stokes Equations $\mathcal{L}(\cdot,\cdot) - \mathcal{F}$, through the following functionals (setting $\mathbf{u}^* = \mathbf{u}_h^n - \mathbf{u}_{ALE,h}^{n+1}$):

$$\mathcal{L}(\mathbf{u}_h^{n+1}, p_h^{n+1}) =$$

$$= \begin{bmatrix} \rho\frac{\mathbf{u}_h^{n+1}-\mathbf{u}_h^n}{\Delta t} + \rho(\mathbf{u}^*\cdot\nabla)\mathbf{u}_h^{n+1} + \nabla p_h^{n+1} - \mu\Delta\mathbf{u}_h^{n+1} + \frac{R}{\varepsilon}\delta_{\Gamma,\varepsilon}(\mathbf{u}_h^{n+1}-\mathbf{u}_\Gamma) \\ \nabla\cdot\mathbf{u}_h^{n+1} \end{bmatrix},$$

$$\mathcal{F} = \begin{bmatrix} \mathbf{0} \\ 0 \end{bmatrix},$$

and the functional $\mathcal{L}_{ss}(\cdot,\cdot)$, representing the skew-symmetric part of $\mathcal{L}(\cdot,\cdot)$, defined as:

$$\mathcal{L}_{ss}(\mathbf{v}_h, q_h) = \begin{bmatrix} \rho(\mathbf{u}^*\cdot\nabla)\mathbf{v}_h + \nabla q_h \\ 0 \end{bmatrix}.$$

Then the SUPG-PSPG stabilization of the Galerkin discretization of problem (4.5) reads:
Assuming $\mathbf{u}^* = \mathbf{u}_h^n - \mathbf{u}_{ALE,h}^{n+1}$, $\forall n = 0, ..., N-1$, *fixed* $t^n = n\Delta t$, *find* $(\hat{\mathbf{u}}_h^{n+1}, p_h^{n+1}) \in V_h^{n+1} \times Q_h^{n+1}$, *such that* $\mathbf{u}_h^0 = \mathbf{0}$ *and* $\forall \mathbf{v}_h \in V_{h,0}^n$ *and* $\forall \mathbf{q}_h \in Q_h^n$:

$$\begin{aligned} \rho\left(\frac{\mathbf{u}_h^{n+1}}{\Delta t}, \mathbf{v}_h\right) + \rho\, c(\mathbf{u}^*, \mathbf{u}_h^{n+1}, \mathbf{v}_h)_{\Omega^{n+1}} + a(\mathbf{u}_h^{n+1}, \mathbf{v}_h) + \\ + b(\mathbf{v}_h, p_h^{n+1}) - b(\mathbf{u}_h^{n+1}, q_h) + \\ + s(\mathbf{u}_h^{n+1}, p_h^{n+1}; \mathbf{v}_h, q_h) = \\ = F(\mathbf{v}_h), \end{aligned} \tag{4.26}$$

where the added stabilization term, that involves the product between the residual of the strong formulation $\mathcal{L}(\mathbf{u}, p) - \mathcal{F}$ and its skew-symmetric part $\mathcal{L}_{SS}(\mathbf{u}, p)$, is evaluated as follows:

$$s(\mathbf{u}_h^{n+1}, p_h^{n+1}; \mathbf{v}_h, q_h) =$$

$$= \sum_{K\in\mathcal{T}^{n+1}} \left(\tau_M(\mathbf{u}_h^n - \mathbf{u}_{ALE,h}^{n+1})\mathbf{r}_M^{n+1}(\mathbf{u}_h^{n+1}, p_h^{n+1}),\ \rho(\mathbf{u}_h^n - \mathbf{u}_{ALE,h}^{n+1})\cdot\nabla\mathbf{v}_h + \nabla q_h\right)_{\Omega^{n+1}} +$$

$$+ \sum_{K\in\mathcal{T}^{n+1}} \left(\tau_C(\mathbf{u}_h^n - \mathbf{u}_{ALE,h}^{n+1}) r_C(\mathbf{u}_h^{n+1}), \nabla\cdot\mathbf{v}_h)\right)_{\Omega^{n+1}},$$

where:

$$\begin{bmatrix} \mathbf{r}_M^{n+1}(\mathbf{u}, p) \\ r_C(\mathbf{u}, p) \end{bmatrix} = \begin{bmatrix} \rho(\frac{\mathbf{u}-\mathbf{u}_h^n}{\Delta t} + (\mathbf{u}_h^n - \mathbf{u}_{ALE,h}^{n+1})\cdot\nabla\mathbf{u}) + \nabla p - \mu\Delta\mathbf{u} + \frac{R}{\varepsilon}\delta_{\Gamma^{n+1},\varepsilon}\mathbf{u} \\ \nabla\cdot\mathbf{u} \end{bmatrix},$$

and the parameters τ_M and τ_C are chosen according to the variational multiscale approach [94][95]. They are local coefficients depending on the mesh element size h_K and the velocity magnitude. They are computed as follows:

$$\begin{cases} \tau_M(\mathbf{u}) = \left(\frac{\rho^2}{\Delta t^2} + \frac{\rho^2}{h_K^2}|\mathbf{u}|^2 + 30\frac{\mu^2}{h_K^4} + \frac{R^2}{\varepsilon^2}\delta^2_{\Gamma^{n+1},\varepsilon} \right)^{-\frac{1}{2}}, \\ \tau_C(\mathbf{u}) = \frac{h_K^2}{\tau_M(\mathbf{u})}. \end{cases}$$

Setting $\mathbf{u}^* = \mathbf{u}_h^n - \mathbf{u}_{ALE,h}^{n+1}$, in order to recover the corresponding algebraic formulation of the stabilized problem (4.6), we decompose the definition of the stabilizing term $s(\mathbf{u}_h^{n+1}, p_h^{n+1}; \mathbf{v}_h, q_h)$, introducing the following stabilization matrices:

$$S_{11}^{(1)} = \left(\rho\frac{\mathbf{u}_h^{n+1}}{\Delta t}, \rho\mathbf{u}^* \cdot \nabla \mathbf{v}_h \right)_{\Omega^{n+1}}, \qquad S_{21}^{(1)} = \left(\rho\frac{\mathbf{u}_h^{n+1}}{\Delta t}, \nabla q_h \right)_{\Omega^{n+1}},$$

$$S_{11}^{(2)} = \left(\rho\mathbf{u}^* \cdot \nabla \mathbf{u}_h^{n+1}, \rho\mathbf{u}^* \cdot \nabla \mathbf{v}_h \right)_{\Omega^{n+1}}, \qquad S_{21}^{(2)} = \left(\rho\mathbf{u}^* \cdot \nabla \mathbf{u}_h^{n+1}, \nabla q_h \right)_{\Omega^{n+1}},$$

$$S_{11}^{(3)} = \left(-\mu\Delta \mathbf{u}_h^{n+1}, \rho\mathbf{u}^* \cdot \nabla \mathbf{v}_h \right)_{\Omega^{n+1}}, \qquad S_{21}^{(3)} = \left(-\mu\Delta \mathbf{u}_h^{n+1}, \nabla q_h \right)_{\Omega^{n+1}},$$

$$S_{11}^{(4)} = \left(\frac{R}{\varepsilon}\delta_{\Gamma,\varepsilon}\mathbf{u}_h^{n+1}, \rho\mathbf{u}^* \cdot \nabla \mathbf{v}_h \right)_{\Omega^{n+1}}, \qquad S_{21}^{(4)} = \left(\frac{R}{\varepsilon}\delta_{\Gamma,\varepsilon}\mathbf{u}_h^{n+1}, \nabla q_h \right)_{\Omega^{n+1}},$$

$$S_{11}^{(5)} = \left(\nabla \cdot \mathbf{u}_h^{n+1}, \rho\mathbf{u}^* \cdot \nabla \mathbf{v}_h \right)_{\Omega^{n+1}},$$

$$S_{12} = \left(\nabla p_h^{n+1}, \rho\mathbf{u}^* \cdot \nabla \mathbf{v}_h \right)_{\Omega^{n+1}}, \qquad S_{22} = \left(\nabla p_h^{n+1}, \nabla q_h \right)_{\Omega^{n+1}},$$

that identify the following monolithic stabilizing matrix:

$$\Sigma = \begin{bmatrix} \Sigma_{11} & \Sigma_{12} \\ \Sigma_{21} & \Sigma_{22} \end{bmatrix} = \begin{bmatrix} \sum_{n=1}^{5} S_{11}^{(n)} & S_{12} \\ \sum_{n=1}^{4} S_{21}^{(n)} & S_{22}, \end{bmatrix} \tag{4.27}$$

to be added to the block matrix in the linear system (4.25).
Moreover we define the following vectors, to be summed to the right hand side in the algebraic formulation (4.25):

$$\mathbf{F}_u = \left(\rho\frac{\mathbf{u}_h^n}{\Delta t}, \rho\mathbf{u}^* \cdot \nabla \mathbf{v}_h \right)_{\Omega^{n+1}}, \qquad \mathbf{F}_p = \left(\rho\frac{\mathbf{u}_h^n}{\Delta t}, \nabla q_h \right)_{\Omega^{n+1}}.$$

Hence, the SUPG-PSPG stabilized Navier-Stokes monolithic system reads: *Assuming* $\mathbf{U}^* = \mathbf{U}^n - \mathbf{U}_{ALE}^{n+1}$, $\forall\, n = 0, ..., N-1$, *having* $\mathbf{U}^0 = \mathbf{0}$:

$$\begin{bmatrix} \widetilde{A} & B^T + S_{12}^T \\ \widetilde{B} & S_{22} \end{bmatrix} \begin{bmatrix} \mathbf{U}^{n+1} \\ \mathbf{P}^{n+1} \end{bmatrix} = \begin{bmatrix} \widetilde{\mathbf{F}} + \mathbf{F}_u \\ \mathbf{F}_p, \end{bmatrix} \tag{4.28}$$

with:

$$\widetilde{A} = \rho\tfrac{M}{\Delta t} + A + N(\mathbf{U}^*) + \textstyle\sum_{n=1}^{5} S_{11}^{(n)}; \qquad \widetilde{B} = B + \textstyle\sum_{n=1}^{4} S_{21}^{(n)}$$

The choice of a stabilization term $s(\cdot,\cdot)$ is critical, since it guarantees uniform convergence to the method. Indeed, stability and convergence results derive from the two following conditions that $s(\cdot,\cdot)$ yields to the system:

- *generalized inf-sup condition*: $\exists \beta_h > 0$ *suchthat*:

$$\sup_{\substack{\mathbf{v}_h \in V_h \\ \mathbf{v}_h \neq 0}} \frac{b(\mathbf{v}_h, q_h)}{\|\mathbf{v}_h\|_{H^1}} + s(q_h, p_h) \geq \beta_h \|q_h\|_{L^2} \quad \forall q_h \in Q_h$$

- *consistency*:

$$s(q_h, p_h) \to 0, \quad as\ h \to 0.$$

In **Algorithm 1**, the pipeline for the numerical analysis of the mathematical model shown in Section 4.2 is depicted.

Algorithm 1: Outline of the solution procedure

Data: Ω^0; $\mathbf{d}_{MRI}$; T_S

Output: $\Omega^n, \mathbf{u}_h^n, p_h^n \ \forall n = 0, ..., N$;

1 Triangulation of Ω^0=$\Omega(0)$ into $\mathcal{T}_h^0$ and definition of V_h^0 and Q_h^0 for velocity $\mathbf{u}_h$ and pressure p_h

2 Partition of time interval $(0, T_S]$ into a finer grid

3 **for** *n=0,1,...,N-1* **do**

- Compute $\hat{\mathbf{d}}_{MRI}^{n+1} : \partial\Omega^{n+1} \to \mathbb{R}^3$ interpolating the datum $\mathbf{d}_{MRI}$ between coarse MRI temporal sub-intervals and refined time interval discretization.
- Solve the ALE harmonic extension problem (4.19) to obtain the fluid domain displacement $\hat{\mathbf{d}}_h^{n+1}$.
- Update the computational domain Ω^{n+1}, the triangulation $\mathcal{T}^{n+1}$ (and the finite element spaces) and the mitral valve location Γ^{n+1} through the ALE map $\mathcal{A}^{n+1} : \Omega^0 \to \mathbb{R}^3$, $\mathcal{A}^{n+1}(\mathbf{x}) = \mathbf{x} + \hat{\mathbf{d}}_h^{n+1}$.
- Solve a time step of the SUPG-stabilized linearized discrete problem (4.28), with semi-implicit first order Euler time discretization.

4.7 Solution of the linear system

In order to compute the solution of the incompressible Navier-Stokes Equation in a homogeneous-Newtonian fluid domain relying on the ALE approach and including the mitral valve dynamics, it is necessary to solve, for a fixed time step, the SUPG-stabilized linearized problem (4.28).
In this section, the idea is to present the linear solver that addresses the task of finding, for each time instant, the solution of the stabilized linear discrete problem, untangling the inner algebraic issues.

4.7.1 The Generalized Minimal Residual Method

Recall the algebraic formulation of the discrete problem as in (4.28):
Assuming $\mathbf{U}^* = \mathbf{U}^n - \mathbf{U}_{ALE}^{n+1}$:

$$\begin{bmatrix} \widetilde{A} & B^T + S_{12}^T \\ \widetilde{B} & S_{22} \end{bmatrix} \begin{bmatrix} \mathbf{U}^{n+1} \\ \mathbf{P}^{n+1} \end{bmatrix} = \begin{bmatrix} \widetilde{\mathbf{F}} + \mathbf{F}_u \\ \mathbf{F}_p, \end{bmatrix} \tag{4.29}$$

The system can be rewritten in a compact way by normalizing the right-hand side as $\hat{A}\mathbf{x} = \mathbf{b}$. It is *non-symmetric* and *undefined* system (with positive and negative eigenvalues). Moreover it carries features that can entail high computational costs and slow convergence for an iterative method. For this reason we employ a Krylov Method, hinging upon a preconditioning procedure, so that the computational performance improves. Because of the non-symmetry, the minimal residual method (MINRES) cannot be employed (suitable only for symmetric systems). Instead, an extension of the MINRES, the *Generalized Minimal Residual Method* (GMRES), can be applied and coupled with a specific preconditioner.
Supposing that $\hat{A} \in \mathbb{R}^{m\times m}$ and $\mathbf{b} \in \mathbb{R}^m$. The starting point is to consider the following *Krylov sequence*:

$$\mathcal{K}_n = \mathcal{K}_n(\hat{A}, \mathbf{r}_0) = span\{\mathbf{r}_0, \hat{A}\mathbf{r}_0, \hat{A}^2\mathbf{r}_0, ..., \hat{A}^{n-1}\mathbf{r}_0\},$$

where $\mathbf{r}_0 = \hat{A}\mathbf{x} - \mathbf{b}$ is the initial error, given the initial guess $\mathbf{x}_0$ different from 0.
Afterwards the following space is defined, relying on the definition of the Krylov sequence:

$$W_n = \{\mathbf{v} = \mathbf{x}_0 + \mathbf{y},\ \ \mathbf{y} \in \mathcal{K}_n\}.$$

The aim is approximating the exact solution of $\mathbf{x}$=$\mathbf{b}$ by a vector $\mathbf{x}_n \in \mathcal{K}_n$ minimizing the L2-norm of the residual $\mathbf{r}_n = \hat{A}\mathbf{x}_n - \mathbf{b}$. The minimizer is found among all the vectors in W_n minimizing the L2-norm of $\hat{A}\mathbf{v} - \mathbf{b}$.
The GMRES approach relies on computing an orthonormal basis $\{\mathbf{q}_k\}_{k=1}^n$ by applying an orthogonalization procedure called *Arnoldi method* [87], a modified Gram-Schimdt orthonormalization technique, due to the fact that the vectors in the basis of $\mathcal{K}_n$ are close to linearly dependent. The first Arnoldi iterate, $\mathbf{q}_1$, is defined as:

$$\mathbf{q}_1 = \|\mathbf{r}_0\|_{L^2}^{-1}\, \mathbf{r}_0.$$

For each iteration k=$1, ..., n$, the GMRES method consists of the following pipeline:

1. compute the Arnoldi iterate $\mathbf{q}_k$ and define the matrix Q_k with the the basis vectors $\mathbf{q}_1, ..., \mathbf{q}_k$ columns;

2. introduce $\mathbf{y}_k \in \mathbb{R}^k$ such that the following decomposition holds: $\mathbf{x}_k = Q_k\mathbf{y}_k$. Along with the last identity, define the Hessenberg matrix [88][89] $\mathrm{H}_n \in \mathbb{R}^{(k+1)\times k}$, such that $\hat{A}Q_k = Q_{k+1}H_k$;

3. compute the L2-norm of the residual as follows:

$$\|\mathbf{r}_k\|_{L^2} = \left\|\hat{A}Q_kH_k - \mathbf{b}\right\|_{L^2} = \|Q_kH_k\mathbf{y}_k - \mathbf{b}\|_{L^2};$$

4. consider the equality $Q^*_{k+1}\mathbf{b} = \|\mathbf{b}\|_{L^2}\,\mathbf{e}_1$, with $\mathbf{e}_1 = (1, ..., 0)^T \in \mathbb{R}^{k+1}$ and minimize:

$$\|\mathbf{r}_k\|_{L^2} = \|H_k\mathbf{y}_k - \|\mathbf{b}\|_{L^2}\,\mathbf{e}_1\|_{L^2}$$

5. evaluate $\mathbf{x}_k = Q_k\mathbf{y}_k$ and repeat the procedure if the residual still exceeds the tolerance.

4.7.2 Preconditioning method

The GMRES is a Krylov method, so it relies on preconditioning, due to the fact the the block matrix $\hat{A}$ is ill-conditioned and the convergence rate depends on the spectral properties of $\hat{A}$.
Introducing a linear operator P, it is an optimal preconditioner if:

- $P \approx \hat{A}$, in order to have $P^{-1}\hat{A} \approx I$;
- the convergence performance of the preconditioned system is improved with respect to the original one;
- P or P^{-1} can be built in parallel.

As a consequence, if these properties are satisfied, it is possible to precondition the linear system, so that of these two new problems is formulated:

- $P^{-1}\hat{A}\mathbf{x} = P^{-1}\mathbf{b}$ *left-preconditioning*;
- $\hat{A}P^{-1}P\mathbf{x} = \mathbf{b}$.

In this work we employ the SIMPLE preconditioner [86], obtained by inexact block LU factorization, decomposing the block matrix of (4.30) in the following lower triangular and upper triangular matrices:

$$\begin{bmatrix} \widetilde{A} & B^T \\ B & 0 \end{bmatrix} = \begin{bmatrix} \widetilde{A} & 0 \\ B & -\Sigma \end{bmatrix} \begin{bmatrix} I & \widetilde{A}^{-1}B^T \\ 0 & I \end{bmatrix}.$$

Afterwards we introduce the following preconditioner, where $D_{\widetilde{A}}$ is the diagonal matrix of $\widetilde{A}$:

$$P = \begin{bmatrix} D_{\widetilde{A}} & 0 \\ B & -BD^{-1}_{\widetilde{A}}B^T \end{bmatrix} \begin{bmatrix} I & D^{-1}_{\widetilde{A}}B^T \\ 0 & I \end{bmatrix}, \tag{4.30}$$

that approximates the original fluid block matrix since $D_{\widetilde{A}} \approx \widetilde{A}$ and $BD^{-1}_{\widetilde{A}}B^T \approx \Sigma$.

Chapter 5

Numerical results and clinical indications

In this chapter, for each of the HCM patients analyzed during the image processing phase, we are going to present the numerical results of the simulation of the CFD problem introduced in Chapter 4. The aim is to exploit the reconstruction pipeline and the computational methods to assess the effect of Hypertrophic Cardiomyopathy on the global cardiac performance and the hemodynamics of the patients during the systolic phase. Relevant outputs of interest will be inspected, as velocity distribution, pressure gradients and aortic jet evolution. In particular, in order to address the obstruction severity, the evaluation of the pressure along the septum provides quantitative measures about the spatial location and extension of the obstruction. The goal is to support clinical decision-making for the design of a surgical treatment of possible pathologically relevant HOCM cases, for example by means of septal myectomy (see Section 5.2.2).
Moreover, the analysis of the Wall-Shear-Stress can yield information about possible wall damages induced by the blood flow and the aortic jet [91], whilst the Q-criterion can provide details about the effects of HCM on the hemodynamics in terms of turbulent and vortex structures development [90].

5.1 Computational aspects

5.1.1 The computational toolkit for the simulations

The numerical problem, with first-order semi-implicit time discretization and SUPG-stabilized Finite Element discretization, is implemented through the multiphysics high-performance C++ finite element library life^X

(https://gitlab.com.com/lifex/lifex), hinging upon the deal.II core (https://www.dealii.org) and devoloped by MOX Laboratory of Politecnico di Milano in the iHEART project. The library includes different solvers for problems related to cardiac applications, concerning, for instance, fluid-dynamics, elastodynamics, fluid-structure interaction or electrophysiology.
The numerical simulations have been performed in parallel, relying on the clustered computational resources of Politecnico di Milano, in particular running over tests in the queue *gigatlong* on a processor relying on 5 nodes with 160 cores 4x Intel®Xeon®E5-4610 v2 (2.3GHz) 1.2TB RAM.
Patient 1's simulation duration has been of 60 hours in a HPC node with 20 cores selected, while in the case of Patient 2 the duration has been of 72 hours, choosing 32 cores, in order to deal with the higher number of degree of freedoms and active cells.
Regarding Patient 1, the computational mesh is characterized by approximately 300.000 active cells and 1.3 milions of DOFs, while Patient 2 mesh has approximately 420.000 active cells and 1.9 milions of active cells (due to its dilated left ventricle and aortic root). In order to start a simulation with the life^x library, two main input files need to be provided:

- the *parameters file*: a script in the *.prm* format containing the needed information related to the physical parameters and the addressed tags of the domain boundary to impose the Dirichlet or Neumann boundary conditions. Moreover, the script includes the path of the computational mesh, the mitral valve surface, and the displacement data *.vtp* file, along with the input commands for the lifting and fluid problem solvers;

- the $lifex\_fluid\_dynamics.cpp$ file: the file implementing the discretized Navier-Stokes Equations with the RIIS term in a moving domain in ALE framework and with the valve dynamics. The input file is the aforementioned parameter file, thanks to which the boundary conditions are assigned and the parameters are set.

5.1.2 Physical parameters and boundary conditions assessment

Provided the computational domain for each patient under investigation (Figure 5.1), in this section the focus is on the input parameters of the physical problem and the boundary conditions of the Navier-Stokes Equations.

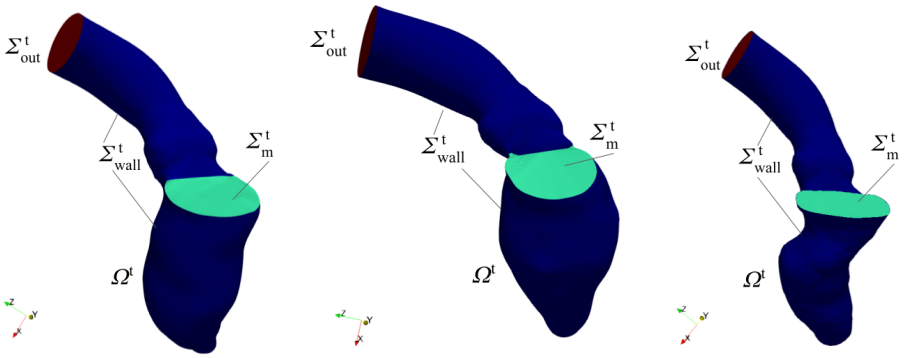

Figure 5.1: Computational domain of each patient under investigation, where a Neumann boundary condition is assigned to Σ^t_{out} and a Dirichlet boundary condition is prescribed to $\Sigma^t = \Sigma^t_{wall} \cup \Sigma^t_m$

For what concerns the latter, a Neumann boundary condition is prescribed at the distal aortic section Σ^t_{out}, where a time-dependent pressure function p_0 is assigned through the tag identifying the aortic outflow section. The prescribed pressure term is a third-order polynomial, identifying a physiological pressure waveform, derived from Wiggers diagram [81] and shown in Figure 5.2. The polynomial $p_0(t)$ is defined as follows:

$$p_0(t) = 80 + 140t + 390t^2 - 1400t^3$$

In this way, the maximum pressure value is reached for t=0.3 s.
The idea of prescribing a physiological pressure hinges upon the fact that in this work we are interested into assessing the effect of HCM. As a consequence, quantifying the deviation from the physiological behaviour (extrapolated from the Wiggers diagram) and inspecting the patient-specific pressure gradient provide interesting indications to evaluate the severity of the pathology.
For what concerns the valve velocity $\mathbf{u}_\Gamma$, in this first work, it will be set to 0, provided a zero-displacement field for the mitral valve (as stated in Chapter 3). Indeed, the idea of prescribing a zero-velocity field to $\mathbf{u}_\Gamma$, choosing a quasi-static approach, derives from the fact that in this work SAM-affected patients are not inspected, so the effect of the leaflet tip is not relevant. In other cases, as for example with Patient 3, aside from reiterating the quasi-static approach and neglecting the effects of SAM on the leaflet tip velocity, it could also be possible to solve an additional structural problem or to reconstruct the motion from clinical images, increasing the computational costs and efforts. A consequence, as stated in Section (4.3), is that

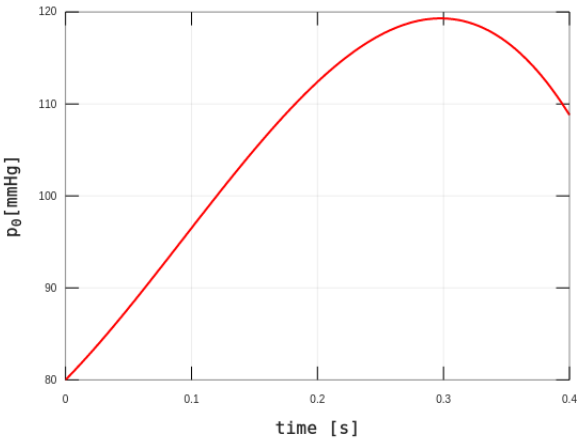

Figure 5.2: Physiological pressure waveform prescribed at the outflow section Σ^t_{out} of the ascending aorta. It represents a physiological aortic pressure profile in the systolic phase, plotted in the range (0, T_S]

the wall motion, reconstructed through the ALE approach, is extended to the immersed mitral valve surface.
Regarding the solution of the harmonic extension problem of the cine-MRI reconstructed displacement datum, a time interpolation through **splines** has been performed from the coarse grid, defined with the MRI time acquisition as time step ($\frac{1}{10}$ of the heartbeat, with pre-determined duration of 1 s), to the refined simulation time grid, with $\Delta t = 10^{-4}s$. An important advantage of exploiting splines for the time interpolation of the local displacements relies on the fact that they are C2-interpolating curves, therefore smooth functions. As a consequence, the interpolated displacements and the evaluated cavity volume (recalled in Figure 5.3) have a smooth behaviour, improving the accuracy of the simulation, compared to a linear time interpolation.
Moreover, in this work, in order to avoid the formation of severely stretched mesh cells, leading to distortion of the computational domain and generation of inaccurate peaks in the solution for a fixed time instant, we employ a computational smoothing strategy for the resolution of the Laplace problem for the harmonic extension of the displacement data.
In particular, we have enabled the **Jacobian-based stiffening** [92]: the factor $(J_0/J)^\chi$ is multiplied to the quantities integrated in the weak formulation of the lifting problem, where J_0 and χ are positive parameters and J is the jacobian of the map from the reference element to the ones in the physical space. In this way it is possible to account for stiffening elements that have a small jacobian, effectively penalizing excessively small

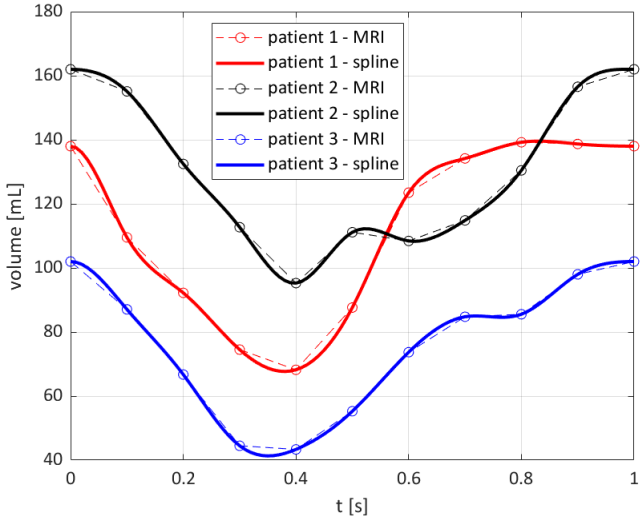

Figure 5.3: Time evolution of the volume of the reconstructed LV cavity

elements. This entails that small cells undergo milder deformations than greater ones, preserving the mesh quality from distortions that are common not only when large displacements are employed in the ALE framework, but also when there are mesh elements with very small angles, causing the reduction of the convergence of algorithms for the solution of the CFD problem and thus their accuracy.
Since the harmonic extension problem is solved on the initial mesh configuration Ω^0, the jacobian is not updated with the mesh motion.
Before presenting the results of the simulations, we report the values of the invariant physical parameters applied in the simulations, depicted in Table 5.1.

ρ	μ	R	ε	T_S	Δt	J_0
$[\frac{kg}{m^3}]$	[Pa·s]	$[\frac{kg}{ms}]$	m	s	s	m^3
$1.06 \cdot 10^3$	$3.5 \cdot 10^{-3}$	1000	0.002	0.4	10^{-4}	10^{-12}

Table 5.1: Values of the invariant physical parameters

The value of the half-thickness of the mitral valve surface ε has been imposed relying on the mesh size. In order to capture correctly the valve motion

in the fluid domain during the systolic phase, the value of ε needs to be sufficiently large. For this reason, since the average size of the hexahedral computational mesh is $h = 1\,mm$, with a local refinement to $h = 0.3\,mm$ in the region of the LVOT and the mitral valve, the half-thickness of the surface has been set to $\varepsilon = 0.002\,m$.

5.2 Results of the computational hemodynamics simulations

In this section we present the outcomes of the simulation of the CFD problem under prescribed motion, inspecting relevant markers for assessing possible obstructions induced by the blood flow due to HCM. For the sake of exposition we present the results relative to Patient 3 too (revising them with a new simulation), suffering from HOCM associated to SAM of the mitral valve, along with the outputs of the simulations for the two HCM patients. In this way it is possible to compare the behaviour of the indicators in presence of a less severe HCM and an obstructive HCM with the influence of the mitral valve on the blood flow.

5.2.1 Analysis of velocity patterns

Firstly the **velocity** field distribution is considered and inspected for each of the three patients at three different time steps during the systolic phase. In Figure 5.4 it is possible to analyze the evolution of velocity by highlighting it at significant times during the systolic phase.
As a first aspect, it is possible to denote that, as expected, the intensity of velocity is higher in the region of the computational domain where the aortic jet impacts, so in the LVOT.
Referring to the time instant where the velocity reaches its maximum as the *systolic peak*, it can be noticed also that the blood flow progression is different for the three patients. Indeed, at the early stages of the contraction phase, when blood starts to be ejected by the left ventricle, Patient 1 shows a quick blood acceleration and an intense aortic jet that impacts over the aortic root. Then a slow deceleration phase starts after $t = 0.1\,s$, that lasts until the end of systole. Instead, regarding Patient 2, the evolution of the blood flow is different, since it undergoes a slow acceleration and develops in the mid-systolic phase, reaching the systolic peak; in the final stages, instead of decelerating as for Patient 1, the blood velocity settles down approximately to the value of $1\,m/s$ (an end-systolic velocity plateau

is observed, referring to Figure 5.7).
Patient 3 blood flow develops later as in Patient 2 case, but it can be clearly noticed the effect of HOCM and SAM of the mitral valve on the blood flow, with a more intense aortic jet and higher blood velocity. In addition, especially for Patient 3 and barely for Patient 2, the impingement of the aortic jet on the superior aortic wall, downstream with respect to the Valsalva sinuses, is observed.

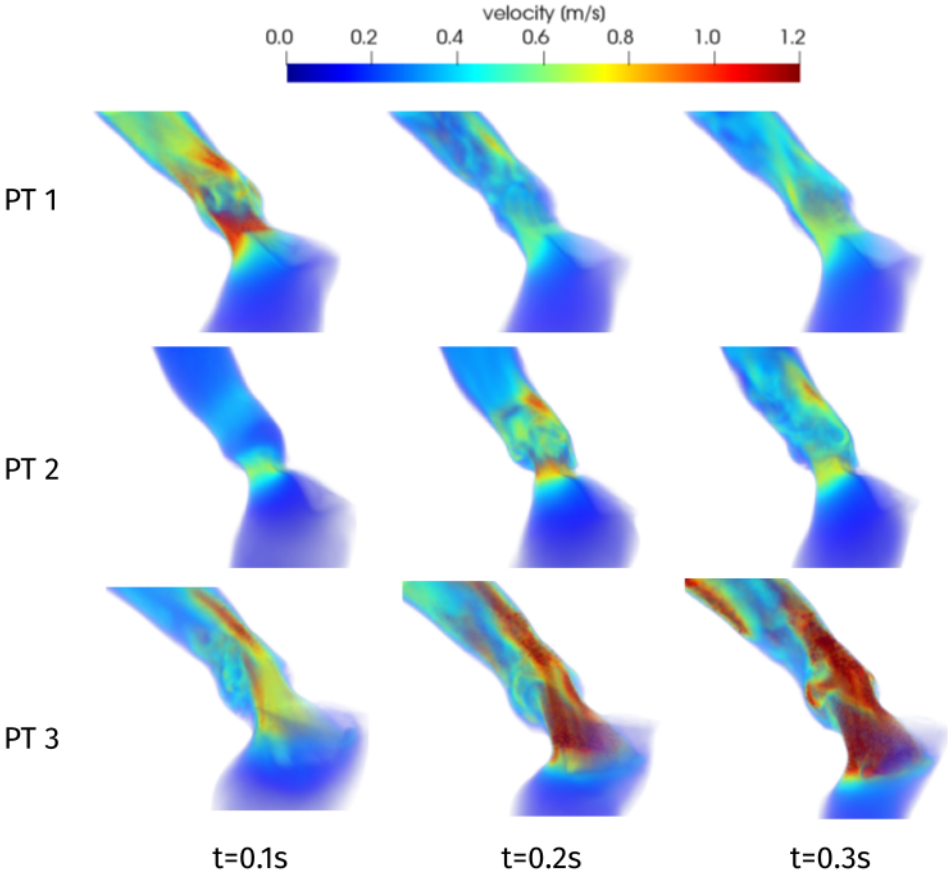

Figure 5.4: Time evolution of the velocity field in the region of LVOT and near the mitral valve for the three patients under investigation (visualized with ParaView) [www.paraview.org]

In terms of *peak systolic velocity* (PSV), we report a maximum velocity of $1.38\,m/s$ for Patient 1, attained at $t = 0.08\,s$, while the systolic peaks for the other two patients are reached afterwards ($t = 0.23\,s$ for Patient 2, $t = 0.22\,s$ for Patient 3), with maximum velocity of $1.31\,m/s$ and $2.2\,m/s$ respectively

for the second and the third case (Figure 5.7). In terms of clinical indications, Patient 1 and Patient 2 maximum velocity is slightly above the limits of the range of physiological values (1-1.2m/s), due to the mild obstruction induced in the flow by HCM. In the case of Patient 3 it is possible to detect the more severe consequences of the mitral leaflet systolic motion and the HOCM, since the attained maximum velocity is a pathological value.

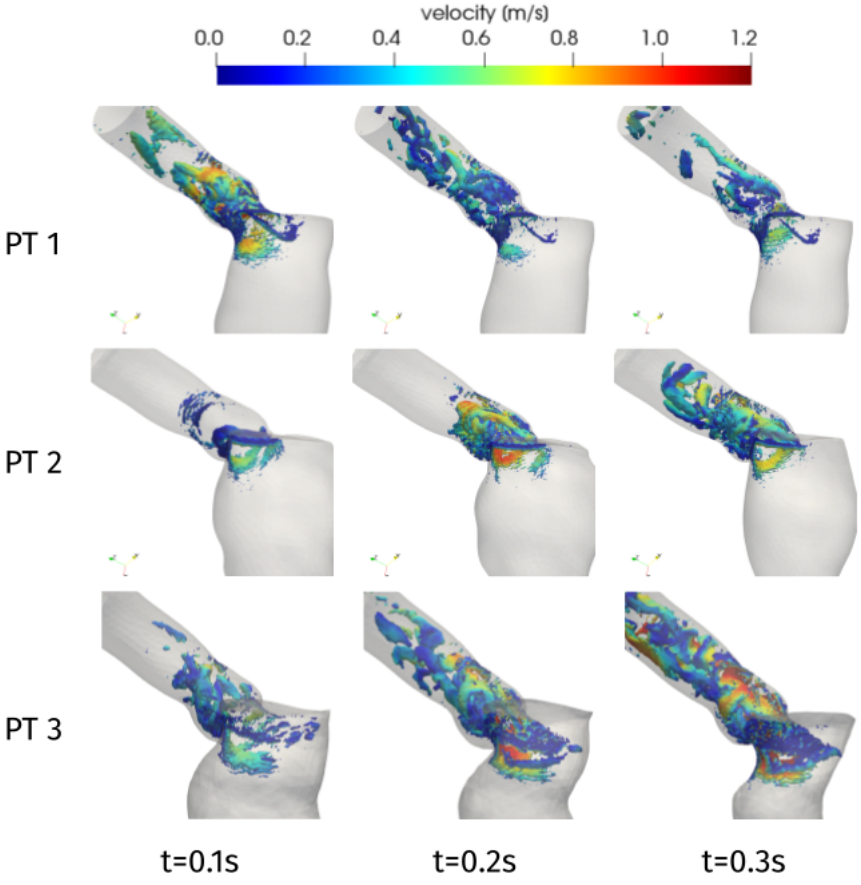

Figure 5.5: Q-criterion contours (10-log-spaced values for Q in 2.4·$[10^4, 10^6]s^{-1}$) colored by velocity magnitude at significant time during systole

Further information can be detected analyzing the **Q-criterion** representation (Figure 5.5), a method that can provide the visualization of coherent vortex structures in the flow, allowing to understand more significantly the flow-field. The definition of Q hinges upon the notion of velocity gradient tensor, that is decomposed into the symmetric part S, representing the

strain rate tensor, and the anti-symmetric part Ω, identifying the *vorticity tensor*, both defined as:

$$S = \frac{1}{2}(\nabla \mathbf{u} + \nabla \mathbf{u}^T), \qquad \Omega = \frac{1}{2}(\nabla \mathbf{u} - \nabla \mathbf{u}^T).$$

Q is obtained as the second invariant of the velocity gradient tensor:

$$Q = \frac{1}{2}(\|\Omega\|^2_{L^2} - \|S)\|^2_{L^2}), \tag{5.1}$$

that can give proper indications over the presence of turbulent structures in the fluid domain.
Indeed, positive values of Q are indicative of areas in the flow-field where the vorticity dominates and negative values of Q are indicative of strain rate or viscous stress dominated areas.
From the analysis of Figure 5.5, it is possible to observe for Patient 1 the advection of the vortex structures generated in the aortic root at the systolic peak ($t = 0.08\,s$) to the ascending aorta, where they progressively dissipate during the systolic phase. For what concerns Patient 2, and coherently Patient 3, the turbulent structures develop progressively throughout the entire systole, until they are present in the whole aortic tract. As expected, the vortex structures for the first two patients are less larger than Patient 3, that is consistent with the smaller peak systolic velocities reached in the LVOT. Indeed, Patient 3 is characterized by pathological high velocities in the aortic tract and in the LVOT, meaning that the flow is in distinct transition to turbulent regime (for good measure, a maximum Reynolds number $Re = 12000$ has been measured in the aortic root).
An interesting visualization that validates the remarks made for what concerns the blood flow progression and the evolution of the vortices is shown in Figure 5.6. In particular it is illustrated the development of the blood flow, that accelerates (slowly for Patient 2 and 3, at the early stages for Patient 1), along with the formation of the turbulent structures, until the systolic peak, after which the dissipation of the vortices in the ascending aorta and a deceleration at the end of the systole is experienced for each patient under investigation. In particular, from this visualization, the flow recirculation in the Valsalva sinuses is observed, causing the vortex shedding and, most of all, more intense Wall-Shear Stresses in the aortic root, as it will be explained in Section 5.2.2.

An important clinical marker employed for the assessment of the severity of HCM is the **duration of the HCM-induced obstruction**, a parameter

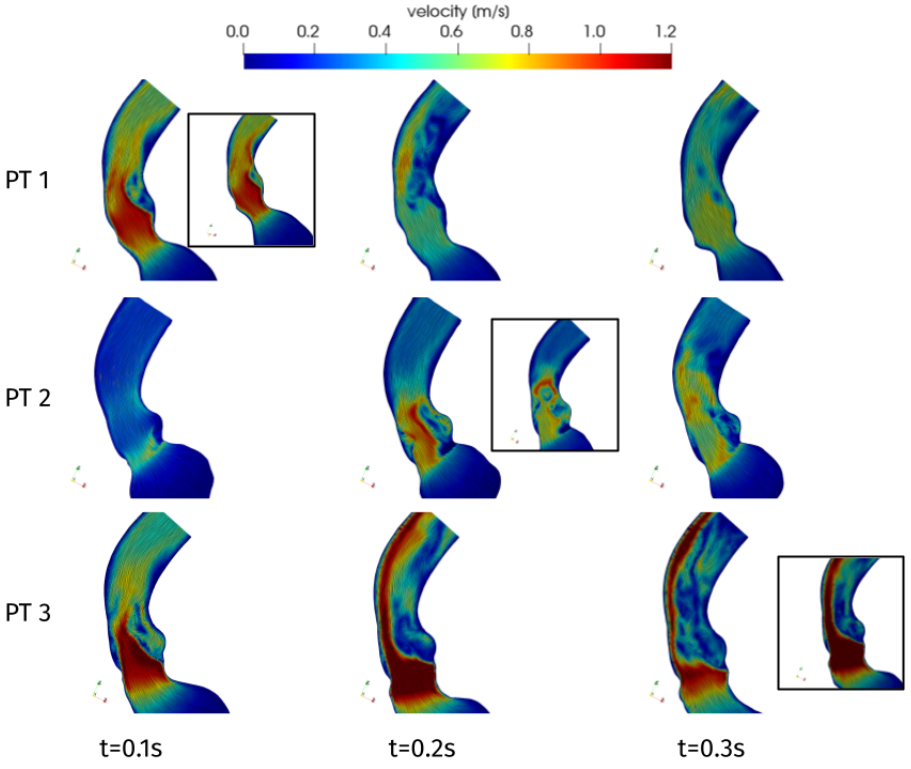

Figure 5.6: Velocity field distribution on a 2D longitudinal slice at significant times during systole; $In\ boxes:$ velocity field distribution on a 2D longitudinal slice at the systolic peak (Patient 1: $t = 0.08\,s$; Patient 2: $t = 0.23\,s$; Patient 3: $t = 0.22\,s$)

PATIENT	OBSTRUCTION START $[s]$	OBSTRUCTION END $[s]$	OBSTRUCTION DURATION $[s]$	THRESHOLD VALUE $U_{thr}\ [m/s]$
1	0.03	0.16	0.13	1.0
2	0.11	0.26	0.15	1.0
3	0.17	0.31	0.14	1.5

Table 5.2: Time evolution of the obstruction and plateau threshold velocity values for the identification of the obstruction time interval

that can be evaluated through the plot of the maximum value reached by the velocity field for each instant of the systolic phase (Figure 5.7).
After inspecting the behaviour of the velocity intensities for the three patients, it is possible to extrapolate for each case a time interval where the

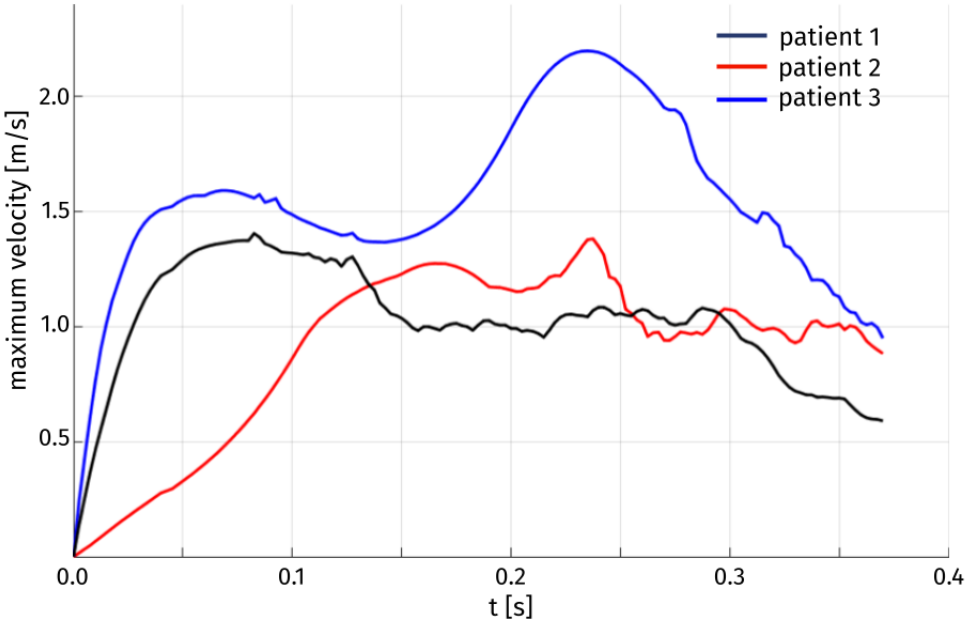

Figure 5.7: Time evolution of the maximum blood velocity for the three patients under investigation

velocity settles down, up to small variations, to a plateau intensity value that we have identified introducing the parameter U_{thr}. The latter represents, for each patient, a threshold value. Therefore, we can define the duration of the obstruction as the largest time interval in which the maximum velocity exceeds U_{thr}. Table 5.2 illustrates the computed results.
Analyzing the results from the table, all the three patients have an obstruction duration that interests slightly more than 30% of the systole (so, more than $0.12\,s$), that coincides with the threshold time duration provided by clinical guidelines to classify the obstruction as pathological. The described parameter is significantly relevant for cases like Patient 3, that is the only one to attain pathological peaks of velocity.
Regarding Patient 2, it is interesting to illustrate from Figure 5.8 (*Right*) the velocity field distribution in the systolic peak. An interesting aspect is that, although the peak systolic velocity (PSV) is attained, the aortic jet is milder and the blood flow is more intense downstream with respect to the Valsalva sinuses. In Section 5.2.2 a more detailed analysis is going to be per-

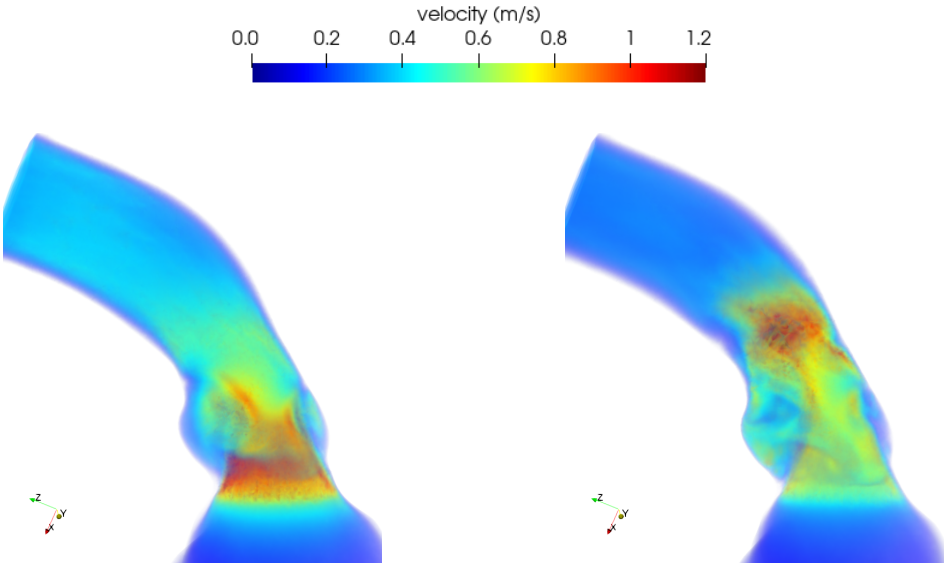

Figure 5.8: Patient 2 velocity distribution at the instant of maximum pressure gradient (Left, $t = 0.16\,s$) and at the systolic peak (Right, $t = 0.23\,s$)

formed, comparing the distribution of the velocity at the systolic peak with the corresponding one at the instant of maximum pressure gradient (Figure 5.8, *Left*), where higher velocities are encountered in the LVOT region.

5.2.2 Analysis of pressure field and gradients

The most important quantity that is inspected in clinical practice to assess the severity of the HCM-induced obstruction is the **intraventricular pressure gradient**, that identifies the pressure variation in the LVOT region. In this work we analyze the pressure difference $\Delta p(t, \mathbf{x}) = p(t, \mathbf{x}) - p_0(t, \mathbf{x})$, depicted in Figure 5.9, that represents the difference between the pressure field obtained from the numerical solution of the discretized CFD problem and the physiological aortic pressure waveform, assigned as outflow condition at the distal section of the ascending aorta (so, as a consequence, in the aortic tract, the more Δp is close to 0, the more the behaviour is physiological).
From the visualization of Figure 5.9 we can notice relevant pressure gradients in the LVOT region and, barely, in the Valsalva sinuses, whilst in the other portions of the computational domain the pressure distribution is uniform. For what concerns Patient 1, during the systolic phase, the overall pressure gradient lays in the range $[-3, 3]$ $mmHg$, whereas for Patient 2, as

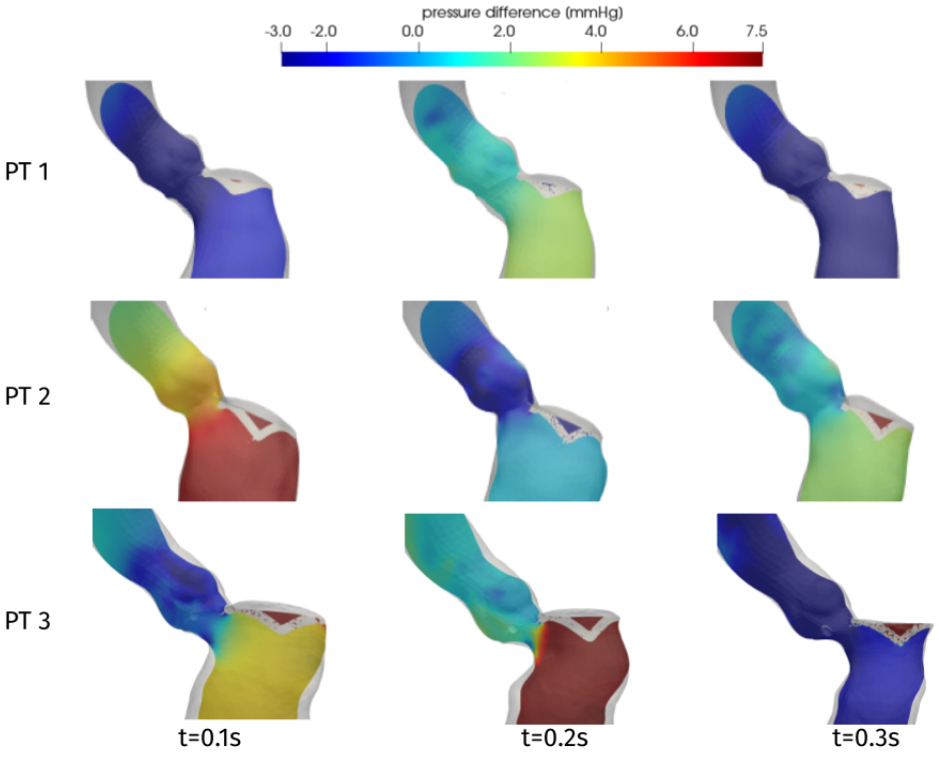

Figure 5.9: Distribution of pressure difference $\Delta p = p - p_0$ on a longitudinal slice at significant times during systole

for Patient 3, it is more than double. The time evolution of the pressure difference Δp, for each patient, is characterized by variability at different stages of the systolic phase, as observed for the time-dependent displacements and left ventricle cavity volume in Section 3.5.4.
The variability of the pressure gradient distribution can be observed also in Figure 5.10, where the behaviour of the jump between the averaged ventricular pressure p_{LV} minus the averaged aortic root one p_{AO} is highlighted during the whole systole.
Although the plot has a fluctuating trend, affecting the smoothness of the representation, the time evolution of the pressure jump in Figure 5.10 denotes for Patient 1 and 3 the same progression of the blood flow that can be depicted analyzing the time evolution of the velocity field in Figure 5.7: we still observe the early intense aortic jet for Patient 1, causing a blood acceleration and leading to the attainment of the systolic peak at $t = 0.08\,s$, consistent with the higher pressure gradient at the early stages. The same remark holds true for Patient 3, with the blood flow development at the

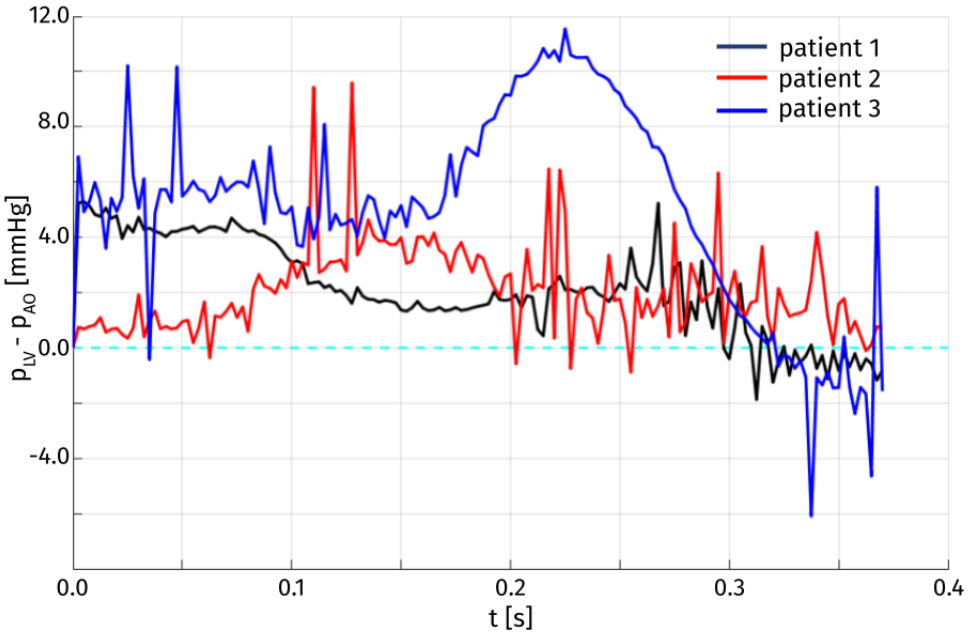

Figure 5.10: Time evolution of the pressure gradient $p_{LV} - p_{AO}$ for the three patients under investigation

middle-stage of the systolic phase, attaining relevant values of pressure gradient, higher than $10\,mmHg$, at the systolic peak. Instead for Patient 2, the plot reveals an important aspect: the systolic peak and the maximum pressure gradient time instant do not coincide. Indeed, as pointed out previously, the former is achieved in late systole, at $t = 0.23\,s$, while the latter is attained earlier, at $t = 0.16\,s$.
An explanation can be found in Figure 5.8, that highlights the velocity distribution of Patient 2 in the two aforementioned time instants. The pressure jump is higher when the aortic jet is more intense and the velocity is higher in the LVOT region. Nevertheless, the systolic peak is attained afterwards, when the systolic jet is milder, but the blood flow velocity attains its maximum downstream in the ascending aorta, beyond the Valsalva sinuses.
A final aspect to be mentioned for what concerns Figure 5.10, that validates the applied method, is the behaviour of the pressure jump at the end of the systole: each patient experiences a decrease of $p_{LV} - p_{AO}$, attaining negative values, in accordance with the the time evolution of the physio-

logical ventricular and aortic waveforms, which can be depicted from the Wiggers diagram. Indeed, in this phase, the left ventricle is close to reach its minimum value of volume, with the ventricular pressure that is going to exceed the aortic one, due to inflation of blood, and the diastolic phase that is starting soon, with the ventricular filling.

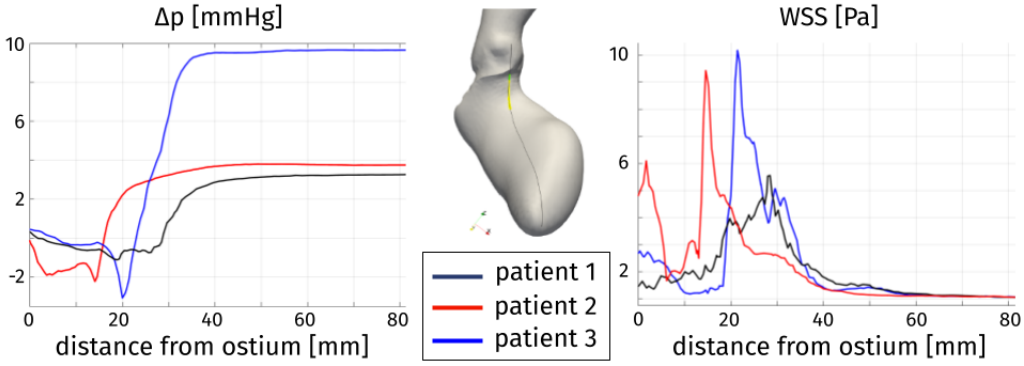

Figure 5.11: Distribution of the intraventricular pressure gradient $\Delta p = p - p_0$ with respect to Valsalva sinuses $(Left)$ and Wall-Shear Stress $(Right)$ along a line on the septum $(Middle)$ at the instant of maximum pressure jump (Patient 1: $t = 0.08\,s$; Patient 2: $t = 0.16\,s$; Patient 3: $t = 0.22\,s$)

The following post-processing analysis that is performed provides preliminary quantitative indications, supporting clinical-decision for the treatment of HCM. Indeed, for the most severe cases, when the induced obstruction causes a pathological evolution of the blood flow, a portion of the myocardium is resected through septal myectomy. The aim, with the following analysis, is to assess the severity of the obstruction, to quantify its location and extension and whether the patient needs or not a surgical treatment.
For this reason, in Figure 5.11 a plot of the pressure difference Δp along a line on the interventricular septum is presented, starting from the Valsalva sinuses ($distance from ostium = 0\,mm$) and ending on the left ventricle apex. The three plotted curves represent the spatial evolution of Δp at a fixed time instant, identified as the time in which the highest pressure gradient is reached for each patient under investigation.
The general behaviour of the curves is that the pressure difference has a

small decay and, immediately after, a relevant increase, reaching, then, a steady state, with maximum in the ventricular region. Therefore only in the LVOT and at the aortic orifice the pressure gradient develops. As a consequence it is possible to locate the HCM-induced obstruction: regarding Patient 1, it is within the LVOT (as for Patient 3), while for Patient 2 the aortic annulus represents the obstacle to the blood flow.
Both Patient 1 and Patient 2 are characterized by lower pressure gradients than the reported physiological limits ($< 5\,mm$) [44], while Patient 3, that is affected by more severe HCM associated to SAM of the mitral valve, experiences an intraventricular pressure gradient ($max(\Delta p) - min(\Delta p) = 12\,mmHg$) that exceeds significantly the physiological limit. In particular, the pressure drop in the subaortic portion can induce a Venturi Effect that can represent a cause of SAM of the mitral valve. Less severe cases as Patient 1 and 2 do not undergo this process.

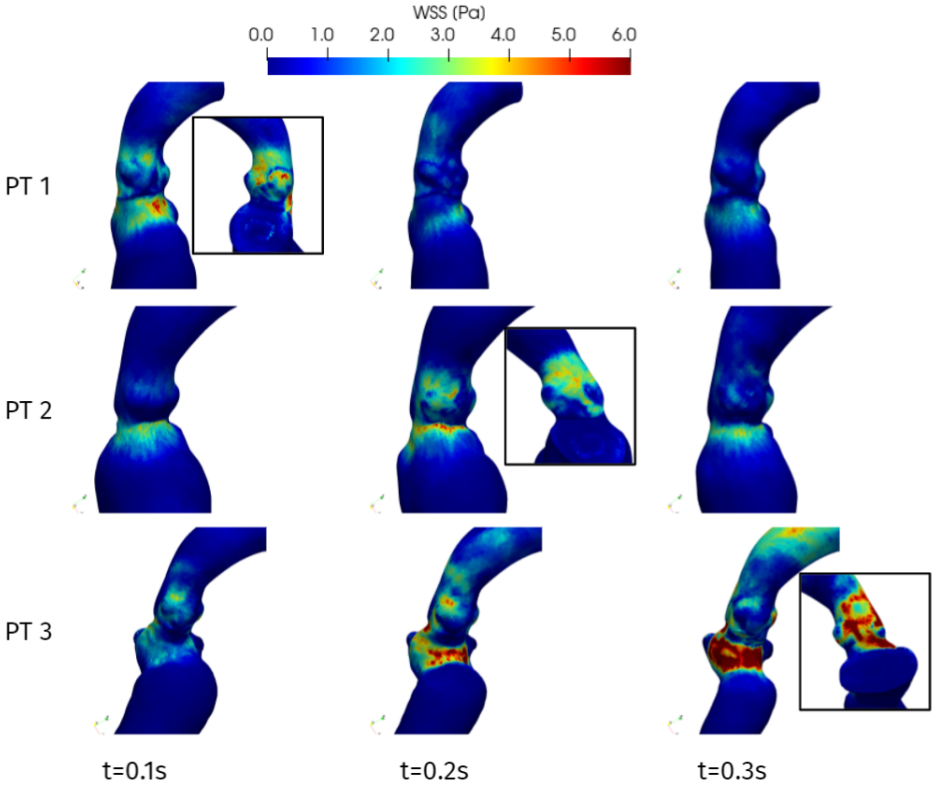

Figure 5.12: Wall-Shear Stress distribution, visualized from the interventricular septum, at significant time during systole. In the boxes: Wall-Shear Stress distribution, visualized from the atrial side at the systolic peak (Patient 1: $t = 0.08\,s$; Patient 2: $t = 0.23\,s$; Patient 3: $t = 0.22\,s$)

In the right plot of Figure 5.11 the **Wall-Shear Stress** (WSS) spatial distribution along the line on the septum, for each patient, is represented at the time instant corresponding to the maximum pressure gradient. A remarkable aspect to be mentioned is the fact that in these instants, for each patient, the WSSs reach their maximum intensity (so, within the LVOT for Patient 1 and 3 and at the aortic annulus for Patient 2). This is a confirm with respect to the results presented in Figure 5.12, which shows the WSS distribution on the ventricular and aortic wall at the systolic peak of each patient (from the septum): higher values of WSS are observed at the septal wall of the LVOT, due to the effect of the hypertrophic septum deviating the blood flow (that is coherent with the remarks made above regarding the obstruction observed analyzing the velocity field and the pressure gradient distribution).
In terms of possible surgical treatment of the pathology, the ESC guidelines refer a threshold value of $50\,mmHg$ for the LVOT pressure gradient peak [44], above which it could be necessary to proceed with the a surgery, in order to resect the portions of the interventricular septum in the medio-basal region that cause the flow obstruction. The plot of the pressure gradients and of the WSSs from Figure 5.11, in this sense, provides useful practical indications: for all the three patients (most of all Patient 1 and 2, who do not experience a HCM-induced flow obstruction), the severity level of the pathology should not require a surgical treatment, due to the acceptable pressure gradient peaks. However, the plot is clinically relevant since it highlights the sites where the a septal myectomy could be pursued (in case of more severe HOCM patients), which are identified as the areas where the pressure decay and the sudden increase are observed: the results are consistent with the common surgical procedures, since the aforementioned regions are commonly targeted by surgeons for the design of a myectomy.
For what concerns Figure 5.12, for all the patients, high values of WSS are detected in the first tract of the aortic root, due to the flow recirculation that is encountered in the Valsalva sinuses (Figure 5.6).
Furthermore, we can also observe high WSS intensity in the ascending aorta at the systolic peak. This aspect is relevant from the clinical point of view since the impingement of the systolic jet can cause damages to the aortic wall, with possible formation of an aneurysm [91].
A final consideration that can be made is associated to Patient 1: WSS are non-negligible on the septal wall throughout the systolic phase. Since the WSS are related with velocity gradients, the outcome is coherent with the representation of the vortex structures in Figure 5.5, that dissipate in the ascending aorta, but they persist in the septal portion.

Chapter 6

Conclusions

In this work, an image-based computational hemodynamics study has been pursued, in order to assess the severity of the systolic Hypertrophic Cardiomyopathy-induced obstruction. We have proposed a reconstruction pipeline in the image processing phase, hinging upon standard cine-MRI data routinely acquired in clinical practice. With the proposed procedure, artificial enriched volumetric images have been generated. Afterwards, these images have been exploited to reconstruct the patient-specific geometry and the ventricular and aortic motion throughout the whole heartbeat. The resulting MRI displacement datum has been employed as boundary conditions for a Computational Fluid Dynamics Study of cardiac hemodynamics, based on Navier-Stokes Equations in a unique framework that includes two different numerical procedures: the ALE approach for the moving domain and the RIIS resistive method, to model the immersed mitral valve surface in the computational domain.
Finally, in order to assess the HCM effects on the hemodynamics of the patients under investigation, we inspect geometrical indicators as the LV cavity volume, the displacement field distribution and clinical bio-markers such as EDV, ESV and EF, along with hemodynamics parameters as the velocity distribution, the pressure field and gradient and the Wall-Shear Stress intensity.

6.1 Clinical impact of the results

In the present section, we point out how our results allow to assess the hemodynamical effects of HCM to the global cardiac function and may support clinical decision-making and the design of the treatment.
The imaging results of the reconstruction pipeline reveal the remarkable

variability among different HCM patients, related to the left ventricle geometry and motion.
Non-homogeneous ventricular displacements can be observed, such as regions of hypokinesis. This affects the contraction and the ventricular cavity volume. By accurate reconstruction of the geometry shape and cavity, we can measure the time evolution of the volume without resorting to the approximation of the LV as ellipsoid [93].
For what concerns the analysis of the hemodynamics outputs of interest, the systolic obstruction of the flow due to HCM can be assessed quantifying its duration and its spatial extension. In terms of time span, for each considered patient the obstruction interests slight more than the 30% of the duration of the systole. Since this duration is highlighted as a risk factor in clinical guidelines, further investigation and monitoring are necessary.
Regarding pressure gradient distribution, a higher intensity in the LVOT and in Valsalva sinuses is observed in the cases with more severe obstruction, leading to more intense systolic jets through the aortic orifice.
Analyzing the behaviour of the pressure difference Δp on the interventricular septum, we can conclude that:

- Regarding Patient 1, the hypertrophic cardiomyopathy does not cause a systolic obstruction due to low pressure gradient, even if the septal hypokinesis in the medio-basal region, entailing inhomogeneous displacements, leads to a slightly higher peak systolic velocity and an ejection fraction just above the limit value of 50% [44].

- For what concerns Patient 2, also in this case the low pressure gradient, developed in the aortic annulus, implies that the HCM does not directly induce an obstruction. Nevertheless, we can still point out that the large left ventricle cavity volume and the distributed hypokinesis affect the blood flow, implying a low ejection fraction.

In this work it has been also possible to compare two HCM patients, without systolic obstruction, with a case that fits the definitions of HOCM, with intense aortic jet and remarkable pressure gradient in the LVOT region, causing a Venturi Effect that may have induced the development of a SAM of the mitral valve.

6.2 Limitations and future developments

The computational pipeline relies on considering a **physiological** mitral valve and neglecting the aortic one. For this reason, an accurate reconstruction of both of them, including possible patient-specific abnormal characteristics of the mitral and aortic valve, would improve the accuracy of the mathematical model.
Furthermore, the reconstruction pipeline could be extended by considering the valves opening and closing and reconstructing the left atrium, with the aim of modeling not only a single systole, but a full heartbeat or even multiple heartbeats. In the latter case, the model may not only assess the effect of HCM on the whole cardiac function, but even predict further developments of the pathology, especially if coupled with a heart remodeling model.
A final limitation relies on the high computational costs and efforts for the analysis of one patient.
In order to provide indications in keeping with the times of clinical decision-making, a real-time numerical simulation approach may be developed.
This procedure could rely on the following key points:

- **automatization of the reconstruction procedure**, in order to provide real-time measurements;
- **inclusion of a data assimilation strategy**: the real-time data may be integrated in the "offline" model through a resolution of an inverse problem (through, for instance, machine learning methods along with physics-based models);
- **improvement of the computational performance**: the application of a reduced-order method (ROM) may decrease the computational costs, so that the model may achieve real-time capabilites

For further reliability of clinical assessment through the results, an enlarged set of patients may be employed, in order to include interpatients variability.

References

[1] H. Gao et al. “A coupled mitral valve-left ventricle model with fluid-structure interaction”. In: Medical Engineering Physics 47 (2017), pp. 128–136.
[2] I. Fumagalli et al. An Image-based Computational Hemodynamics Study of the Systolic Anterior Motion of the Mitral Valve. Mox Report. 2020.
[3] K. Kunzelman, D.R. Einstein, and R. Cochran. “Fluid-structure interaction models of the mitral valve function in normal and pathological states”. In: Philosophical Transactions of the Royal Societies B: Biological Sciences 362.1484 (2007), pp. 1393–1406.
[4] L. Feng et al. “Analysis of a coupled fluid-structure interaction model of the left atrium and mitral valve”. In: International Journal for Numerical Methods in Biomedical Engineering 35.11 (2019).
[5] X. Ma et al. “Image-based fluid-structure interaction model of the human mitral valve”. In: Computers Fluids 47 (2017), pp. 128–136.
[6] B. Su et al. “Numerical simulation of patient-specific left ventricular model with both mitral and aortic valves by FSI approach”. In: Journal of Biomechanics 113.2 (2014), pp. 474–482.
[7] T. Lassila et al. “Simulation of the left ventricle fluid dynamics with mitral regurgitation from magnetic resonance images with fictitious elastic structure regularization”. In: arXiv preprint arXiv:170703998 (2017).
[8] A.D. Kaiser, D.M. McQueen, and C.S. Peskin. “Modeling the mitral valve”. In: International Journal for Numerical Methods in Biomedical Engineering 35.11 (2019).
[9] J. Donea, S. Giuliani, and J.P. Halleux. “An arbitrary Lagrangian-Eulerian finite element method for transient dynamic fluid-structure interactions”. In: Computer Methods in Applied Mechanics and Engineering 33.1-3 (1982), pp. 689–723.
[10] L. Dedè, F. Menghini, and A. Quarteroni. ”Computational fluid dynamics of blood flow in an idealized left human heart”. In: International Journal for Numerical Methods in Biomedical Engineering (2019).

[11] A. Tagliabue, L. Dedè, and A. Quarteroni. "Complex blood flow patterns in an idealized left ventricle: a numerical study". In: Chaos: An Interdisciplinary Journal of Nonlinear Science 27.9 (2017).
[12] A. Masci et al. "A proof of concept for computational fluid dynamics analysis of the left atrium in atrial fibrillation on a patient-specific basis". In: Journal of Biomedical Engineering 142.1 (2020).
[13] A. This et al. "A pipeline for image based intracardiac CFD modeling and application to the evaluation of the PISA method". In: Computer Methods in Applied Mechanics and Engineering (2019).
[14] A. This. "Image/model fusion for the quantification of mitral regurgitation severity". PhD Thesis. Universitè Pierre et Marie Curie, 2019.
[15] Federico Canè, Matteo Selmi, Gianluca De Santis, Alberto Redaelli, Patrick Segers, Joris Degroote, Mixed impact of torsion on LV hemodynamics: A CFD study based on the Chimera technique, Computers in Biology and Medicine, Volume 112, 2019, 103363, ISSN 0010-4825.
[16] B. Su et al. "Patient-specific blood flows and vortex formations in patients with hypertrophic cardiomyopathy using computational fluid dynamics". In: 2014 IEEE Conference on Biomedical Engineering and Sciences (IECBES). 2014, pp. 276–280.
[17] Simulations of Hypertrophic Obstructive Cardiomyopathy (HOCM) in a Human Heart Left Ventricle using ANSYS/CFX/Fluent, May 2014, DOI:10.13140/2.1.4468.5127, Conference: ANSYS USers Conference, SantaClara, Project: CFD of Human Heart, Authors: Vladimir Kudriavtsev
[18] B. Su et al. "Cardiac MRI based numerical modeling of left ventricular fluid dynamics with mitral valve incorporated". In: Journal of Biomechanics 49.7 (2016), pp. 1199–1205.
[19] B. Su et al. "Patient-specific blood flows and vortex formations in patients with hypertrophic cardiomyopathy using computational fluid dynamics". In: 2014 IEEE Conference on Biomedical Engineering and Sciences (IECBES). 2014, pp. 276–280.
[20] A. Nardi et al. "Hypertrophic Cardiomyopathy Treatment – A Numerical Study". In: Computer Methods, Imaging and Visualization in Biomechanics and Biomedical Engineering. Ed. by Gerard A. Ateshian, Kristin M. Myers, and João Manuel R. S. Tavares. Springer International Publishing, 2020, pp. 24– 35.
[21] M. Fedele et al. "A patient-specific aortic valve model based on moving resistive immersed implicit surfaces". In: Biomechanics and Modeling in Mechanobiology 16.5 (2017), pp. 1779–1803.
[22] M. Astorino et al. "A robust and efficient valve model based on resistive immersed surfaces". In: International Journal for Numerical Methods

in Biomedical Engineering 28.9 (2012), pp. 937–959.
[23] M.A. Fernández, J.F. Gerbeau, and V. Martin. “Numerical simulation of blood flows through a porous interface”. In: ESAIM: Mathematical Modelling and Numerical Analysis 42.6 (2008), pp. 961–990.
[24] A. Quarteroni , A. Manzoni and C. Vergara ”The cardiovascular system: Mathematical modelling, numerical algorithms and clinical applications”. In: Acta Numerica (2017), pp. 365–590, doi:10.1017/S0962492917000046
[25] L. Formaggia, A. Quarteroni, A. Veneziani ”Cardiovascular Mathematics” - ”Modeling and simulation of the circulatory system”
[26] ”Types of Cardiomyopathy”. NHLBI. 22 June 2016
[27] https://www.healio.com/cardiology/learn-the-heart/cardiology-review/topic-reviews/hypertrophic-obstructive-cardiomyopathy-hocm
[28] Berger A. Magnetic resonance imaging. BMJ. 2002; 324(7328):35
[29] Kramer CM, Barkhausen J, Flamm SD, Kim RJ, Nagel E; Society for Cardiovascular Magnetic Resonance Board of Trustees Task Force on Standardized Protocols. Standardized cardiovascular magnetic resonance imaging (CMR) protocols, society for cardiovascular magnetic resonance: board of trustees task force on standardized protocols. J Cardiovasc Magn Reson. 2008;10(1):35. Published 2008 Jul 7. doi:10.1186/1532-429X-10-35
[30] Francesca Nicolo’, Antonio Lio, Marina Comisso, Romina Pantanella, Roberto Scrofani and Francesco Musumeci, Surgical Treatment of Hypertrophic Obstructive Cardiomyopathy, Intechopen, June 7th 2019
DOI: 10.5772/intechopen.86816
[31] Perktold K, Thurner E, Kenner T. Flow and stress characteristics in rigid walled and compliant carotid artery bifurcation models. Med Biol Eng Comput. 1994 Jan;32(1):19-26. doi: 10.1007/BF02512474. PMID: 8182957.
[32] Taylor C., Hughes T., Zarins C., Computational Investigations in Vascular Disease Computers in Physics 10, 224 (1996)
[33] L. Formaggia, A. Quarteroni, A. Veneziani ”Cardiovascular Mathematics” - ”Modeling and simulation of the circulatory system”
[34] Robertson, Anne Sequeira, Adélia Owens, Robert. (2010). Rheological models for blood. 10.1007/978-88-470-1152-6_6.
[35] Fasano, A., Santos, R.F., Sequeira, A. (2012). Blood coagulation: A puzzle for biologists, a maze for mathematicians.
[36] Barnard AC, Hunt WA, Timlake WP, Varley E. A theory of fluid flow in compliant tubes. Biophys J. 1966;6(6):717-724. doi:10.1016/S0006-3495(66)86690-0
[37] T. Hughes (1974), A study of the one-dimensional theory of arterial pulse propaga- tion. PhD thesis, University of California, Berkeley.
[38] T. Hughes and J. Lubliner (1973), ‘On the one-dimensional theory of

blood flow in the larger vessels', Math. Biosci. 18, 161–170.
[39] P. Colli Franzone, L. Pavarino and S. Scacchi (2014), Mathematical Cardiac Electro- physiology, Springer.
[40] R. FitzHugh (1961), 'Impulses and physiological states in theoretical models of nerve membrane', Biophys. J. 1, 445–466.
[41] A. L. Hodgkin, A. F. Huxley "A quantitative description of membrane current and its application to conduction and excitation in nerve" In: J Physiol. 1952 Aug 28; 117(4): 500–544.
[42] Nash MP, Panfilov AV. Electromechanical model of excitable tissue to study reentrant cardiac arrhythmias. Prog Biophys Mol Biol. 2004 Jun-Jul;85(2-3):501-22.
[43] Land S, Niederer SA, Aronsen JM, et al. An analysis of deformation-dependent electromechanical coupling in the mouse heart. J Physiol. 2012; 590(18):4553-4569.
[44] P. Elliott, A. Anastasakis, M. Borger, M. Borggrefe, F. Cecchi, P. Charron, A. Hagege, A. Lafont, G. Limongelli, H. Mahrholdt, W. McKenna, J. Mogensen, P. Nihoyannopoulos, S. Nistri, P. Piepe, B. Pieske, C. Rapezzi andF. Rutten, ≪ESC guidelines on diagnosisand management of hypertrophic cardiomyopathy: The task force for the diagnosis and management of hypertrophic cardiomyopathy of the European Society of Cardiology (ESC),≫ European Heart Journal, vol. 35, n. 39, 2014
[45] V. Meschini, R. Mittal and R. Verzicco, ≪Systolic anterior motion in hypertrophic cardiomyopathy: a fluid-structure interaction computational model,≫ Theoretical and Computational Fluid Dynamics, vol. 35, pp. 381-396, 2021
[46] L. Deng, X. Huang, C. Yang, B. Lyu, F. Duan, D. Tang andY. Song, ≪Numerical simulation study on systolic anterior motion of the mitral valve inhypertrophic obstructive cardiomyopathy,≫ International Journal of Cardiology, vol. 266, 2018
[47] M. D'Elia, L. Mirabella, T. Passerini, M. Perego, M. Piccinelli, C. VergaraandA. Veneziani,Applications of variational data assimilation in computational hemodynamics, in "Modeling of Physiological Flows", D. Ambrosi, A. Quarteroni, G. Rozza editors, Springer,2011.
[48] Gareth Matthews David Chambers Christopher Huang. Basic Physiology for Anaesthetists. 1st ed. Cambridge University Press, 2015.
[49] Bansal, Manish Kasliwal, Ravi. (2013). How do I do it? Speckle-tracking echocardiography. Indian heart journal. 65. 117-23. 10.1016/j.ihj.2012.12.004.
[50] I. Wolf, M. Vetter, I. Wegner, T. Böttger, M. Nolden, M. Schöbinger, M. Hastenteufel, K. T. andH.-P. Meinzer, ≪The medical imaging interaction

toolkit≫ Medical Image Analysis, vol. 9, n. 6, 2005
[51] M. Nolden, S. Zelzer, A. Seitel, D. Wald, M. Müller, A.Franz, D. Maleike, M. Fangerau, M. Baumhauer,L. Maier-Hein, K. Maier-Hein, H. Meinzer andI. Wolf, ≪The medical imaging interaction toolkit: challenges and advances,≫ International Journal of Computer Assisted Radiology and Surgery, vol. 8, 2013
[52] L. Antiga, M. Piccinelli, L. Botti, B. Ene-Iordache, A. Remuzzi and D.Steinman, ≪An image-based modeling framework for patient-specific computational hemodynamics,≫ Medical Biological Engineering Computing, vol. 46, 2008
[53] Zygote Media Group, Inc., Zygote Solid 3D Heart Generation II Development Report, 2014
[54] M. Fedele and A. Quarteroni, ≪Polygonal surface processing and mesh generation tools for the numerical simulation of the cardiac function,≫ International Journal for Numerical Methods in Biomedical Engineering, vol. e3435, 2021
[55] P.J. Besl and N.D. McKay. "Method for registration of 3-d shapes". In: Sen- sor fusion IV: control paradigms and data structures, International Society for Optics and Photonics 1611 (1992), pp. 586–606.
[56] L. Antiga, B. Ene-Iordache, and A. Remuzzi. "Computational geometry for patient-specific reconstruction and meshing of blood vessels from MR and CT angiography". In: IEEE Transactions on Medical Imaging 22.5 (2003), pp. 674–684.
[57] G. Pase, "An Image-based Computational Hemodynamic Study of Hypertrophic Cardiomyopathy", Master Thesis, Supervisors: L. O. Müller, C. Vergara; Assistant Supervisors: M. Fedele, I. Fumagalli; Department of Mathematics, Università degli Studi di Trento, a.a. 2019-2020
[58] R. Cheng, Y.G. Lai, K.B. Chandran, Three-dimensional fluid-structure interaction simulation of bileaflet mechanical heart valve flow dynamics, Ann. Biomed. Eng. 32 (11) (2004) 1471–1483.
[59] Y.S. Morsi, W.W. Yang, C.S. Wong, S. Das, Transient fluid–structure coupling for simulation of a trileaflet heart valve using weak coupling, J. Artif. Organs 10 (2) (2007) 96–103.
[60] D.M. Espino, D.E. Shepherd, D.W. Hukins, Evaluation of a transient, simultaneous, arbitrary Lagrange–Euler based multi-physics method for simulating the mitral heart valve, Comput. Methods Biomech. Biomed. Eng. 17 (4) (2014) 450–458.
[61] S. Basting, A. Quaini, S. Čanić, R. Glowinski, Extended ALE method for fluid– structure interaction problems with large structural displacements, J. Comput. Phys. 331 (2017) 312–336.

[62] A. Massing, M. Larson, A. Logg, M. Rognes, A nitsche-based cut finite ele- ment method for a fluid-structure interaction problem, Commun. Appl. Math. Comput. Sci. 10 (2) (2015) 97–120.
[63] F. Alauzet, B. Fabrèges, M.A. Fernández, M. Landajuela, Nitsche-XFEM for the coupling of an incompressible fluid with immersed thin-walled structures, Comput. Methods Appl. Mech. Engrg. 301 (2016) 300–335.
[64] S. Zonca, C. Vergara, L. Formaggia, An unfitted formulation for the interaction of an incompressible fluid with a thick structure via an XFEM/DG approach, SIAM J. Sci. Comput. 40 (1) (2018) B59–B84.
[65] L. Boilevin-Kayl, M.A. Fernández, J.-F. Gerbeau, Numerical methods for immersed FSI with thin-walled structures, Comput. Fluids 179 (2019) 744–763
[66] L. Ge, H.-L. Leo, F. Sotiropoulos, A.P. Yoganathan, Flow in a mechanical bileaflet heart valve at laminar and near-peak systole flow rates: CFD simulations and experiments, J. Biomech. Eng. 127 (5)
(2005) 782–797. [67] T.B. Le, F. Sotiropoulos, Fluid–structure interaction of an aortic heart valve prosthesis driven by an animated anatomic left ventricle, J. Comput. Phys. 244 (2013) 41–62.
[68] J. De Hart, G. Peters, P. Schreurs, F. Baaijens, A three-dimensional computa- tional analysis of fluid–structure interaction in the aortic valve, J. Biomech. 36 (1) (2003) 103–112.
[69] Z. Yu, A DLM/FD method for fluid/flexible-body interactions, J. Comput. Phys. 207 (1) (2005) 1–27.
[70] R. van Loon, P.D. Anderson, F.N. van de Vosse, A fluid–structure interaction method with solid-rigid contact for heart valve dynamics, J. Comput. Phys. 217 (2) (2006) 806–823.
[71] N.D. Dos Santos, J.-F. Gerbeau, J.-F. Bourgat, A partitioned fluid–structure algorithm for elastic thin valves with contact, Comput. Methods Appl. Mech. Engrg. 197 (19–20) (2008) 1750–1761.
[72] M. Astorino, J.-F. Gerbeau, O. Pantz, K.-F. Traore, Fluid–structure interaction and multi-body contact: application to aortic valves, Comput. Methods Appl. Mech. Engrg. 198 (45–46) (2009) 3603–3612.
[73] B.E. Griffith, X. Luo, D.M. McQueen, C.S. Peskin, Simulating the fluid dynamics of natural and prosthetic heart valves using the immersed boundary method, Int. J. Appl. Mech. 1 (01) (2009) 137–177.
[74] I. Borazjani, L. Ge, F. Sotiropoulos, High-resolution fluid–structure interaction simulations of flow through a bi-leaflet mechanical heart valve in an anatomic aorta, Ann. Biomed. Eng. 38 (2) (2010) 326–344.
[75] L. Ge, F. Sotiropoulos, Direction and magnitude of blood flow shear stresses on the leaflets of aortic valves: is there a link with valve calcifica-

tion?, J. Biomech. Eng. 132 (1) (2010) 014505.
[76] B.E. Griffith, Immersed boundary model of aortic heart valve dynamics with physiological driving and loading conditions, Int. J. Numer. Methods Biomed. Eng. 28 (3) (2012) 317–345.
[77] M.-C. Hsu, D. Kamensky, Y. Bazilevs, M.S. Sacks, T.J. Hughes, Fluid–structure interaction analysis of bioprosthetic heart valves: significance of arterial wall deformation, Comput. Mech. 54 (4) (2014) 1055–1071.
[78] D. Kamensky, M.-C. Hsu, D. Schillinger, J.A. Evans, A. Aggarwal, Y. Bazilevs, M.S. Sacks, T.J. Hughes, An immersogeometric variational framework for fluid–structure interaction: Application to bioprosthetic heart valves, Comput. Methods Appl. Mech. Engrg. 284 (2015) 1005–1053.
[79] L. Boilevin-Kayl, M.A. Fernández, J.-F. Gerbeau, A loosely coupled scheme for fictitious domain approximations of fluid-structure interaction problems with immersed thin-walled structures, SIAM J. Sci. Comput. 41 (2) (2019) B351–B374.
[80] M.C. Wu, R. Zakerzadeh, D. Kamensky, J. Kiendl, M.S. Sacks, M.-C. Hsu, An anisotropic constitutive model for immersogeometric fluid–structure interaction analysis of bioprosthetic heart valves, J. Biomech. 74 (2018) 23–31.
[81] C. Wiggers, Modern Aspects of the Circulation in Health and Disease, Lea Febiger, 1923.
[82] L. Formaggia and F. Nobile. "A Stability Analysis for the Arbitrary Lagrangian Eulerian Formulation with Finite Elements". In: East-West J. Numer. Math. 7.2 (1999), pp. 105–131.
[83] T. Tezduyar and S. Sathe. "Stabilization parameters in SUPG and PSPG for- mulations". In: Journal of Computational and Applied Mechanics 4.1 (2003), pp. 71–88.
[84] Y. Bazilevs, V. Calo, J. Cottrell, T. Hughes, A. Reali, G. Scovazzi, Variational multiscale residual-based turbulence modeling for large eddy simulation of incompressible flows, Comput. Methods Appl. Mech. Engrg. 197 (1–4) (2007) 173–201.
[85] D. Forti, L. Dedè, Semi-implicit BDF time discretization of the navier-Stokes equations with VMS-LES modeling in a high performance computing framework, Comput. Fluids 117 (2015) 168–182.
[86] Chunguang Li and Kees Vuik. The GCR-SIMPLE Solver and the SIMPLE-type preconditioning for Incompressible Navier-Stokes Equations. 2004.
[87] W. E. Arnoldi,The principle of minimized iterations in the solution of the matrix eigenvalue problem, Quart. Appl. Math., 9 (1951), pp. 17–29
[88] Hessenberg, K. Thesis. Darmstadt, Germany: Technische Hochschule,

1942.
[89] Press, W. H.; Flannery, B. P.; Teukolsky, S. A.; and Vetterling, W. T. "Reduction of a General Matrix to Hessenberg Form." §11.5 in Numerical Recipes in FORTRAN: The Art of Scientific Computing, 2nd ed. Cambridge, England: Cambridge University Press, pp. 476-480, 1992.
[90] J.C.R. Hunt, A.A. Wray and P. Moin, ≪Eddies, stream, and convergence zones in turbulent flows≫, Center for Turbulence Research Report, CTR-S88, 1988
[91] J.M. Dolan, J. Kolega and H. Meng, High wall shear stress and spatial gradients in vascular pathology: a review. Annals of Biomedical Engineering, 41(7), 2013
[92] Stein, K., Tezduyar, T., and Benney, R. (January 23, 2003). "Mesh Moving Techniques for Fluid-Structure Interactions With Large Displacements ." ASME. J. Appl. Mech. January 2003; 70(1): 58–63.
[93] K. Hergan, A.Schuster,J.Frühwald, M. Mair, R. Burgerand M.Töpker,≪Comparison of left and right ventricular volume measurement using the Simpson's method and the area length method≫,European journal of radiology, vol. 65(2), 2008

Appendix A

Further computational methods for heart function modeling

A.1 Geometric reduced models: the 1D and 0D models

Since the resolution of a 3D FSI problem for the entire circulatory system is not affordable in terms of computational costs, geometric reduced 1D or 0D models were derived, in order to model the complexity of the computational domain.
1D models are obtained by simplifying assumptions from the 3D model, considering cylindrical coordinates (r, ϕ, z), radial displacements and prescribing equations in the axial z-direction. Relevant references are from Euler (1775), [36], [37] and [38]. The introduced quantities are the area of the lumen section A, the mean velocity $\hat{u}$, the velocity profile s, the flow rate Q and the mean pressure P. In terms of the introduced parameters, firstly a membrane law relating the pressure and the lumen area:

$$P(t,z) = P_{ext} + \psi(A(t,z), A_0(z), \beta(z)) \tag{A.1}$$

with the function ψ that is such that $\partial\psi/\partial A$¿0 and $\psi(A_0) = 0$.
Then a system that couples the momentum equation and the mass conservation law integrated over each cross-section S is taken into account:

$$\frac{\partial \mathbf{U}}{\partial t} + H(\mathbf{U})\frac{\partial \mathbf{U}}{\partial z} + B(\mathbf{U}) = \mathbf{0} \tag{A.2}$$

where $\mathbf{U} = [A \ Q]^T$ is the unknown and U and B are matrices representing respectively the flux and the dissipation term.
The 1D models are characterized by the resolution of the system in terms of average quantities that have a lower order of magnitude than the corresponding parameters in the 3D FSI model. However they do not provide a description of the vortices and the recirculation regions.
The 0D models, instead, are obtained by integrating the 1D problems over the axial direction z, introducing the average flow rate $\hat{Q}$ and the average pressure $\hat{P}$, depending on the proximal and longitudinal abscissae z_p and z_d. As a consequence, the proximal and distal flow rates and pressure are obtained.
The final two ordinary differential equations (ODEs) are prescribed taking the longitudinal average of the momentum and mass conservation. Then the system is closed by taking the suitable corresponding boundary conditions, and imposing two equations depending on two of the four unknowns introduced above (the remaining two are provided), localizing the pressure or flow rate at the proximal or distal section. The two equations are obtained by electrical analogy, assuming that the flow rate has the same behaviour of the current, while the pressure represents the potential. The acceleration, the viscosity and the compliance term are modeled respectively by an inductance, a resistance and a capacitance.

A.2 Geometric multiscale coupling

Another significant model is based on a coupling between the three-dimensional, the one-dimensional and zero-dimensional models: the geometric multiscale approach. The aim of applying this technique is to consider the higher dimensional model in a detailed way the physical problem in a specific area of interest, while in the remaining portion of the domain the lower dimensional model is taken into account. Usually the coupling of the 3D and 1D models is the most common approach, since the 0D problems are thought to provide boundary conditions for the higher-dimensional models, in order to well-pose them. However, also the 3D-0D coupling can be provided.

The 3D-1D coupling model reads as the following multidomain formulation:

$$\begin{cases} P_{3D}(\boldsymbol{u}_{3D}, p_{3D}, \boldsymbol{d}_{3D}; \Omega_{3D}) = \mathbf{0}, \\ \rho_f \int_{\Gamma_f} \boldsymbol{u}_{3D} \cdot \boldsymbol{n} = Q_{1D}(z=0), \\ \frac{1}{|\Gamma_f|} \int_{\Gamma_f} p_{3D} = P_{1D}(z=0) = \Psi(A_{1D}(z{=}0), A_0(z{=}0), \beta(z{=}0)) + P_{ext}, \\ \int_0^{2\pi} \int_0^{R_0 + \hat{\mathbf{d}}(\Gamma_s, r=R_0, \phi)} r\, dr d\phi = A_{1D}(z{=}0), \\ P_{1D}(Q_{1D}, A_{1D}; \Omega_{1D}) = 0. \end{cases} \tag{A.3}$$

where the three interface conditions are the result of the mass conservation, the 3^{rd} Newton's Law and the continuity of the structure displacement. Since they are of defective type, these conditions are treated in a specific way in order to complete them. In the case of the pressure condition, the following identity is introduced:

$$(\mathbf{T}_f(\boldsymbol{u}_{3D}, p_{3D}) \cdot \boldsymbol{n})|_{\Gamma_f} = -P_{1D}(z=0)\boldsymbol{n} \tag{A.4}$$

The system is then closed by selecting a velocity profile in the coupling direction (or choosing a Lagrange multiplier approach), assuming circular interface $\Gamma_f \cup \Gamma_s$, treating the structure displacement $\boldsymbol{d}_{3D}$ as independent of ϕ (and so of the 1D model) and, finally, considering suitable interface conditions on the uncoupling directions to well-pose the 3D problem.
The 3D-0D coupling model is obtained in the same way, substituting the 1D pressure and flow rate respectively with the 0D proximal pressure P_{0D} and flow rate Q_{0D}.

A.3 Electrophysiology

The aforementioned models can be applied in both the frameworks of the cardiovascular system, the arterial circulation and the heart function.
For the latter, also the electrical activity has been modeled, studying the electrical propagation at the macroscopic level (Chapter 1, Section 1.1.2) due to cellular excitation, producing an action potential that spreads among the cardiomyocites. The aim is to model the ionic current flow, considering the single membrane cell as a capacitor, with accumulating charges at the intracellular and extracellular surfaces. As a consequence, a trans-membrane potential V_m is introduced and defined as the difference between the intracellular and extracellular potentials.
The membrane current I_m is then derived from the potential and it depends on the membrane capacitance V_m and the surface area-to-volume ratio χ_m. Finally, as result [39] of the application of the conservation of current and

charge (introducing the intracellular and extracellular current fluxes $\boldsymbol{j}_i$ and $\boldsymbol{j}_e$)

$$\nabla \cdot \boldsymbol{j}_i = -I_m, \quad \nabla \cdot \boldsymbol{j}_e = I_m \tag{A.5}$$

and the Ohm's law in both the regions

$$\boldsymbol{j}_i = -\Sigma_i \nabla \phi_i, \quad \boldsymbol{j}_e = -\Sigma_e \nabla \phi_e \tag{A.6}$$

the following partial differential equations (bidomain model) are derived:

$$\begin{cases} \chi_m C_m \frac{m}{\partial t} - \nabla \cdot (\Sigma_i \nabla \phi_i) + \chi_m I_{ion} = I_i^{ext} & in\ \ \Omega, \\ -\chi_m C_m \frac{\partial V_m}{\partial t} - \nabla \cdot (\Sigma_e \nabla \phi_e) + \chi_m I_{ion} = -I_e^{ext} & in\ \ \Omega. \end{cases} \tag{A.7}$$

where Ω is the myocardium and the forcing terms are the applied external currents.

Furthermore the system of equations is closed by modeling the ionic current I_{ion} through ordinary differential equations depending on suitable functions. There are three families of ventricular cell models for the ionic current. The first one concerns the *reduced ionic models*, in which the sub-cellular processes are neglected and the action potential description is provided, introducing the gating variable $\boldsymbol{w}$ that represents the percentage of open channels per unit area with respect to the membrane:

$$\begin{cases} I_{ion} = f(V_m, \boldsymbol{w}), \\ \frac{\partial \boldsymbol{w}}{\partial t} = g_w(V_m, \boldsymbol{w}). \end{cases} \tag{A.8}$$

The most important reduced model is the *FitzHugh-Nagumo* model [40] in which $f(V_m, w) = -k\, V_m(V_m - a)(V_m - 1) - m$ and $g_w = \epsilon(V_m - \gamma w)$, with constant parameters k, a, γ.

The second family consists of *first-generation models*, which are characterized by the mathematical description of different ionic currents. The most known example is the *Hodgkin-Huxley* model [41], where the sodium, potassium and leakage currents I_{NA}, I_K, I_L are also taken into account. The system reads:

$$\begin{cases} I_{ion} = I_{NA} = G_{NA} + I_K + I_L, \\ I_{NA} = G_{NA} \boldsymbol{w}_1^3 \boldsymbol{w}_2 (V_m - V_{NA}), \\ I_K = G_K \boldsymbol{w}_3^4 (V_m - V_K), \\ I_L = G_L (V_m - V_L), \\ \frac{\partial w_j}{\partial t} = (w_j^\infty(V_m) - w_j)/\tau(V_m). \end{cases} \tag{A.9}$$

being V_n and G_n respectively the Nernst potential and the maximal conductance of the n-th ion, while the last equation is applied for each of the

M gating variables (being M the total number of gating variables, M=3 in Eq. A.9). Moreover, w_j^∞ is the equilibrium state and τ_j the characteristic time.
The third family to be mentioned is represented by the *second-generation models*, which focus more on the ion concentration and they are applied in the research field of the ion channels pathologies and drug action.

A.4 Electromechanical coupling

As shown in the previous chapter, the propagation of the trans-membrane potential in the cardiomyocites is responsible for the ventricular (and atrial) contraction at a macroscopic level, due to the longitudinal shortening, wall thickening and torsion. As result, a strong relation between the mechanical and electrical behaviour is detected for what concerns the heart function: indeed, due to the activation of the extra-cellular calcium ions channels due to depolarization of the cell, a inward flux of calcium ions in the direction of the intracellular region occurs. This leads to the bind of the calcium with the troponin, with the following bind between myosin and actin.
In terms of mathematical modeling, the first relevant result, concerning a relation between finite elasticity and electrical activity, is by Nash and Panfilov in 2004 [42], who derived a new formulation of the first Piola-Kirchhoff tensor, decomposed into the sum of two terms:

$$\hat{\mathbf{T}}_s = \hat{\mathbf{T}}_s^P + \hat{\mathbf{T}}_s^A \tag{A.10}$$

The term $\hat{\mathbf{T}}_s^P$ represents the *passive component*, that is the required stress to deform the passive myocardium. It can be modeled by differentiating a suitable energy density function. On the other hand, $\hat{\mathbf{T}}_s^A$ is the *active component*, that refers to the stress provided by the electrical signal in the depolarization phase.
An important assumption in this context is considering the passive myocardium as an orthotropic material (i.e. with two principal directions). This is a consequence of the strict dependence between heart contraction and fibers motion. For this reason three unit vectors $\hat{\mathbf{a}}_f$, $\hat{\mathbf{a}}_s$, $\hat{\mathbf{a}}_n$ are introduced, representing the tangential and the two orthogonal directions to the fibers.
Since the inward flux of calcium ions after the depolarization occurs along the direction of the fibers, the active component is modeled introducing a scalar function P^A in space and time representing the pointwise active stress:

$$\hat{\mathbf{T}}_s^A = P^A \hat{\mathbf{a}}_f \otimes \hat{\mathbf{a}}_f \tag{A.11}$$

The latter has been modeled by Nash and Panfilov [42] in a specific ordinary differential equation, depending on the trans-membrane potential, the resting potential V_r:

$$\frac{dP^A(t)}{dt} = \varepsilon(V_m(t))[k_P(V_m(t) - V_r) - P^A(t)] \tag{A.12}$$

Another interesting result [43] proposes a model of the active potential depending also on calcium concentration c_{ca} and on the stretch in the fibre direction $\lambda = (\hat{\mathbf{a}}_f^T C \hat{\mathbf{a}}_f)^{\frac{1}{2}}$, to account in particular for the stretch activated channels. It consists of the following compact system of ODEs:

$$\begin{cases} \frac{d\boldsymbol{y}}{dt} = \boldsymbol{g}_y(P^A, \lambda, \frac{d\lambda}{dt}, \boldsymbol{c}, \boldsymbol{y}) \\ P^A = g_{P^A}(\lambda, \boldsymbol{y}) \end{cases} \tag{A.13}$$

where the concentration variable is the calcium one and $\boldsymbol{y}$ collects the state variables related to electrophysiology and other variables.
The trans-membrane potential V_m or the concentration of calcium ions c_{ca} in most cases are obtained from the monodomain (or bidomain) equations in an Eulerian framework (in order to deal with a time-variant domain). For simplicity the Lagrangian approach is the chosen one, leading to the following equation for the monodomain, that introduces the deformation map ψ between the initial configuration ($\Omega = \Omega_0$) and the actual configuration $\Omega(t)$:

$$J_{\chi_m} C_m \left(\frac{\partial \hat{V}_m}{\partial t} - \mathbf{F}^{-T} \nabla \hat{V}_m \cdot \frac{\partial \psi}{\partial t} \right) - \nabla \cdot (J\mathbf{F}^{-1} \Sigma \mathbf{F}^{-T} \nabla \hat{V}_m)$$

$$+ J_{\chi_m} \hat{I}_{ion}(\hat{V}_m, \hat{\mathbf{w}}, \hat{\mathbf{c}}, \lambda) = J\hat{I}^{ext} \quad in\ \Omega \tag{A.14}$$

From the equation above, it can be noticed that the mechanics problem affects the electrophysiology problem introducing three sources of *mechanico-electrical feedback*:

- the conductivity tensor $\hat{\Sigma} = J\mathbf{F}^{-1}\Sigma\mathbf{F}^{-T}$ depending on the deformation gradient $\mathbf{F}$
- The stretch in the fiber direction, λ affecting I_{ion}, that leads to the opening of the ionic channels during diastole and allows the current flow (*stretch activated channels*).
- The advection term $-\mathbf{F}^{-T}\nabla\hat{V}_m \cdot \frac{\partial\psi}{\partial t}$, that depends on the solution of the mechanics problem [39], introduced from the relation between time and spatial derivatives

As a result, the action of the stretch activated channels and the active strain component of the gradient deformation leads to the following formulation of the electromechanics problem as a coupled system:
Find the displacement $\boldsymbol{d}$*, the trans-membrane potential* V_m*, the gating variables* $\boldsymbol{w}$*, the concentration variables* $\boldsymbol{b}$*, such that:*

$$\begin{cases} \nabla \cdot \left(\hat{\mathbf{T}}_s^P(\hat{\boldsymbol{d}}) + \hat{\mathbf{T}}_s^A\left(\hat{\boldsymbol{c}}, \hat{\boldsymbol{d}}, \frac{d\hat{\boldsymbol{d}}}{dt}\right)\right) = \mathbf{0} & in\,\Omega, \\ \hat{\mathbf{T}}_s^A = P^A \boldsymbol{a}_f \otimes \boldsymbol{a}_f, \;\; P^A = \mathcal{A}\left(\hat{\boldsymbol{c}}, \hat{\boldsymbol{d}}, \frac{d\hat{\boldsymbol{d}}}{dt}\right) & in\,\Omega, \\ \hat{V}_m = \mathcal{M}(\hat{V}_m; \hat{\boldsymbol{d}}, \hat{\boldsymbol{w}}, \hat{\boldsymbol{c}}) & in\ \Omega, \\ (\hat{\boldsymbol{w}}, \hat{\boldsymbol{c}}) = \mathcal{G}(\hat{\boldsymbol{w}}, \hat{\boldsymbol{c}}; \hat{V}_m) & in\ \Omega. \end{cases} \tag{A.15}$$

where the first equation represents the mechanical problem, the third one represents identifies the system of PDEs of the monodomain problem, while the fourth and last one stands for the ODEs defining the ionic models for the cardiac cells.